

HARVARD UNIVERSITY  
Graduate School of Arts and Sciences



DISSERTATION ACCEPTANCE CERTIFICATE

The undersigned, appointed by the

Department of Physics

have examined a dissertation entitled

Preliminary Measurements for an Electron  
EDM Experiment in ThO

presented by

Yulia Vsevolodovna Gurevich

Candidate for the degree of Doctor of Philosophy and hereby  
Certify that is worthy of acceptance.

Signature Gerald Gabrielse

Typed name: Professor Gerald Gabrielse, Chairman

Signature John Doyle

Typed name: Professor John Doyle

Signature R. Walsworth

Type name: Dr. Ronald Walsworth

Date: August 26, 2011



# Preliminary Measurements for an Electron EDM Experiment in ThO

A thesis presented  
by

Yulia Vsevolodovna Gurevich

to

The Department of Physics  
in partial fulfillment of the requirements  
for the degree of  
Doctor of Philosophy  
in the subject of

Physics

Harvard University  
Cambridge, Massachusetts  
January 2012

UMI Number: 3495611

All rights reserved

INFORMATION TO ALL USERS

The quality of this reproduction is dependent upon the quality of the copy submitted.

In the unlikely event that the author did not send a complete manuscript and there are missing pages, these will be noted. Also, if material had to be removed, a note will indicate the deletion.



UMI 3495611

Published by ProQuest LLC 2012. Copyright in the Dissertation held by the Author.

Microform Edition © ProQuest LLC.

All rights reserved. This work is protected against unauthorized copying under Title 17, United States Code.



ProQuest LLC  
789 East Eisenhower Parkway  
P.O. Box 1346  
Ann Arbor, MI 48106-1346

©2012 - Yulia Vsevolodovna Gurevich

All rights reserved.

Thesis advisor

Author

**Gerald Gabrielse**

**Yulia Vsevolodovna Gurevich**

## **Preliminary Measurements for an Electron EDM Experiment in ThO**

### **Abstract**

The ACME collaboration aims to measure the eEDM via Ramsey spectroscopy of a cryogenic beam of ThO molecules in their metastable  $H$  state. This thesis describes the launch of this new experimental effort. A set of diode lasers has been built to address all the necessary ThO transitions. The laser frequencies were stabilized to a stable reference laser via a Fabry-Pérot transfer cavity. A measurement of the magnetic dipole moment of the  $H$  state has been performed that is complementary to a previous measurement by the collaboration. This value is important for determining the sensitivity of the  $H$  state to magnetic fields, which can be a source of noise and systematic errors in the eEDM measurement. Experimental efforts to prepare the coherent superposition of the  $M = \pm 1$  Zeeman sublevels in the  $H, J = 1$  state that is the starting point of the eEDM experiment using transitions to the  $G$  state resulted in a better understanding of transitions between  $\Omega$ -doublet states in an electric field. This led to a new technique for normalizing out shot-to-shot fluctuations in the molecular beam flux, which has also been demonstrated experimentally.

# Contents

Title Page . . . . .	i
Abstract . . . . .	iii
Table of Contents . . . . .	iv
Acknowledgments . . . . .	vi
<b>1 Background and motivation</b>	<b>1</b>
1.1 The eEDM and fundamental symmetries . . . . .	2
1.2 The Standard Model . . . . .	4
1.2.1 The eEDM in the Standard Model . . . . .	7
1.3 Beyond the Standard Model . . . . .	9
<b>2 The eEDM in atoms and molecules</b>	<b>13</b>
2.1 Schiff's theorem and its violation . . . . .	14
2.2 Polarization of atoms and molecules . . . . .	18
<b>3 Diatomic molecules for eEDM measurements</b>	<b>22</b>
3.0.1 Calculation of molecular matrix elements . . . . .	25
3.0.2 Omega doubling . . . . .	27
3.1 The $H$ state in electric and magnetic fields . . . . .	30
<b>4 The ACME experiment</b>	<b>36</b>
4.1 Thorium monoxide . . . . .	36
4.2 A generic eEDM measurement . . . . .	39
4.3 ACME measurement scheme . . . . .	41
<b>5 Lasers and locks</b>	<b>46</b>
5.1 Apparatus . . . . .	47
5.1.1 LabVIEW program . . . . .	50
5.2 Performance . . . . .	52
5.3 Limitations . . . . .	53

---

<b>6</b>	<b>An alternative g-factor measurement</b>	<b>55</b>
6.1	Apparatus . . . . .	55
6.2	Measurement technique . . . . .	60
6.3	Results . . . . .	63
<b>7</b>	<b>State preparation</b>	<b>71</b>
7.1	The G state . . . . .	74
7.2	A new normalization scheme . . . . .	77
<b>8</b>	<b>Conclusion</b>	<b>83</b>
<b>A</b>	<b>Diode laser assembly instructions</b>	<b>85</b>
A.1	Precautions . . . . .	85
A.2	Selecting the grating . . . . .	86
A.3	Circuit board assembly . . . . .	87
	A.3.1 Current, temperature, and PZT controllers . . . . .	91
A.4	Laser assembly instructions . . . . .	93
	A.4.1 Tuning the temperature control loop . . . . .	99
	A.4.2 Obtaining feedback . . . . .	102
A.5	Some notes on laser operation . . . . .	107
A.6	Limitations and possible improvements . . . . .	107
	<b>Bibliography</b>	<b>109</b>



# Acknowledgments

I would like to thank my adviser, Gerald Gabrielse, for giving me the opportunity to work on this exciting project. I would also like to thank the other PIs of the ACME collaboration, John Doyle and David DeMille, for their support throughout my time in graduate school. I am grateful to Ron Walsworth for agreeing to serve on my committee on short notice and for saying exactly what I needed to hear four days before my defense.

None of the work described here would have been possible without the efforts of the other members of the ACME collaboration. Nick Hutzler designed and characterized the beam source and made the ThO beam work well. He also designed and built the light collection system for the interaction region. Elizabeth Petrik made the ablation and thermochemical targets we use and developed the thermochemical beam source. Amar Vutha designed the interaction region, electric field plates, and magnetic shields. Ben Spaun measured the saturation intensities of the important ThO transitions and helped assemble the interaction region. He and Amar also measured the electric and magnetic dipole moments of the  $H$  state. Paul Hess wrote VIs to automate much of the experiment and set up the polarization switching normalization scheme. Emil Kirilov assembled the interaction region and magnetic shields, came up with the  $C$  state switching normalization method, and put together the AOM system that enabled us to demonstrate this switching. He also made the magnetic field measurements that I use to calculate the  $g$ -factor. I am very grateful to everyone for their help, their good humor, and for letting me monopolize the apparatus during the month before my defense.

I would particularly like to thank Ben for fruit snacks and Green Day articles, Paul

for his lovely DAMOP talk slides, and Emil for telling me what to do and keeping me from despair.

I am grateful to the Doyle group - Hsin-I Lu, Julia Rasmussen, Colin Connolly, Edem Tsikata, Wes Campbell, Matt Hummon, Dave Patterson, Yat Shan Au, and Matt Wright - for making me feel welcome in their lab from the day I joined the ACME experiment, for sharing their knowledge of cryogenic beams, and for generously allowing me to drink their coffee all these years.

I would like to thank Stan Cotreau for making fun of me, Jim MacArthur for laughing when I made fun of myself, and Jan Ragusa for her support, both administrative and emotional. I would also like to thank Isaac for being cute and furry and always willing to be petted.

Finally, I am grateful to the students in the Gabrielse lab - Josh Goldman, Jack DiSciaccia, Josh Dorr, Robert McConnell, Shannon Fogwell Hoogerheide, Phil Richerme, Steve Kolthammer, Rita Kalra, and Elise Novitski. Their company, conversations about physics, life, and everything in between, and their appreciation of my drawings made my time in graduate school enjoyable and cheered me up even when my project was falling apart. I am truly lucky to have worked in a lab with such fun and supportive people.

# Chapter 1

## Background and motivation

The existence of a permanent electric dipole moment (EDM) associated with the spin of the electron would represent direct violation of parity and time reversal symmetries. Both of these symmetries are known to be violated in nature, and our current understanding of their violation is encompassed in the Standard Model (SM) of particle physics. However, the observed dominance of matter over antimatter in the universe strongly suggests that time reversal is violated in additional ways, the consequences of which have so far not been observed experimentally. EDM measurements are a uniquely sensitive probe for such additional violation, since the known time-reversal violation in the SM produces a negligibly small background.

This thesis describes work done as part of the ACME collaboration, a joint effort between Harvard University (Professors John Doyle and Gerald Gabrielse) and Yale University (Professor David DeMille). The collaboration began in 2007 with the goal of using a cryogenic beam of thorium monoxide (ThO) molecules to measure the electron EDM (eEDM). All major parts of the apparatus - the beam source, electric

field plates, magnetic shields and coils, and laser systems - are now in place. This year we observed spin precession in electric and magnetic fields using a measurement technique very similar to the one we will use in the real eEDM experiment.

This thesis describes construction of the laser locking system and some preliminary measurements for the ACME experiment. The remainder of this chapter discusses the motivation for eEDM measurements in more detail. Chapter 2 describes the observable effect of the eEDM in atoms and molecules, while Chapter 3 provides some background on diatomic molecules necessary for understanding the ACME experiment. The planned experiment is described in Chapter 4, while Chapters 5, 6, and 7 focus on aspects of the work in which I was involved. This includes building diode lasers and a system to stabilize the lasers' frequencies (Chapter 5), a measurement of the magnetic moment of the eEDM-sensitive state of ThO (Chapter 6), and work on preparation of the initial state for the eEDM experiment (Chapter 7).

## 1.1 The eEDM and fundamental symmetries

First, let's convince ourselves that a non-zero eEDM requires violation of both parity and time reversal. According to the Wigner-Eckart theorem, the expectation value of any vector operator in an eigenstate of total angular momentum  $\mathbf{J}$  is proportional to the expectation value of  $\mathbf{J}$ . For an isolated electron, this means that  $\langle \mathbf{d}_e \rangle \propto \langle \mathbf{S} \rangle$ , where  $\mathbf{S}$  is the electron's spin. In an eigenstate of  $S_z$ , the  $z$ -component of the eEDM must be  $\langle d_{e,z} \rangle = \beta \langle J_z \rangle = \beta m$ , where  $\beta$  is some constant. Since the  $z$ -direction is arbitrary for a rotationally symmetric system, we can write this relationship as  $\mathbf{d}_e = \beta \mathbf{S}$ . As shown in Fig. 1.1, the two sides of this equation transform

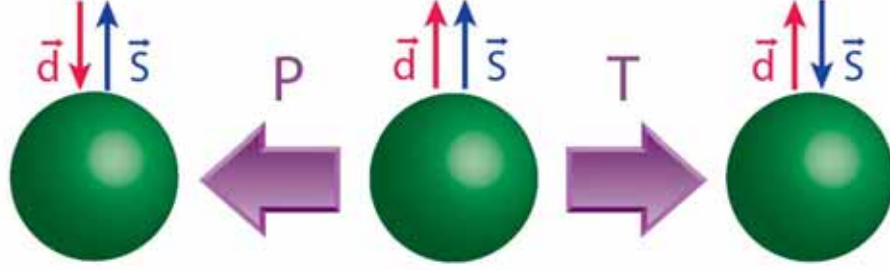


Figure 1.1: Transformation properties of the electron spin ( $\vec{S}$ ) and EDM ( $\vec{d}$ ) under parity ( $P$ ) and time reversal ( $T$ ). The spin is even under  $P$  and odd under  $T$ , whereas the EDM is odd under  $P$  and even under  $T$ . A non-zero EDM would not violate  $P$  or  $T$  if electrons existed both with  $\vec{d}_e = |\beta|\vec{S}$  and  $\vec{d}_e = -|\beta|\vec{S}$ ; these two states would be degenerate if  $P$  and  $T$  were good symmetries. In that case, the relative orientation of the spin and EDM would constitute an additional degree of freedom for the electron, and another quantum number would be required to specify its state. Since we know from atomic structure that this is not the case, only one type of electron exists in nature. In this situation, a non-zero EDM implies  $P$  and  $T$  violation.

differently under both parity and time reversal; for this relation to remain valid for the transformed electron,  $\beta$  must be zero.

Parity and time reversal are two of the three discrete symmetries important in the Standard Model. Parity ( $P$ ) corresponds to inversion of all three spatial coordinates, i.e.  $\mathbf{x} \rightarrow -\mathbf{x}$ . Time reversal ( $T$ ) corresponds to  $t \rightarrow -t$ . The third symmetry is charge conjugation ( $C$ ), which interchanges particles and antiparticles. A physical process respects one of these symmetries if the result of applying the symmetry operation is an equally possible process. The combined action of  $C$ ,  $P$ , and  $T$  is a symmetry of any Lorentz invariant, local quantum field theory [1]. However, neither the individual transformations  $C$ ,  $P$ , and  $T$  nor combinations of any two of them are good symmetries of nature; they are violated by the weak interaction. Parity violation is inherent in the structure of the weak interaction, since the  $W$  and  $Z$  bosons

interact only with the left-handed component of each quark or lepton field. As we will now see,  $T$ -violation<sup>1</sup> can also occur in certain weak interaction processes due to a complex phase in the Cabbibo-Kobayashi-Maskawa (CKM) matrix.

## 1.2 The Standard Model

Generically,  $T$ -violation arises from complex coupling constants in the Lagrangian<sup>2</sup>. In the SM, there is only one source of  $T$ -violation, the complex phase  $\delta_{CKM}$  in the CKM matrix<sup>3</sup>. When the SM Lagrangian is expressed in terms of the mass eigenstate fields (i.e. the couplings to the Higgs are diagonalized),  $T$ -violation appears only in the charged current weak interaction of the quarks<sup>4</sup>. To see how this occurs, we write down the Lagrangian for the charged current weak interaction

$$\mathcal{L}_{CC} = \frac{g}{\sqrt{2}} \left( V_{kl} \bar{u}_{kL} \gamma^\mu d_{lL} W_\mu^+ + V_{lk}^* \bar{d}_{kL} \gamma^\mu u_{lL} W_\mu^- \right) \quad (1.1)$$

Here the indices  $k = u, c, t$  and  $l = d, s, b$  run over all possible flavors of up-type and down-type quarks, respectively, and the parameter  $V_{kl}$  is the appropriate element of the CKM matrix.  $T$  would be a good symmetry if  $\mathcal{L}_{CC}$  were unchanged under a  $T$  transformation:  $T\mathcal{L}_{CC}T^{-1} = \mathcal{L}_{CC}$ . Using the  $T$ -transformation properties of the

---

<sup>1</sup>Assuming CPT invariance, as we do throughout this thesis,  $T$ -violation is equivalent to  $CP$  violation and is more commonly discussed under this name.

<sup>2</sup>Complex couplings lead to  $T$ -violation because the operator that implements the  $T$  transformation is antiunitary. See [2] for a more detailed discussion.

<sup>3</sup>A  $P$ - and  $T$ -violating term  $\theta_{QCD}$  can also occur in quantum chromodynamics. Limits on the neutron EDM impose the constraint  $|\theta_{QCD}| < 10^{-9}$  [3]. Providing a natural explanation for the smallness of  $\theta_{QCD}$  remains problematic (this is the *strong CP problem*). We ignore this term since it is irrelevant for the electron.

<sup>4</sup>For the moment, we are assuming that neutrinos are massless. The effects of neutrino mass will be discussed at the end of this section.

fields [2]

$$T\psi_l T^{-1} = e^{i\beta_l} \gamma_0^* \gamma_5^* C^* A \psi_l \quad (1.2)$$

$$T\bar{\psi}_k T^{-1} = e^{-i\beta_k} \psi^\dagger (C^{-1})^* \gamma_5^* \gamma_0^* \quad (1.3)$$

$$TW_\mu^+ T^{-1} = e^{i\beta_W} W^{\mu+}, \quad (1.4)$$

we find that  $T$  will be a symmetry of  $\mathcal{L}_{CC}$  if the CKM matrix elements satisfy

$$V_{kl}^* = e^{i(\xi_l - \xi_k - \xi_W)} V_{kl}. \quad (1.5)$$

If we write the CKM matrix elements as

$$V_{kl} = R_{kl} e^{i\theta_{kl}}, \quad (1.6)$$

the theory will be  $T$ -invariant if we can define the  $T$  transformation phases such that

$$\xi_l - \xi_k - \xi_W = -2\theta_{kl}. \quad (1.7)$$

To see whether we have enough independent phases  $\xi_k$  at our disposal, we first consider the SM with  $n$  generations of quarks and later specialize to the case of our world where  $n = 3$ . For  $n$  generations,  $V_{CKM}$  is an  $n \times n$  unitary matrix, which means there are  $(n^2 + n)/2$  independent  $\theta_{kl}$  ( $n^2$  matrix elements minus  $(n^2 - n)/2$  constraints from unitarity). There are  $2n$  quark fields ( $n$  up-type and  $n$  down-type); thus, there are  $2n - 1$  phase differences<sup>5</sup>. The number of  $\theta_{kl}$  that cannot be eliminated using Eqn. (1.7) is thus  $(n - 2)(n - 1)/2$ . This means that  $T$  violation can occur via the CKM matrix only for  $n \geq 3$ . For  $n = 3$ , there is only one complex phase in the CKM matrix that cannot be eliminated by phase redefinitions of the quark fields. This phase  $\delta_{CKM}$  is the only source of  $T$  violation in the Standard Model.

---

<sup>5</sup>A phase common to all the quark fields does not affect  $V_{CKM}$ .

We can change the phases of the CKM matrix elements by rephasing the quark fields, i.e.  $u_k \rightarrow e^{i\phi_k} u_k$ ,  $d_k \rightarrow e^{i\phi_k} d_k$ . Since physical observables cannot depend on such arbitrary phase choices, the only observable parameters of the CKM matrix are those invariant under phase redefinitions. The only rephasing invariant quantities that can be built from CKM matrix elements are the magnitudes of the elements  $|V_{kl}|^2$  and quantities of the form

$$Q_{ijkl} = V_{ik} V_{jl} V_{il}^* V_{jk}^*, \quad (1.8)$$

where there is no summation over repeated indices. The condition for  $T$ -invariance, Eqn. (1.7), also guarantees that all quantities  $Q_{ijkl}$  in Eqn. (1.8) are real. Thus, we are led to an alternative formulation of the  $T$ -invariance condition: the theory is  $T$ -invariant if and only if all of the rephasing invariants of the CKM matrix are real [2]. Since the SM contains only one complex phase, the imaginary parts of all  $Q_{ijkl}$  are equal up to a sign. If we define the Jarlskog invariant [4] as

$$J \equiv |\text{Im}(V_{ik} V_{jl} V_{il}^* V_{jk}^*)|, \quad (1.9)$$

all  $CP$ -violating quantities in the Standard Model are proportional to  $J$ . In terms of the mixing angles between quarks of different generations and the complex phase  $\delta_{CKM}$ , the Jarlskog invariant is [5]

$$J = s_{12} s_{13} s_{23} c_{12} c_{13}^2 c_{23} \sin \delta_{CKM}, \quad (1.10)$$

where  $s_{ij} = \sin \theta_{ij}$  and  $c_{ij} = \cos \theta_{ij}$ . Each angle is labeled with two indices indicating the two generations that are mixed;  $\theta_{ij} = 0$  would indicate that the two generations  $i$  and  $j$  are decoupled. Although  $\delta_{CKM} = 1.05 \pm 0.24$  radians [5] is large,  $J =$



$2.91_{-0.11}^{+0.19} \times 10^{-5}$  [6] is small due to the smallness of the mixing angles between different generations  $\theta_{12}$ ,  $\theta_{13}$ , and  $\theta_{23}$ .

### 1.2.1 The eEDM in the Standard Model

In the SM, the eEDM arises from loop diagrams involving quarks and  $W$  bosons. The lowest order diagram that could produce a result proportional to the Jarlskog invariant is shown in Fig 1.2 (a). Pospelov and Khriplovich [7] proved that the sum of all diagrams of this form is zero; however, they expect a non-zero result if strong interactions of the quarks in the loop are included, as shown in Fig 1.2 (b). To our knowledge, an exact calculation of the electron EDM in the SM has not been done. A rough estimate of the sum of all diagrams of the form shown in Fig. 1.2 (b) is

$$d_e \sim e \frac{\alpha^3 \alpha_s J m_e}{(2\sqrt{2} \sin \theta_W M_W)^6 \pi^4} \sum_{i,j,k,l} (m_i^2 - m_k^2)(m_j^2 - m_l^2), \quad (1.11)$$

where  $\alpha$  is the fine structure constant,  $\alpha_s$  is the strong interaction coupling constant,  $\theta_W$  is the weak mixing angle,  $M_W$  is the mass of the  $W$  boson,  $m_e$  is the electron mass, and the sum runs over all quark flavors of the appropriate type (up-type for  $i$ ,  $k$  and down-type for  $j$ ,  $l$ ). The dependence on quark mass differences is a key feature of the SM and comes about as follows. Each diagram of the form in Fig. 1.2 (b) is proportional to  $Q_{iklj} = V_{il}V_{kj}V_{ij}^*V_{kl}^*$ . Interchanging  $i$  and  $k$  gives a diagram proportional to  $Q_{kilj} = Q_{iklj}^*$ , which has an imaginary part of opposite sign. Since only the imaginary part contributes to  $d_e$ , diagrams with any two quarks of the same type interchanged contribute with opposite signs. Since the only difference between quarks of the same type is their mass, the diagrams would cancel if two quarks of the same type had the same mass. This is the GIM mechanism [8]. Using the heaviest up-type

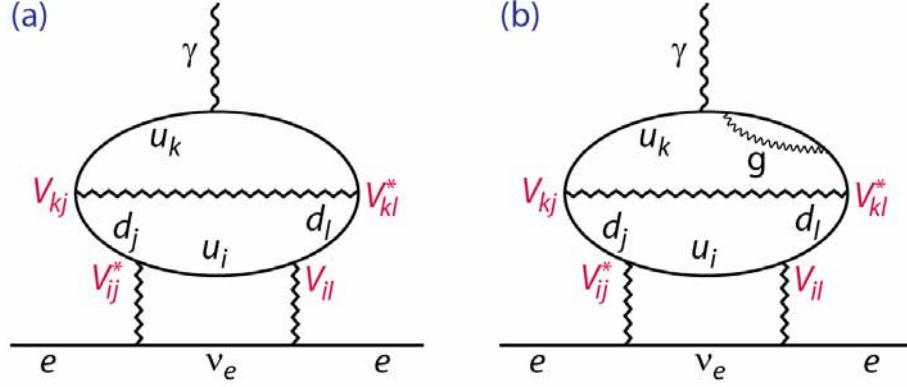


Figure 1.2: **(a)** Three-loop diagram for the eEDM. The sum of all such diagrams is zero [7]. **(b)** Four-loop diagram for the eEDM. Diagrams of this type are expected to give the largest non-zero contribution to the eEDM in the SM. Here  $u_k$  denotes an up-type quark of generation  $k$ ,  $d_j$  denotes a down-type quark of generation  $j$ , zig-zag lines denote  $W$  bosons, and  $g$  denotes a gluon. The virtual gluon should be attached to all possible quark lines, and the external photon should be attached to all possible charged lines. The CKM matrix element appearing at each vertex is indicated in red.

and down-type quark masses gives the numerical estimate

$$d_e \sim e \frac{\alpha^3 \alpha_s J m_e}{(2\sqrt{2} \sin \theta_W M_W)^6 \pi^4} m_b^2 m_t^2 \sim 10^{-38} e \cdot \text{cm}, \quad (1.12)$$

where  $m_b$  is mass of the bottom quark and  $m_t$  is the mass of the top quark. This value is many orders of magnitude below the current experimental limit  $|d_e| < 1.05 \times 10^{-27} e \cdot \text{cm}$  [9].

The above discussion assumed that neutrinos were massless, in which case the analogue of the CKM matrix in the lepton sector was simply the unit matrix. Since neutrinos are known to have mass, the lepton mixing matrix - called the Pontecorvo-Maki-Nakagawa-Sakata (PMNS) matrix - is non-trivial and can contain additional  $T$ -violating phases. The number of phases in the PMNS matrix depends on the number

of neutrino species<sup>6</sup>, as well as on whether neutrinos are Dirac or Majorana fermions. For a minimal model with three neutrino species, the PMNS matrix contains one Dirac phase (analogous to  $\delta_{CKM}$  in the quark sector) and two Majorana phases [10]. These phases produce a non-zero eEDM at the two loop level; however, for realistic values of the active neutrino masses, the resulting eEDM remains orders of magnitude below the sensitivity of current or proposed experiments [11].

### 1.3 Beyond the Standard Model

Although all current experimental data are consistent with the CKM phase as the only source of  $T$ -violation, it is widely believed that additional sources of  $T$ -violation exist. One motivation for this belief is the success of the inflationary scenario in cosmology, which necessitates a way to dynamically generate the observed baryon asymmetry of the universe from the baryon-symmetric state that existed at the end of inflation. Dynamical production of a net baryon number - baryogenesis - requires three conditions [12]: (1) violation of baryon number, (2) departure from thermal equilibrium, and (3)  $C$ - and  $CP$ -violation. Although the SM contains all three ingredients, the baryon asymmetry that can be dynamically generated with  $\delta_{CKM}$  as the only source of  $CP$ -violation is orders of magnitude below the observed value [3].

For this reason and others, the Standard Model is unlikely to provide a complete description of nature. In particular, it does not include gravity, while any theory valid up to the Planck scale should incorporate gravitational interactions. The SM

---

<sup>6</sup>Besides the known three active neutrino species that participate in the weak interaction, there may be an unknown number of sterile neutrinos that do not interact weakly.

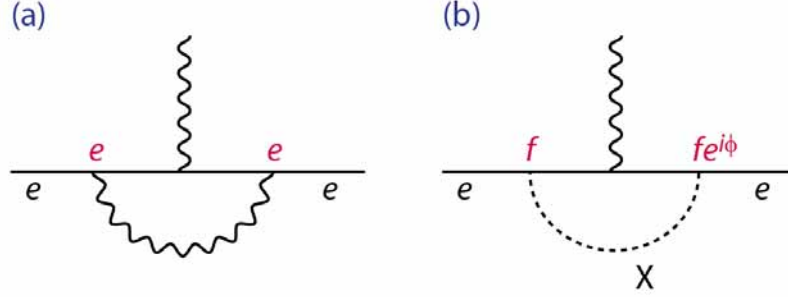


Figure 1.3: **(a)** One-loop diagram for the electron  $g - 2$ . **(b)** Similar diagram for the eEDM.

also fails to provide any viable candidate for dark matter, the non-baryonic particles that constitute 83% of the matter in the universe. In addition, the SM has several features that seem unnatural to many authors. Perhaps the best known of these is the *gauge hierarchy problem*, the quadratic sensitivity of the Higgs boson mass to the largest energy scale in the theory. Another is the *strong CP problem*, the experimental fact that the  $CP$ -violating term in quantum chromodynamics is extremely small, for which the SM can provide no explanation. Resolving some of these problems has been the main motivation for most of the proposed extensions of the SM.

Essentially all proposed extensions include additional particles not present in the SM, allowing additional complex coupling constants that lead to  $T$ -violation. In many such models, non-zero contributions to the eEDM appear at the one- or two-loop level in perturbation theory, leading to a greatly enhanced effect compared to the SM. In fact, if the  $T$ -violating phases appearing in these new interaction terms are similar in size to  $\delta_{CKM}$ , many of these theories predict values of the eEDM at or above the current experimental limit.

Following [5], we can estimate the magnitude of  $d_e$  expected in almost any extension of the SM. Consider the diagram of Fig. 1.3, which is very similar to the diagram

that gives the lowest-order correction to the electron  $g$ -factor,  $g - 2 = \alpha/\pi$ . From dimensional analysis, we expect,

$$\frac{d_e}{(g - 2)\mu_B} \sim \left(\frac{f}{e}\right)^2 \sin \phi \left(\frac{m_e}{M_X}\right)^2. \quad (1.13)$$

The dependence on the squared mass ratio (rather than some other power of  $m_e/M_X$ ) occurs because the integral for this diagram has six powers of momentum in the denominator, and after integrating over the loop momentum  $d^4p$ , the result will scale as  $\Lambda^{-2}$ , where  $\Lambda$  is the largest energy scale in the problem, in this case, the mass  $M_X$ . Assuming the coupling constants are similar ( $f \sim e$ ) and the  $T$ -violating phase is similar to  $\delta_{CKM}$  so  $\sin \phi \sim 1$ , the eEDM is

$$d_e \sim \left(\frac{f}{e}\right)^2 \sin \phi \left(\frac{m_e}{M_X}\right)^2 \frac{\alpha}{\pi} \mu_B \sim \left(\frac{100 \text{ GeV}}{M_X}\right)^2 \times 10^{-24} e \cdot \text{cm}. \quad (1.14)$$

In most theories that attempt to provide a natural solution of the gauge hierarchy problem, some particles must appear with masses in the range of 100 GeV - 1 TeV<sup>7</sup>. Thus, in any such theory, the “natural” range for  $d_e$  is  $10^{-24} - 10^{-26} e \cdot \text{cm}$ . Each additional loop typically introduces another factor of  $f^2/\pi \sim \alpha/\pi \sim 3 \times 10^{-3}$ . Thus, the current experimental limit  $|d_e| < 1.05 \times 10^{-27} e \cdot \text{cm}$  [9] already places significant constraints on theories in which  $d_e$  appears at the one- or two-loop level.

It is not surprising that virtually all extensions of the SM predict significantly larger values of  $d_e$  since the combination of features that makes  $d_e$  small in the SM - a single source of  $T$ -violation in the quark sector combined with GIM suppression due to the family structure of quarks - is absent in more general theories. Indeed, in many

---

<sup>7</sup>To solve the gauge hierarchy problem, some new physics has to appear at an energy scale not too far from the scale of the Higgs boson mass, which is experimentally constrained to the range  $114 < m_H < 186 \text{ GeV}$  [13].

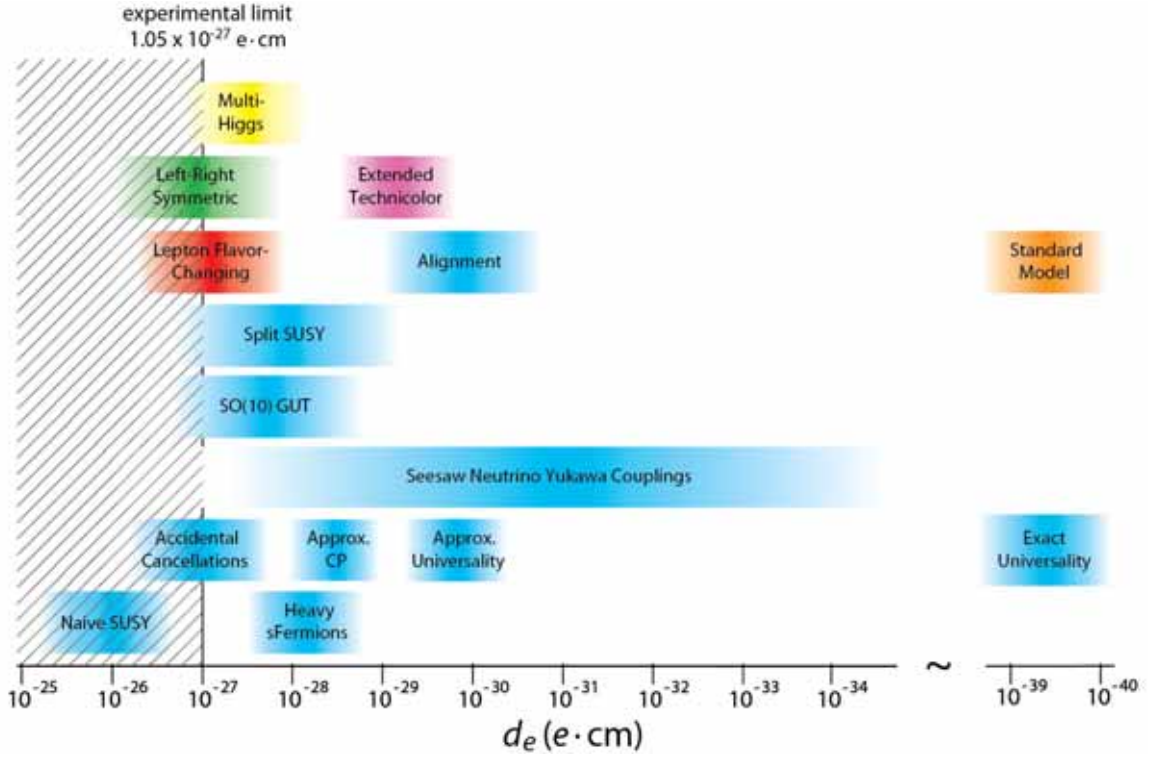


Figure 1.4: Predictions for the eEDM from the SM and some proposed extensions (see [14] for details). The hatched region is excluded by the current experimental limit [9]. All models shown in blue are supersymmetric.

proposed extensions, it is difficult to avoid values of  $d_e$  that are already experimentally excluded unless special assumptions are made about the masses or coupling constants of the new particles in the theory. As seen in Fig. 1.4, eEDM measurements are already beginning to impose significant constraints on several classes of new physics models. An improvement in sensitivity by an order of magnitude or more could entirely rule out some of these theories or perhaps even detect an eEDM.

## Chapter 2

# The eEDM in atoms and molecules

The signature of an eEDM is the electric analog of the Zeeman effect, an energy shift that depends on the orientation of the electron's spin relative to an applied electric field. Detecting this effect with free electrons is difficult since the electric field required to induce the shift would quickly accelerate them out of the region of observation. Thus, the eEDM is most commonly studied via measurements on paramagnetic atoms or molecules. In this case, the measured energy shift is  $\Delta E_{edm} = -\mathbf{d}_a \cdot \mathcal{E}_e$ , where  $\mathbf{d}_a$  is the atomic or molecular EDM and  $\mathcal{E}_e$  is the applied electric field. This shift can be written in terms of the eEDM  $\mathbf{d}_e$  as  $\Delta E_{edm} = -\mathbf{d}_e \cdot \mathcal{E}_{eff}$ , where  $\mathcal{E}_{eff}$  is the effective electric field experienced by the unpaired electron.

Interpretation of a measured energy shift in terms of a limit on  $d_e$  requires knowledge of the effective electric field  $\mathcal{E}_{eff}$ . In this chapter, we describe the basic method of calculating  $\mathcal{E}_{eff}$  using the simplest example of an atom with a single valence electron. The resulting expression can also be used to estimate the effective field in a diatomic molecule like ThO, although detailed molecular calculations are needed for a more

precise determination of  $\mathcal{E}_{eff}$ . As we will see, the *eEDM* energy shift depends on the degree of polarization of the species in an applied electric field, which can be orders of magnitude greater for molecules than for atoms. This property is what makes polar molecules so attractive for *eEDM* measurements.

## 2.1 Schiff's theorem and its violation

Schiff [15] showed that in the limit of non-relativistic quantum mechanics, there is no first-order shift of the atomic energy levels due to the *eEDM*, i.e. the atom does not acquire a permanent EDM even if the electron has one. A relativistic treatment of the problem does reveal a first-order effect; indeed, as pointed out by Sandars [16, 17], in heavy atoms the resulting atomic EDM  $d_a$  can be orders of magnitude larger than the *eEDM*  $d_e$ . This enhancement of the *eEDM* in heavy atoms is what makes precision measurements of this very small quantity possible.

To see how the enhancement arises, we will use perturbation theory to calculate the effect of the *eEDM* on the atomic energy levels. We work in the central field approximation and assume that the atom has only one valence electron. The unperturbed Hamiltonian is the Dirac Hamiltonian for an atom in an external electric field,

$$H_D = c\boldsymbol{\alpha} \cdot \mathbf{p} + mc^2\gamma^0 - e\Phi. \quad (2.1)$$

Here the total electrostatic potential is  $\Phi = \Phi_{int} + \Phi_{ext}$ , where  $\Phi_{int}$  is the atomic electrostatic potential and  $\Phi_{ext}$  is the potential of the applied electric field. To determine the correct Hamiltonian for the *eEDM* interaction, we start from the Lagrangian



density [18]

$$\mathcal{L}_{edm} = -\frac{i d_e}{2} \bar{\psi} \sigma^{\mu\nu} \gamma^5 \psi F_{\mu\nu}, \quad (2.2)$$

where  $\psi$  is the electron field,  $\bar{\psi} = \psi^\dagger \gamma^0$  is the conjugate field,  $\sigma^{\mu\nu} = (i/2)(\gamma^\mu \gamma^\nu - \gamma^\nu \gamma^\mu)$ ,  $\gamma^\mu$  are the Dirac matrices, and  $F_{\mu\nu} = \partial_\mu A_\nu - \partial_\nu A_\mu$  is the electromagnetic field tensor. In terms of the electric ( $\boldsymbol{\mathcal{E}}$ ) and magnetic ( $\boldsymbol{\mathcal{B}}$ ) fields experienced by the electron, we have

$$\mathcal{L}_{edm} = d_e \bar{\psi} [\boldsymbol{\Sigma} \cdot \boldsymbol{\mathcal{E}} + i \boldsymbol{\alpha} \cdot \boldsymbol{\mathcal{B}}] \psi, \quad (2.3)$$

where

$$\boldsymbol{\Sigma} = \begin{pmatrix} \boldsymbol{\sigma} & 0 \\ 0 & \boldsymbol{\sigma} \end{pmatrix}, \boldsymbol{\alpha} = \begin{pmatrix} 0 & \boldsymbol{\sigma} \\ \boldsymbol{\sigma} & 0 \end{pmatrix}. \quad (2.4)$$

This gives the single-particle Hamiltonian [19]

$$H_{edm} = -d_e (\gamma^0 \boldsymbol{\Sigma} \cdot \boldsymbol{\mathcal{E}} + i \gamma^0 \boldsymbol{\alpha} \cdot \boldsymbol{\mathcal{B}}). \quad (2.5)$$

The classical expression  $-\boldsymbol{d} \cdot (\boldsymbol{\mathcal{E}} + \boldsymbol{v} \times \boldsymbol{\mathcal{B}})$  is the non-relativistic limit of this interaction. Since the electric term is larger than the magnetic term in paramagnetic atoms, we take

$$H_{edm} = -d_e \gamma^0 \boldsymbol{\Sigma} \cdot \boldsymbol{\mathcal{E}} \quad (2.6)$$

as the perturbation.

Before calculating the energy shift, it is convenient to rewrite Eqn. (2.6) as

$$H_{edm} = -d_e \boldsymbol{\Sigma} \cdot \boldsymbol{\mathcal{E}} - d_e (\gamma^0 - 1) \boldsymbol{\Sigma} \cdot \boldsymbol{\mathcal{E}}. \quad (2.7)$$

The first-order energy shift of the state  $|\psi_0\rangle$  is thus

$$\Delta E_{edm} = \langle \psi_0 | -d_e \boldsymbol{\Sigma} \cdot \boldsymbol{\mathcal{E}} | \psi_0 \rangle + \langle \psi_0 | -d_e (\gamma^0 - 1) \boldsymbol{\Sigma} \cdot \boldsymbol{\mathcal{E}} | \psi_0 \rangle = \Delta E_1 + \Delta E_2. \quad (2.8)$$

The second term in Eqn. 2.8 is very small in the non-relativistic limit because the operator  $(\gamma^0 - 1) \boldsymbol{\Sigma} \cdot \boldsymbol{\mathcal{E}}$  acts only on the small components of the electron's wavefunction. We first calculate  $\Delta E_1$ , the dominant term in the non-relativistic limit. We can write the electric field as

$$\boldsymbol{\mathcal{E}} = -\nabla\Phi = \frac{-i}{e\hbar} [\mathbf{p}, e\Phi], \quad (2.9)$$

where the chain rule is used in the last step. Using Eqn. (2.1), we have

$$\boldsymbol{\Sigma} \cdot \boldsymbol{\mathcal{E}} = \frac{-i}{e\hbar} [\boldsymbol{\Sigma} \cdot \mathbf{p}, e\Phi] = \frac{-i}{e\hbar} [\boldsymbol{\Sigma} \cdot \mathbf{p}, (H_D - c\boldsymbol{\alpha} \cdot \mathbf{p} + mc^2\gamma^0)] = \frac{-i}{e\hbar} [\boldsymbol{\Sigma} \cdot \mathbf{p}, H_D], \quad (2.10)$$

where the last step follows because  $[\boldsymbol{\Sigma} \cdot \mathbf{p}, \boldsymbol{\alpha} \cdot \mathbf{p}] = 0$  and  $[\boldsymbol{\Sigma} \cdot \mathbf{p}, \gamma^0] = 0$ . The energy shift is then

$$\Delta E_1 = -\frac{id_e}{e} \langle \psi_0 | [\boldsymbol{\Sigma} \cdot \mathbf{p}, H_D] | \psi_0 \rangle = 0 \quad (2.11)$$

because  $|\psi_0\rangle$  is an eigenstate of  $H_D$ . What we have just proved is Schiff's theorem [15]. The derivation given here follows that in [5].

The relativistic shift  $\Delta E_2$  is *not* zero, and it is responsible for the enhancement of the  $eEDM$  in heavy atoms. We now calculate this shift, following the discussion in [20] and [21]. Since

$$(\gamma_0 - 1)\boldsymbol{\Sigma} \cdot \boldsymbol{\mathcal{E}} = \begin{pmatrix} 0 & 0 \\ 0 & -2\boldsymbol{\sigma} \cdot \boldsymbol{\mathcal{E}} \end{pmatrix}, \quad (2.12)$$

we can simplify  $\Delta E_2$  by writing the electron wavefunction in terms of its large ( $f_0$ ) and small ( $g_0$ ) components as

$$|\psi_0\rangle = \begin{pmatrix} f_0 \\ g_0 \end{pmatrix}, \quad (2.13)$$

in which case  $\Delta E_2$  becomes

$$\Delta E_2 = -2d_e \langle g_0 | \boldsymbol{\sigma} \cdot \boldsymbol{\mathcal{E}} | g_0 \rangle. \quad (2.14)$$

This energy shift depends only on the small components of the electron wavefunction, which are related to the large components by  $|g_0/f_0| \sim v/c$ , where  $v$  is the electron's velocity and  $c$  is the speed of light. In the non-relativistic limit,  $v \ll c$ , these components are indeed small. Very close to the nucleus, however, the ratio of the small components to the large components can approach unity. In this region, the electron's potential energy  $V(r) = -Ze^2/r$  assumes very large negative values, which means that its kinetic energy must assume correspondingly large positive values because its total energy is constant. In particular, this implies that  $v$  can become close to  $c$  in this region. This argument suggests that the main contribution to the energy shift comes from the region very close to (and inside) the nucleus, an expectation confirmed by more rigorous calculations [5]. An electron with little or no orbital angular momentum has the highest probability of penetrating into this region, which is why atoms with valence electrons in  $s$ - or  $p$ -orbitals are preferable. Since the magnitude of the small components of the wavefunction scales as  $Z^2\alpha^2$ , an atom with large  $Z$  is necessary.

Due to the odd parity of  $\mathcal{E}$ , the energy shift vanishes if  $|g_0\rangle$  is a parity eigenstate. This is why an external electric field is necessary. Since we assumed that  $|g_0\rangle$  is an eigenstate of  $H_D$ , which includes an external field, it is indeed a state of mixed parity. Assuming the valence electron is nominally in an  $|s_{1/2}\rangle$  state to which the electric field admixes some amount of  $|p_{1/2}\rangle$ , we write  $|g_0\rangle$  as

$$|g_0\rangle = \epsilon_s |g_{s_{1/2}}\rangle + \epsilon_p |g_{p_{1/2}}\rangle + \dots \quad (2.15)$$

For an atom, we expect  $\epsilon_s \sim 1$  and  $\epsilon_p \ll 1$ . We will not, however, assume anything about  $\epsilon_s$  and  $\epsilon_p$  at this stage. We neglect mixing with the  $|p_{3/2}\rangle$  and higher states in

Eqn. (2.15) since the wavefunctions of these states scale as higher powers of  $r$  near the origin and are thus very small.

Very close to the nucleus, the total electric field  $\mathcal{E}$  seen by the electron can be well approximated by  $\mathcal{E} \approx kZe\hat{r}/r^2$ , the Coulomb field of the unscreened nucleus, where  $k = (4\pi\epsilon_0)^{-1}$ . This gives for the matrix element

$$\Delta E_2 = -4d_e kZe\epsilon_s\epsilon_p \left\langle g_{s_{1/2}} \left| \frac{\boldsymbol{\sigma} \cdot \hat{\mathbf{r}}}{r^2} \right| g_{p_{1/2}} \right\rangle \quad (2.16)$$

The radial integral is ([22], 8.13)

$$\Gamma_{rel} = a_0^2 \left\langle g_{s_{1/2}} \left| \frac{\boldsymbol{\sigma} \cdot \hat{\mathbf{r}}}{r^2} \right| g_{p_{1/2}} \right\rangle = \frac{2(Z\alpha)^2}{\gamma(4\gamma^2 - 1)(\nu'\nu)^{3/2}}, \quad (2.17)$$

where  $a_0$  is the Bohr radius,  $\gamma = \sqrt{(j + 1/2)^2 - Z^2\alpha^2}$ , and  $\nu$  and  $\nu'$  are the effective principal quantum numbers for the  $s_{1/2}$  and  $p_{1/2}$  states. Putting everything together, we find

$$\Delta E_2 = - \left[ \left( \frac{8ke}{a_0^2} \right) Z \Gamma_{rel} \epsilon_s \epsilon_p \right] d_e = [(4.1 \times 10^{10} \text{ V/cm}) Z \Gamma_{rel} \epsilon_s \epsilon_p] d_e \quad (2.18)$$

The quantity in square brackets can be interpreted as the effective electric field acting on the eEDM. The size of this field depends on two different properties of the atom: the relativistic enhancement described by  $Z \Gamma_{rel}$  and the mixing of opposite parity states described by  $\epsilon_s$  and  $\epsilon_p$ .

## 2.2 Polarization of atoms and molecules

Although we derived Eqn. (2.18) for an atom, it can be used to estimate the energy shift in a diatomic molecule like ThO, since the relativistic enhancement of the eEDM is still determined by the enhancement in the heavy atom. However, the

mixing coefficients  $\epsilon_s$  and  $\epsilon_p$  for a molecule can have quite different values from those for an atom.

To see this, let's consider an atom with a valence electron in an  $|s_{1/2}\rangle$  state in an applied electric field  $\mathcal{E}_e = \mathcal{E}_e \hat{z}$ . For atoms, perturbation theory is valid for any practically achievable  $\mathcal{E}_e$ , so the mixing coefficients are

$$\epsilon_s \simeq 1 \quad (2.19)$$

$$\epsilon_p \simeq -\mathcal{E}_e \frac{\langle g_{p_{1/2}} | e z | g_{s_{1/2}} \rangle}{E_{s_{1/2}} - E_{p_{1/2}}}. \quad (2.20)$$

If we make the approximations

$$\begin{aligned} \langle g_{p_{1/2}} | e z | g_{s_{1/2}} \rangle &\sim e a_0 \\ E_{p_{1/2}} - E_{s_{1/2}} &\sim 0.1 \frac{e^2}{a_0}, \end{aligned} \quad (2.21)$$

we find  $\epsilon_p \sim \mathcal{E}_e / (5 \times 10^8 \text{ V/cm})$ . Since the largest attainable electric field in a laboratory vacuum is about 200 kV/cm [22], this gives  $\epsilon_p \sim 4 \times 10^{-4}$ . This small value of  $\epsilon_p$  enters directly into the Eqn. (2.18), reducing the size of the energy shift. For atoms in any practically achievable electric field, atomic EDM  $d_a$  is proportional to the applied field  $\mathcal{E}_e$ . Thus, the ratio  $R = d_a/d_e = \mathcal{E}_{eff}/\mathcal{E}_e$  is a constant, which is usually called the enhancement factor. For heavy atoms, this factor can be much larger than one since it scales with atomic number as  $Z^3$ . For thallium, which was used to set the best atomic limit on the eEDM, for instance,  $R = -585$  [23].

Significantly greater polarization can be achieved with polar diatomic molecules. In such molecules, the atomic  $s$  and  $p$  orbitals are strongly polarized along the inter-nuclear axis  $\hat{n}$  by the intermolecular electric field. This mixing of  $s$  and  $p$  orbitals in a the molecule will contribute to an eEDM signal only if it produces a molecular

orbital of  $\sigma$  symmetry. An electron in a  $\sigma$  orbital has no orbital angular momentum around the molecular axis, allowing it to penetrate close to the heavy atom's nucleus, where the relativistic enhancement occurs. To estimate the mixing coefficients, we can express the molecular orbital as a linear combination of atomic orbitals centered on the heavy atom [21]

$$|\sigma\rangle = \epsilon_s |s\rangle + \epsilon_p \left[ -\frac{2\omega}{\sqrt{3}} |p_{1/2}\rangle + \sqrt{\frac{2}{3}} |p_{3/2}\rangle \right] + \dots \quad (2.22)$$

Here  $\omega$  is the spin projection on the molecular axis,  $\omega = \pm 1/2$ , and we have neglected the contributions of  $d$  and higher orbitals and of all orbitals centered on the light atom since these will not contribute to the *eEDM* signal. In this case, the mixing coefficients  $\epsilon_s$  and  $\epsilon_p$  are properties of the molecular orbital and do not depend on the applied electric field.

Applying an electric field is still essential in a molecular *eEDM* experiment to orient the molecular axis in the laboratory frame. In the absence of this polarizing field, energy eigenstates of the molecule are also parity eigenstates. For a heteronuclear molecule, parity eigenstates are equal linear combinations of states with opposite orientations of the molecular axis and hence of the intermolecular electric field. In such a state, the *eEDM* is antiparallel to the molecular electric field as often as it is parallel to the field, so the net energy shift is zero. When the molecule is polarized by an applied field, however, the parity states mix to produce new energy eigenstates in which the molecular axis is either parallel or antiparallel to the applied field, as we will see in Section 3.0.2.

Since polarization occurs through the mixing of opposite parity states by the applied electric field, polarizing a molecule requires a much smaller electric field than

polarizing an atom, as the molecular states of opposite parity are much closer in energy than atomic states. Every molecule has rotational states whose splitting  $\Delta_{rot}$  is related to a typical electronic energy  $\Delta_{el}$  by  $\Delta_{rot} \sim (m_e/M_{nuc})\Delta_{el} \sim 10^{-4}\Delta_{el}$ . Some molecules have opposite parity states with even smaller splittings due to  $\Omega$ -doubling, which we will discuss in Section 3.0.2. The presence of such closely spaced opposite parity states makes complete polarization achievable for realistic values of the applied field. For instance, for ThO in the  $H$  state, the polarization is 0.999 for  $\mathcal{E}_e = 10$  V/cm. The effective electric field in a fully polarized molecule like ThO is thus about  $10^3$  times larger than the largest effective field achievable in an atom because the atomic field is limited by the achievable degree of polarization. Now that techniques for producing large numbers of cold molecules are available [24, 25, 26], many molecular *eEDM* experiments have been started to take advantage of this feature (see [5] and [27] for reviews of current molecular *eEDM* experiments).

## Chapter 3

# Diatomic molecules for eEDM measurements

In this chapter, we briefly review some features of diatomic molecules that are relevant for the ACME experiment. A more detailed introduction to molecules can be found in [28], while the definitive treatment is [29].

A molecule has more degrees of freedom than an atom due to the vibrational and rotational motion of the nuclei. Since the Coulomb forces experienced by electrons and nuclei in a molecule are comparable in strength, but the nuclei are at least three orders of magnitude heavier, the nuclear motion is much slower than the electronic motion. This makes it a good approximation to treat these motions independently and calculate the electronic wavefunction at each value of the internuclear separation by treating the nuclei as fixed. This is called the Born-Oppenheimer approximation. The electronic charge distribution is then a function of the internuclear separation and determines the nuclear motion. This leads to the energy level structure shown



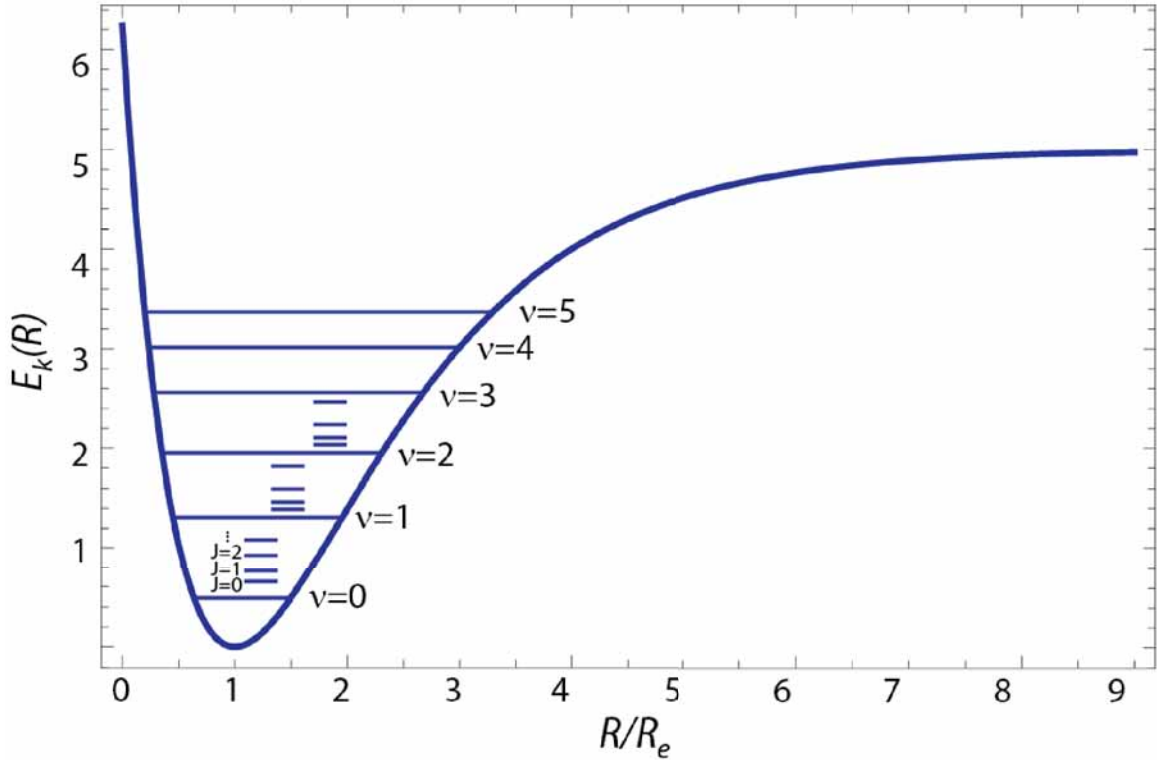


Figure 3.1: Plot of the electronic energy  $E_k(R)$  as a function of the internuclear separation  $R$ . Each electronic state  $k$  is described by a curve of this general shape. For  $R \rightarrow 0$ , the energy is dominated by the mutual repulsion of the nuclei, while for  $R \rightarrow \infty$ , it approaches a constant equal to the sum of the energies of two separated atoms. For a bound state, the energy has a minimum at some intermediate distance  $R_e$ . Within each electronic state, there is a set of vibrational states labeled by the quantum number  $v$ , and within each vibrational state is a series of rotational states labeled by the quantum number  $J$ .

schematically in Fig. 3.1.

In an atom, the total electronic angular momentum  $\mathbf{J}_e^2$  is identical with the total angular momentum of the atom<sup>1</sup>. Rotational invariance of the Hamiltonian means that energy eigenstates can be chosen to be simultaneous eigenstates of  $\mathbf{J}_e^2$  (quantum number  $J_e$ ) and its projection on an arbitrarily chosen  $z$ -axis  $J_{ez}$  (quantum number

<sup>1</sup>We ignore nuclear spin here and throughout this chapter, since it is irrelevant for ThO in which both nuclei have spin 0.

$M_e$ ). In a diatomic molecule, the spherical symmetry of the Hamiltonian is reduced to axial symmetry around the internuclear axis  $\hat{\mathbf{n}}$ <sup>2</sup>, which means that  $\mathbf{J}_e^2$  no longer commutes with the Hamiltonian and  $M_e$  is not a good quantum number. However, the Hamiltonian still commutes with  $J_{ez}$  when the  $z$ -axis is chosen to coincide with the internuclear axis. The eigenvalue  $\Omega$  of the projection of the electronic angular momentum on the internuclear axis,  $\mathbf{J}_e \cdot \hat{\mathbf{n}}$ , thus remains a good quantum number. The total angular momentum  $\mathbf{J}$  of the molecule is  $\mathbf{J} = \mathbf{N} + \Omega \hat{\mathbf{n}}$ , where  $\mathbf{N}$  is the rotational angular momentum of the nuclei, which is always perpendicular to  $\hat{\mathbf{n}}$ . Due to rotational invariance, the total angular momentum  $\mathbf{J}^2$  commutes with the Hamiltonian, and its eigenvalue  $J$  is used to label the rotational states of the molecule. The possible values of  $J$  are  $|\Omega|, |\Omega| + 1, |\Omega| + 2, \dots$ .

The various angular momenta in the molecule can couple together in different ways, which give rise to the different Hund's cases. Each case leads to a set of good (i.e. well-defined) quantum numbers that can be used to label the molecular states. The most important ones for our purposes are Hund's case (a) and Hund's case (c). In case (a), the electronic orbital angular momentum  $\mathbf{L}$  is coupled to the internuclear axis  $\hat{\mathbf{n}}$  by the internal electric field of the molecule and precesses about  $\hat{\mathbf{n}}$  with projection  $\Lambda$  on the axis. Spin-orbit coupling then couples the total electronic spin  $\mathbf{S}$  to the axis via its interaction with  $\mathbf{L}$ , so  $\mathbf{S}$  also precesses around the internuclear axis with projection  $\Sigma$  on the axis. In this case, the good quantum numbers are  $\Lambda$ ,  $S$ ,  $\Sigma$ , and  $\Omega = |\Lambda + \Sigma|$ . The ground state of ThO can be described by Hund's case (a). Since thorium is heavy, most excited states of ThO are described by Hund's case (c),

---

<sup>2</sup>The internuclear axis  $\hat{\mathbf{n}}$  is usually defined to point in the direction of the molecular electric dipole moment in the molecule-fixed frame.

which occurs when the spin-orbit coupling is stronger than the coupling of  $\mathbf{L}$  to the internuclear axis. In this case,  $\mathbf{L}$  and  $\mathbf{S}$  first couple together to form the total electronic angular momentum  $\mathbf{J}_e = \mathbf{L} + \mathbf{S}$ , which precesses around the internuclear axis  $\hat{\mathbf{n}}$  with projection  $\Omega$  on this axis. Due to the strong spin-orbit coupling in Hund's case (c),  $\Lambda$ ,  $\Sigma$ , and  $S$  are no longer good quantum numbers; the only good quantum number in this case is  $\Omega$ .

In analogy with atomic states, molecular states can be described by the notation  $^{2S+1}\Lambda_\Omega$ , where  $S$  is the total electronic spin (eigenvalue of  $\mathbf{S}^2$ ) and  $\Lambda$  is the projection of  $\mathbf{L}$  on the internuclear axis. The value of  $\Lambda$  is represented by a capital Greek letter in analogy with the atomic case:  $\Sigma$  ( $\Lambda = 0$ ),  $\Pi$  ( $\Lambda = 1$ ),  $\Delta$  ( $\Lambda = 2$ ), ... For instance, the ground state of ThO, called  $X$ , is essentially a pure  $^1\Sigma^+$  state<sup>3</sup>.

The  $^{2S+1}\Lambda_\Omega$  notation assumes that  $\Lambda$  and  $S$  are well-defined, which is not true in Hund's case (c). Although states of ThO can generally not be described by a single term of the form  $^{2S+1}\Lambda_\Omega$ , they can be expressed as linear combinations of such terms with differing values of  $S$  and  $\Lambda$  but the same value of  $\Omega$ . For instance, *ab initio* molecular calculations indicate that the *eEDM*-sensitive  $H$  state of ThO is 98.4%  $^3\Delta_1$ , with small admixtures of  $^3\Pi_1$  and  $^1\Pi_1$  states [30].

### 3.0.1 Calculation of molecular matrix elements

To determine the effect of external fields on a molecule, we need to relate matrix elements of operators expressed in the laboratory-fixed coordinate system to matrix

---

<sup>3</sup>The subscript  $\Omega$  is omitted in this case since the only possible value is  $\Omega = 0$ . The  $+$  superscript describes the fact that the wavefunction of this state is even under reflection through a plane containing the internuclear axis. There are also  $\Sigma^-$  states for which the wavefunction is odd under this reflection.

elements expressed in the molecule-fixed system. Since the molecule-fixed axes are obtained by rotation of the space-fixed axes by the Euler angles  $(\phi, \theta, \chi) = \omega$ , a spherical tensor operator  $T_p^{(k)}$  in the laboratory-fixed system can be expressed in terms of molecule-fixed components  $T_n^{(k)}$  as ([29], 5.143)

$$T_p^{(k)} = \sum_n \mathcal{D}_{pn}^{(k)}(\omega)^* T_n^{(k)}, \quad (3.1)$$

where  $\mathcal{D}_{pn}^{(k)}(\omega)^*$  is the complex conjugate of the  $pn$  element of the  $k$ -th rank rotation matrix  $\mathcal{D}^{(k)}(\omega)$ . We use  $p$  to label space-fixed coordinates and  $n$  for molecule-fixed coordinates. The rotational part of the wavefunction for a diatomic molecule can be written as ([29], 5.145)

$$|J, M, \Omega\rangle = \sqrt{\frac{2J+1}{8\pi^2}} \mathcal{D}_{M\Omega}^{(J)}(\omega)^* \quad (3.2)$$

Using Eqns. (3.1) and (3.2), as well as the formula for the integral over a product of three rotation matrices ([29], 5.100), we find the following relation between matrix elements in the laboratory-fixed ( $p$ ) and molecule-fixed ( $n$ ) frames

$$\begin{aligned} \langle \beta', J', M', \Omega' | T_p^{(k)} | \beta, J, M, \Omega \rangle &= \sum_n (-1)^{M'-\Omega'} \sqrt{(2J+1)(2J'+1)} \\ &\quad \begin{pmatrix} J' & k & J \\ -M' & p & M \end{pmatrix} \begin{pmatrix} J' & k & J \\ -\Omega' & n & \Omega \end{pmatrix} \langle \beta', \Omega' | T_n^{(k)} | \beta, \Omega \rangle, \end{aligned} \quad (3.3)$$

where  $\beta$  represents all additional quantum numbers required to specify the state. We will need this formula in Section 3.1.

For matrix elements that are diagonal in  $\Omega$ , we will also need the  $n = 0$  spherical component of the electric dipole moment operator  $\mathbf{D}$  in the molecule-fixed frame. Since the  $z$ -axis of the molecular frame is the internuclear axis and the electric dipole

moment lies along this axis,  $D_0 = D_{mol}$ , where  $D_{mol}$  is the magnitude of the electric dipole moment for the electronic state under consideration. The matrix element is thus simply  $\langle \Omega | D_0 | \Omega \rangle = D_{mol}$ .

### 3.0.2 Omega doubling

The Hamiltonian of a diatomic molecule is invariant under reflection through a plane passing through the internuclear axis. Such a reflection does not change the energy of the molecule, but it does change the sign of the angular momentum about this axis. Thus, for  $\Omega \neq 0$ , there are two degenerate states with opposite signs of the angular momentum about the internuclear axis,  $\Omega = \pm|\Omega|$ . Since these states transform under parity as ([29], 6.228)

$$P|J, M, \Omega\rangle = (-1)^{J-\Omega}|J, M, -\Omega\rangle, \quad (3.4)$$

simultaneous eigenstates of the molecular Hamiltonian and parity can be constructed by taking the following linear combinations of states with signed values of  $\Omega$

$$|\beta, J, M, |\Omega|, \pm\rangle = \frac{1}{\sqrt{2}}(|\beta, J, M, \Omega\rangle \pm (-1)^{-\Omega}|\beta, J, M, -\Omega\rangle). \quad (3.5)$$

Here  $\beta$  represents all other quantum numbers, for instance those specifying the electronic and vibrational state. The states  $|\beta, J, M, |\Omega|, \pm\rangle$  are conventionally denoted  $|\beta, J, M, |\Omega|, e\rangle$  with parity  $(-1)^J$  and  $|\beta, J, M, |\Omega|, f\rangle$  with parity  $(-1)^{J+1}$  [29]. These states are degenerate in the absence of molecular rotation. The degeneracy is lifted by a coupling between the electronic and rotational motion, and the resulting energy splitting is called  $\Omega$ -doubling. Thus, for  $\Omega \neq 0$ , each rotational level consists of two

closely spaced states of opposite parity corresponding to the linear combinations in Eqn. (3.5).

To see how  $\Omega$ -doubling arises, we write the rotational part of the Hamiltonian as

$$H_{rot} = B\mathbf{N}^2 = B(\mathbf{J} - \mathbf{J}_e)^2 = B\mathbf{J}^2 - 2B\mathbf{J} \cdot \mathbf{J}_e + B\mathbf{J}_e^2, \quad (3.6)$$

where  $B$  is the rotational constant. The first term in Eqn. (3.6) is the usual rotational energy, while the third term is a constant for a given electronic state. The second term,  $H' = -2B\mathbf{J} \cdot \mathbf{J}_e$ , is responsible for  $\Omega$ -doubling. The most general matrix element of this term is

$$\mathcal{M} = \langle \beta', J', M', \Omega' | H' | \beta, J, M, \Omega \rangle = -2B \sum_p (-1)^p \langle \beta', J', M', \Omega' | J_p J_{e,-p} | \beta, J, M, \Omega \rangle, \quad (3.7)$$

where in the second part of Eqn. (3.7) we have written out the scalar product  $\mathbf{J} \cdot \mathbf{J}_e$  in terms of spherical components. Inserting the identity as a sum over eigenstates, we have

$$\mathcal{M} = -2B \sum_{\substack{p, \beta'', J'', \\ M'', \Omega''}} \langle \beta', J', M', \Omega' | J_p | \beta'', J'', M'', \Omega'' \rangle \langle \beta'', J'', M'', \Omega'' | J_{e,-p} | \beta, J, M, \Omega \rangle. \quad (3.8)$$

We evaluate the matrix element of  $J_p$  using the Wigner-Eckart theorem and the formula ([31], 4.148)

$$\langle \beta', J', \Omega' | J | \beta'', J'', \Omega'' \rangle = \delta_{\beta' \beta''} \delta_{J' J''} \delta_{\Omega' \Omega''} \sqrt{J'(J' + 1)(2J' + 1)}, \quad (3.9)$$

which leads to

$$\mathcal{M} = -2B \sqrt{J'(J' + 1)(2J' + 1)} \sum_{p, M''} \begin{pmatrix} J' & 1 & J' \\ -M' & p & M'' \end{pmatrix} \langle \beta', J', M'', \Omega' | J_{e,-p} | \beta, J, M, \Omega \rangle. \quad (3.10)$$

Using Eqn. (3.3) to express the matrix element of  $J_e$  in terms of molecule-fixed components, we find

$$\begin{aligned} \mathcal{M} = & -2B\sqrt{J'(J'+1)(2J'+1)}(-1)^{J'-M'-\Omega'} \sum_n \begin{pmatrix} J' & 1 & J \\ -\Omega' & n & \Omega \end{pmatrix} \langle \beta', \Omega' | J_{e,n} | \beta, \Omega \rangle \\ & \sum_{p, M''} (-1)^{p+M''} \begin{pmatrix} J' & 1 & J' \\ -M' & p & M'' \end{pmatrix} \begin{pmatrix} J' & 1 & J \\ -M'' & -p & M \end{pmatrix}. \end{aligned} \quad (3.11)$$

Performing the sum over  $p$  and  $M''$  using the orthogonality relation of the  $3j$  symbols ([31], 4.42), we have

$$\mathcal{M} = -2B(-1)^{J-\Omega'} \sqrt{J(J+1)(2J+1)} \sum_n \begin{pmatrix} J & 1 & J \\ -\Omega' & n & \Omega \end{pmatrix} \langle \beta', \Omega' | J_{e,n} | \beta, \Omega \rangle. \quad (3.12)$$

Since  $J_e$  is a vector operator, Eqn. (3.12) tells us that the only non-zero matrix elements are those where  $\Omega' = \Omega, \Omega \pm 1$ . We first consider the diagonal elements, which would give a first-order energy shift. Since the parity eigenstates in the absence of external fields are equal linear combinations of  $|\Omega\rangle$  and  $|- \Omega\rangle$  (Eqn. (3.5)), the first order energy shift vanishes.

There is a second order energy shift due to coupling of states with  $\Delta\Omega = \pm 1$ . Note that for coupling to states with  $\Omega = 0$ , only one of the two parity states of the  $\Omega$ -doublet is shifted, the one that has the same parity as the levels of the  $\Omega = 0$  state. This occurs because the operator  $\mathbf{J} \cdot \mathbf{J}_e$  has even parity. For the  $H$  state  $J = 1$  level, the shift arises from coupling to states with  $\Omega = 0^4$ . The closest  $\Omega = 0$  states to the

$H$  state are the  $A$  state and the ground state  $X$ , which are both about  $5300 \text{ cm}^{-1}$

---

<sup>4</sup>The closest state to the  $H$  state is the  $Q$  state with  $\Omega = 2$ , which is only about  $800 \text{ cm}^{-1}$  away [32]. The  $Q$  state does not contribute to  $\Omega$ -doubling for the  $J = 1$  level in  $H$  since it doesn't have a  $J = 1$  state but contributes for  $J = 2$  and above. Due to the  $\Omega$ -doubling in the  $Q$  state, coupling to this state shifts both the  $e$  and  $f$  levels of the  $H$  state in the same direction. If the matrix elements are similar in magnitude, the shifts of the  $e$  and  $f$  levels should be similar, so the contribution of this state to  $\Omega$ -doubling is expected to be fairly small.

away [32]. Since  $A$  is above  $H$  in energy while  $X$  is below, they will shift the  $e$  levels of the  $H$  state in opposite directions. From Eqn. (3.12), the second-order energy shift is

$$\Delta E = 4B_H^2 \left( \frac{|\langle A, 0 | J_{e,-1} | H, 1 \rangle|^2}{E_H - E_A} + \frac{|\langle X, 0 | J_{e,-1} | H, 1 \rangle|^2}{E_H - E_X} \right) J(J+1). \quad (3.13)$$

If we assume that the unknown matrix elements  $|\langle A, 0 | J_{e,-1} | H, 1 \rangle|$  and  $|\langle X, 0 | J_{e,-1} | H, 1 \rangle|$  are both of order one, Eqn. (3.13) predicts a splitting of 29 kHz for  $J = 1$ . This simple estimate is not too far off: existing spectroscopic data on ThO yield a value of  $q = 192$  kHz for the  $\Omega$ -doubling constant [33, 34], which gives a splitting of  $\Delta_\Omega = qJ(J+1) = 384$  kHz for  $J = 1$ .

### 3.1 The $H$ state in electric and magnetic fields

The  $J = 1$   $\Omega$ -doublet in the  $H$  state of ThO is the heart of the ACME experiment. In this section, we determine the shifts of levels in this manifold due to applied electric and magnetic fields.

Ignoring the very small  $eEDM$  for now, we start with the much larger effect of an electric field  $\mathcal{E}_e = \mathcal{E}_e \hat{z}$  on the  $\Omega$ -doublet. This field mixes the  $|e\rangle$  (parity -1) and  $|f\rangle$  (parity +1) states with the same value of  $M$ . Using Eqns. (3.3) and (3.5), the dipole moment matrix element between the states  $|J, M, |\Omega|, e\rangle$  and  $|J, M, |\Omega|, f\rangle$  is

$$\begin{aligned} \langle e | -\mu_{z,lab} \mathcal{E}_e | f \rangle &= \frac{1}{2} (\langle J, M, \Omega | \mu_{z,lab} | J, M, \Omega \rangle - \langle J, M, -\Omega | \mu_{z,lab} | J, M, -\Omega \rangle) \\ &= \frac{-D_{mol} \mathcal{E}_e |\Omega| M}{J(J+1)}. \end{aligned} \quad (3.14)$$



The Hamiltonian in the  $|e\rangle, |f\rangle$  basis for  $M = \pm 1$  is

$$H = \begin{pmatrix} \Delta_\Omega/2 & \frac{-D_{mol}\mathcal{E}_e|\Omega|M}{J(J+1)} \\ \frac{-D_{mol}\mathcal{E}_e|\Omega|M}{J(J+1)} & -\Delta_\Omega/2 \end{pmatrix}, \quad (3.15)$$

where  $\Delta_\Omega$  is the splitting between the  $\Omega$ -doublet states in the absence of an electric field. To simplify the notation<sup>5</sup>, we define  $x = \Delta_\Omega/2$  and  $y = -D_{mol}\mathcal{E}_e|\Omega|M/[J(J+1)]$ . Now let  $r = \sqrt{x^2 + y^2}$  and  $\theta = \arctan(y/x)$ , so that the Hamiltonian becomes

$$H = \begin{pmatrix} r \cos \theta & r \sin \theta \\ r \sin \theta & -r \cos \theta \end{pmatrix}. \quad (3.16)$$

The eigenstates can be written as

$$\begin{aligned} |\psi_H\rangle &= \cos \frac{\theta}{2} |e\rangle + \sin \frac{\theta}{2} |f\rangle \\ |\psi_L\rangle &= -\sin \frac{\theta}{2} |e\rangle + \cos \frac{\theta}{2} |f\rangle, \end{aligned} \quad (3.17)$$

where  $H$  ( $L$ ) labels the higher (lower) energy state. The  $M = 0$  states do not mix and remain parity eigenstates regardless of the electric field. In the limit of large electric field,  $\theta \rightarrow \mp\pi/2$  for the  $M = \pm 1$  states. In this case, we have

$$\begin{aligned} |\psi_H, M = +1\rangle &= \frac{1}{\sqrt{2}} (|e\rangle - |f\rangle) \\ |\psi_H, M = -1\rangle &= \frac{1}{\sqrt{2}} (|e\rangle + |f\rangle) \\ |\psi_L, M = +1\rangle &= \frac{1}{\sqrt{2}} (|e\rangle + |f\rangle) \\ |\psi_L, M = -1\rangle &= -\frac{1}{\sqrt{2}} (|e\rangle - |f\rangle). \end{aligned} \quad (3.18)$$

In this limit, the parity states are completely mixed and the signed values of  $\Omega$  are again good quantum numbers. To confirm this statement, we express the fully mixed

---

<sup>5</sup>This section owes a great debt to and appropriates much of the notation of [35].

states in the  $|\Omega\rangle, |-\Omega\rangle$  basis using Eqn. (3.5). The result is

$$\begin{aligned} |\psi_H, M = +1\rangle &= -|-\Omega\rangle \\ |\psi_H, M = -1\rangle &= |\Omega\rangle \\ |\psi_L, M = +1\rangle &= |\Omega\rangle \\ |\psi_L, M = -1\rangle &= |-\Omega\rangle. \end{aligned} \quad (3.19)$$

The fully mixed states correspond to alignment of the internuclear axis parallel or antiparallel to the applied field, as we can demonstrate by calculating the expectation value of the molecular electric dipole moment  $\mathbf{D}$  in such a state. For a state of fixed  $M$ , only the  $z$ -component of  $\mathbf{D}$  has non-zero expectation value, which is given by

$$\langle J, M, \Omega | D_{z,lab} | J, M, \Omega \rangle = \frac{M\Omega}{J(J+1)} D_{mol}. \quad (3.20)$$

Eqn. (3.20) tells us that states  $M\Omega < 0$  (i.e.  $|\psi_H, M = \pm 1\rangle$ ) correspond to the molecular electric dipole moment oriented antiparallel to the electric field, while states with  $M\Omega > 0$  (i.e.  $|\psi_L, M = \pm 1\rangle$ ) correspond to the opposite orientation. This makes intuitive sense: the energy of the state with its dipole moment parallel to the electric field decreases, while that of the state polarized antiparallel to the field increases. We can characterize the fully mixed states by the quantum number  $\mathcal{N} = \text{sign}(\hat{\mathbf{n}} \cdot \boldsymbol{\mathcal{E}}_e) = \text{sign}(M)\text{sign}(\Omega)$ . Thus,  $\mathcal{N} = -1$  ( $\mathcal{N} = +1$ ) for the higher (lower) energy state.

The energies of the states  $|\psi_H, M = \pm 1\rangle$  and  $|\psi_L, M = \pm 1\rangle$  in the electric field are

$$E_{\mathcal{N}} = -\mathcal{N} \sqrt{\left(\frac{\Delta_{\Omega}}{2}\right)^2 + \left(\frac{D_{mol}\mathcal{E}_e|\Omega|M}{J(J+1)}\right)^2}. \quad (3.21)$$

Using  $D_{mol} = 2.13$  MHz/V/cm [36] and  $\Delta_{\Omega} = 384$  kHz [33, 34] for the  $H$  state of ThO, for  $\mathcal{E}_e$  larger than about 18 V/cm, the Stark shift of the  $M = \pm 1$  levels relative

to their unperturbed energies becomes linear in the external field with a slope of 1 MHz/V/cm. In the absence of an *eEDM*, the energies don't depend on the sign of  $M$ . This is an example of Kramers degeneracy, which is a consequence of time-reversal invariance [37].

The effect of a magnetic field  $\mathbf{B} = B\hat{z}$  can be described by the effective Hamiltonian  $H_Z^{\text{eff}} = g_N\mu_B\mathbf{J} \cdot \mathbf{B}$ , where  $g_N$  is the  $g$ -factor of the state  $\mathcal{N}$  [38]. This shifts the levels by an amount  $\delta_Z = g_N\mu_B BM$ . The  $g$ -factors for the  $\mathcal{N} = \pm 1$  states differ by a few parts per thousand and also depend on the applied electric field [35, 38].

Finally, we consider the additional shift due to the *eEDM* interaction  $H_{edm} = -\mathbf{d}_e \cdot \mathcal{E}_{eff}$ . This can be expressed in terms of an effective Hamiltonian is  $H_{edm} = d_e\mathcal{E}_{eff}\mathbf{J}_e \cdot \hat{\mathbf{n}}$  [39], so that  $\langle J, M, \Omega | H_{edm} | J, M, \Omega \rangle = d_e\mathcal{E}_{eff}\Omega$ . Since the energy shift is proportional to the expectation value of  $\Omega$ , it vanishes in the absence of an applied electric field, when the molecule is in a parity eigenstate. If we define the polarization by  $\mathcal{P} = \langle \Omega \rangle / |\Omega|$ , the *eEDM* shift is  $\delta_{d_e} = \mathcal{P}d_e\mathcal{E}_{eff}$ . From Eqns. (3.5) and (3.17), the polarization is

$$\begin{aligned} \mathcal{P}_{\mathcal{N}} &= -\mathcal{N} \left[ \cos^2 \left( \frac{\theta}{2} - \frac{\pi}{4} \right) - \sin^2 \left( \frac{\theta}{2} - \frac{\pi}{4} \right) \right] = -\mathcal{N} \sin \theta \\ &= \mathcal{N} \frac{\frac{D_{mol}\mathcal{E}_e|\Omega|M}{J(J+1)}}{\sqrt{\left( \frac{D_{mol}\mathcal{E}_e|\Omega|M}{J(J+1)} \right)^2 + \frac{\Delta_{\Omega}^2}{4}}}. \end{aligned} \quad (3.22)$$

For a fully polarized state,  $\mathcal{P}_{\mathcal{N}} = \mathcal{N}\text{sign}(M)$ . The polarization of the  $J = 1$  state is shown in Fig. 3.2.

Fig. 3.3 shows the energy levels of  $J = 1$   $\Omega$ -doublet in the presence of parallel electric and magnetic fields. The total energy of the  $|M, \mathcal{N}\rangle$  state due to the Stark, Zeeman, and *eEDM* interactions is  $E[M, \mathcal{N}] = E_{\mathcal{N}} + g_N\mu_B BM + \mathcal{N}\text{sign}(M) d_e \mathcal{E}_{eff}$ .

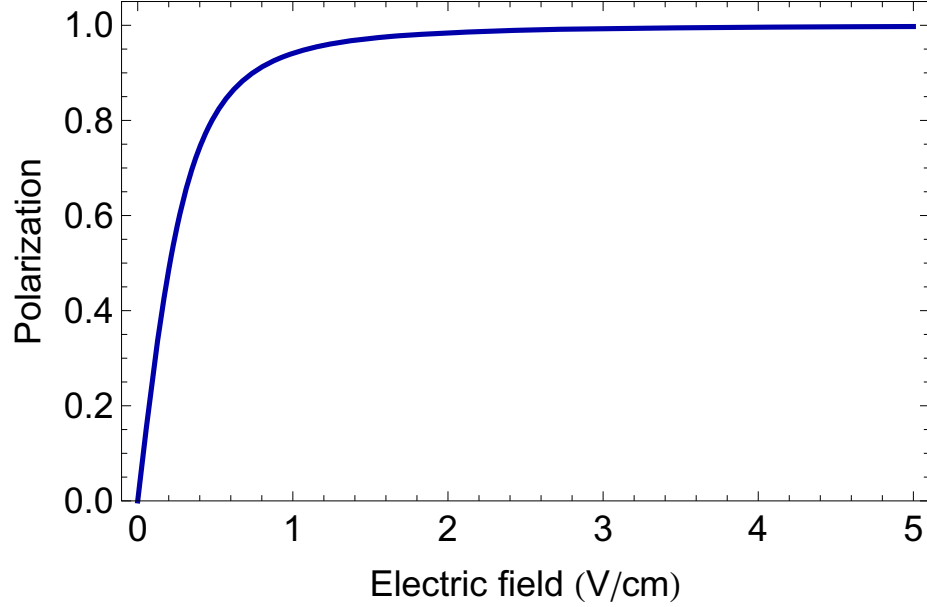


Figure 3.2: Polarization  $\mathcal{P}$  of the  $J = 1$  level of the  $H$  state as a function of the applied electric field.

The energy difference between the  $M = +1$  and  $M = -1$  states is

$$\Delta_{edm}[\mathcal{N}] = E[1, \mathcal{N}] - E[-1, \mathcal{N}] = 2(g_N \mu_B B + \mathcal{N} d_e \mathcal{E}_{eff}). \quad (3.23)$$

Note that the  $eEDM$  shift has opposite signs in the upper ( $\mathcal{N} = -1$ ) and lower ( $\mathcal{N} = +1$ ) pair of states, which is a consequence of the opposite orientation of the molecular electric field in these states. In effect, switching between the  $\mathcal{N} = +1$  and  $\mathcal{N} = -1$  levels allows us to reverse the direction of the electric field acting on the  $eEDM$  without reversing the applied electric field. In the limit that the  $g$ -factors are equal, the difference  $\Delta_{edm}[1] - \Delta_{edm}[-1] = 4 d_e \mathcal{E}_{eff}$  is independent of the magnetic field and hence immune to any magnetic field-induced systematic effects. The idea of using a polarized  $\Omega$ -doublet as a comagnetometer in this way was first suggested by D. DeMille [40].

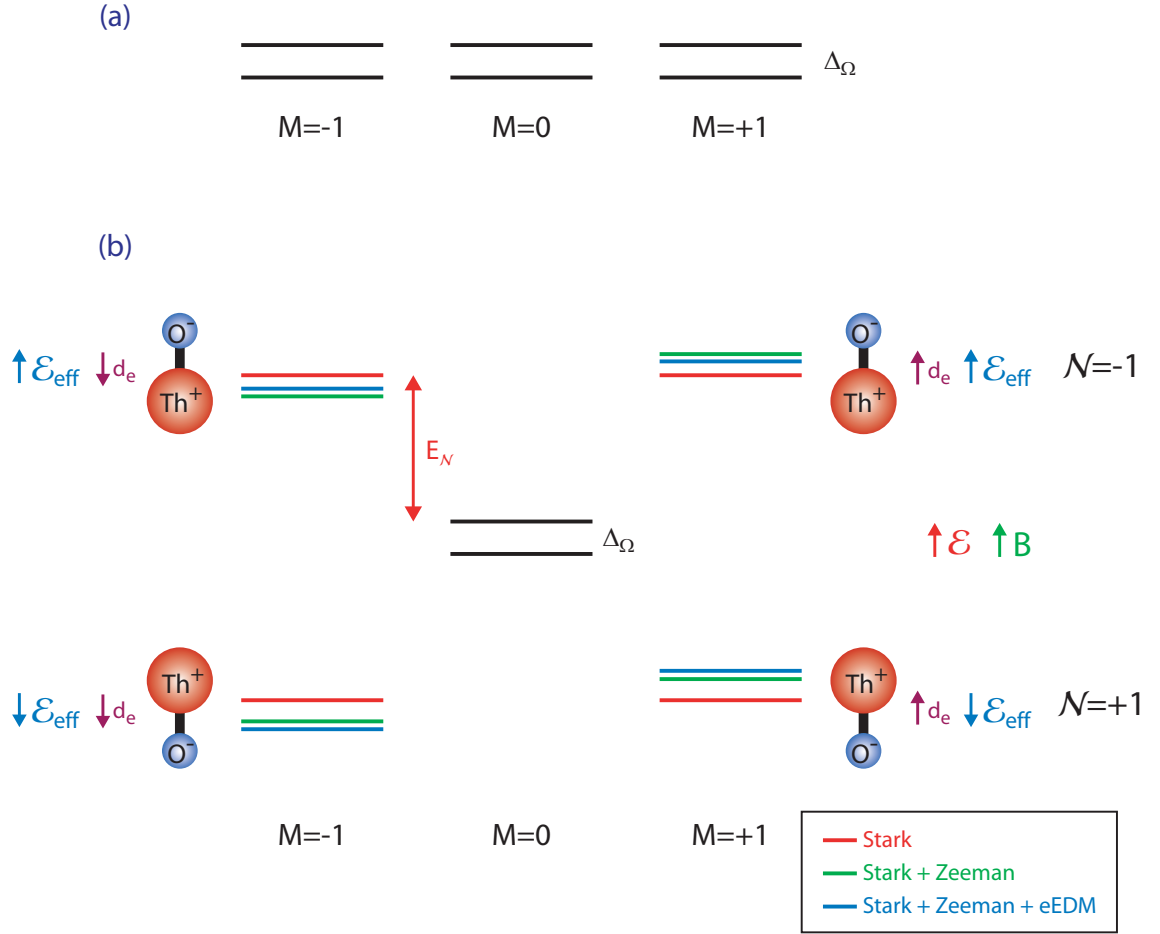


Figure 3.3: (a)  $J = 1$  level  $\Omega$ -doublet in the absence of external fields. The splitting is  $\Delta_\Omega \approx 384$  kHz. (b)  $J = 1$   $\Omega$ -doublet in applied electric and magnetic fields.

# Chapter 4

## The ACME experiment

The ACME collaboration aims to exploit the eEDM sensitivity of polar diatomic molecules by performing an eEDM measurement using thorium monoxide (ThO) [41]. ThO was selected for its high sensitivity to  $d_e$  and experimental simplicity. This chapter describes the planned experiment.

### 4.1 Thorium monoxide

In forming ThO, thorium ( $[\text{Rn}]7s^26d^2$ ) gives two of its electrons to oxygen ( $[\text{He}]2s^22p^4$ ) to complete its  $2p$  shell. The ground state of ThO then corresponds to the configuration  $\text{Th}^{2+}(7s^2)\text{O}^{2-}(2p^6)$ , while the low-lying excited states arise from excitations of one of thorium's  $7s$  electrons to the  $6d$  orbital [30, 42]. The metastable  $H$  state of interest for the eEDM measurement is of  $(s\sigma d\delta)$   $^3\Delta$  symmetry [43]. This means that there are two unpaired electrons in this state, one in a  $\sigma$  orbital and one in a  $\delta$

orbital<sup>1</sup>. Only the electron in the  $\sigma$  orbital has significant probability of penetrating close to the thorium nucleus, where the relativistic enhancement of the eEDM arises, so this is the electron responsible for the eEDM signal.

The energy levels of ThO are well known due to extensive spectroscopic [44, 33, 32, 34, 42] and theoretical [30, 45] studies. The electronic states relevant for the eEDM measurement are shown in Fig. 4.1. The  $H$  state has  $|\Omega| = 1$ , so each rotational level consists of a doublet of opposite parity states. For  $J = 1$ , the rotational level of interest for the eEDM measurement, the  $\Omega$ -doublet splitting is  $\Delta_\Omega = 384$  kHz [33, 34]. This makes the molecule easily polarizable in an electric field. The critical field at which the Stark shift is equal to the  $\Omega$ -doublet splitting is  $\mathcal{E}_c = \Delta_\Omega/\mu_H$ , where  $\mu_H = D_{mol}/2$  is electric dipole moment in the  $H$  state. Using  $D_{mol} = 2.13(2)$  MHz/(V/cm) [36], we find  $\mathcal{E}_c \approx 0.4$  V/cm for  $J = 1$ . Thus, for a realistic field of  $\sim 100$  V/cm, the molecule will be completely polarized. The calculated effective electric field for fully polarized ThO in the  $H$  state is  $\mathcal{E}_{eff} = 104$  GV/cm [43]. The effective field is the quantity that determines the eEDM energy shift,  $\Delta E_{edm} = -\mathbf{d}_e \cdot \mathcal{E}_{eff}$ .

As pointed out in [43],  $^3\Delta_1$  states like the  $H$  state in ThO are particularly advantageous for eEDM experiments because they are relatively insensitive to magnetic fields. In such a state,  $\Lambda = 2$  and  $\Sigma = -1$  (the latter follows because  $\Omega = |\Lambda + \Sigma| = 1$ ). The effective  $g$ -factor for the state is  $g_{eff} = g_L\Lambda + g_S\Sigma \sim 0$  since  $g_L = 1$  and  $g_S = 2.002$  [46]. A small non-zero value of  $g_{eff}$  arises due to spin-orbit mixing with other electronic states having different values of  $\Lambda$  and  $\Sigma$ . A measurement of the magnetic moment of the  $H$  state gave  $\mu_H = (8.5 \pm 0.5) \times 10^{-3} \mu_B$  [36], confirming this prediction. An

---

<sup>1</sup>Lowercase Greek letters label molecular orbitals, while lowercase Latin letters label atomic orbitals. The letter identifies the projection  $\lambda$  of the electron's orbital angular momentum onto the internuclear axis, i.e.  $\sigma$  ( $\lambda = 0$ ),  $\pi$  ( $\lambda = 1$ ),  $\delta$  ( $\lambda = 2$ ), ...

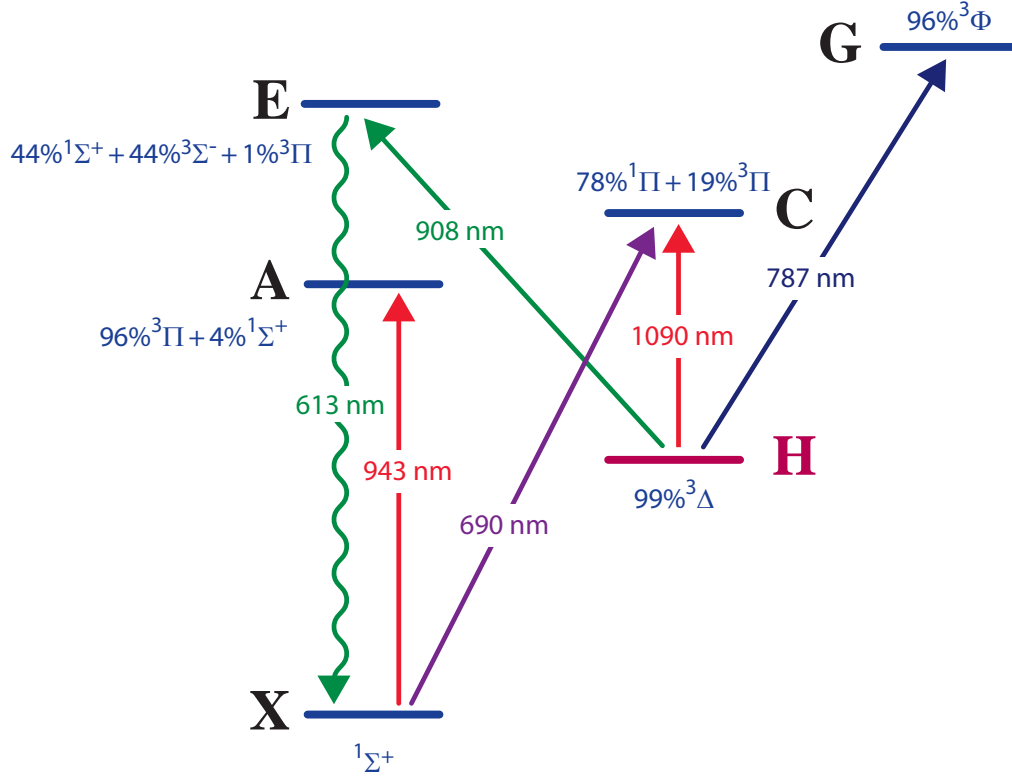


Figure 4.1: Electronic states of ThO relevant for the ACME experiment. Expressions in blue are calculated expansions of each state in terms of  $\Lambda S$  states [30] using the notation  ${}^{2S+1}\Lambda_{\Omega}$ . Arrows indicate transitions important for the experiment, with the wavelength of each transition given by the number on the arrow.

alternative measurement of the  $H$  state magnetic moment will be described in Chapter 6. This small magnetic moment makes the  $H$  state significantly less sensitive to magnetic field noise, an important feature for our experiment since magnetic noise will lead directly to noise in the measured eEDM.



## 4.2 A generic eEDM measurement

Almost every atomic or molecular eEDM experiment can be viewed as an interferometer in which the two arms are states with the electron's spin parallel and antiparallel to the electric field. To understand the basic idea, let's consider a model "atom" with spin 1/2 with enhancement factor  $R$  containing a single unpaired electron. At  $t = 0$ , the spin is prepared to lie along  $\hat{\mathbf{x}}$ :

$$|\psi(0)\rangle = \frac{1}{\sqrt{2}} \begin{pmatrix} 1 \\ 1 \end{pmatrix}. \quad (4.1)$$

This state is then left to evolve in electric  $\mathcal{E}$  and magnetic  $\mathbf{B}$  fields, both of which are along the  $z$ -axis. Due to their different Zeeman and eEDM shifts, the two states in the superposition acquire different phases, so that after a time  $\tau$  the state is

$$|\psi(\tau)\rangle = \frac{1}{\sqrt{2}} \begin{pmatrix} e^{i\phi/2} \\ e^{-i\phi/2} \end{pmatrix}, \quad (4.2)$$

where  $\phi = 2(-g\mu_B B/2 + d_e R \mathcal{E})\tau/\hbar$ . To measure the phase difference, we rotate the spin by  $\pi/2$  around  $\hat{\mathbf{y}}$  using the rotation matrix

$$A = \frac{1}{\sqrt{2}} \begin{pmatrix} 1 & -1 \\ 1 & 1 \end{pmatrix}, \quad (4.3)$$

so that the resulting state is

$$|\psi'\rangle = \begin{pmatrix} i \sin \phi/2 \\ \cos \phi/2 \end{pmatrix}. \quad (4.4)$$

If we now measure the population in the spin-up state, the signal from  $N_0$  atoms is  $S = N_0 \sin^2 \phi/2$ . Writing the phase as  $\phi/2 = \phi_B + \phi_E$ , where  $\phi_B = -g\mu_B B\tau/2\hbar$

and  $\phi_E = d_e R \mathcal{E} \tau / \hbar$ , we isolate  $\phi_E$  by performing the experiment with  $\mathcal{E}$  and  $\mathbf{B}$  both parallel and antiparallel. Reversing either  $\mathcal{E}$  or  $\mathbf{B}$  changes the relative sign of  $\phi_E$  with respect to  $\phi_B$ . The maximal change in  $S$  for a given  $\phi_E$  occurs when  $\phi_B = \pm\pi/4$ . Adjusting the magnetic field to give  $\phi_B = \pi/4$  and using the fact that  $\phi_E \ll 1$ , we find

$$S_{\pm} = \frac{N_0}{2} (1 \pm \sin 2\phi_E) = \frac{N_0}{2} (1 \pm 2\phi_E), \quad (4.5)$$

where the  $+$  ( $-$ ) sign applies for  $\mathcal{E} \cdot \mathbf{B} > 0$  ( $\mathcal{E} \cdot \mathbf{B} < 0$ ).

For  $N_0$  molecules measured in a pulse, the uncertainty in the precession angle  $\phi$  due to shot noise is  $\delta\phi_{shot} = \sqrt{1/N_0}$ . The resulting uncertainty in the eEDM is

$$\delta d_e = \frac{\hbar}{2\mathcal{E}_{eff} \tau \sqrt{N_0}}. \quad (4.6)$$

Magnetic field noise also introduces an uncertainty in the phase  $\delta\phi_{mag} = GD$ , where  $G = g\mu_B/\hbar$  and  $D = \left( \int_0^t B_z(t') dt' \right)_{rms}$  is the root-mean-square fluctuation of the magnetic field [5]. The total uncertainty in the phase is obtained by adding the  $\delta\phi_{shot}$  and  $\delta\phi_{mag}$  in quadrature:

$$\delta d_e = \sqrt{\frac{1}{N_0} + (GD)^2} \frac{\hbar}{2\mathcal{E}_{eff} \tau}. \quad (4.7)$$

Eqn. (4.7) shows that increasing the molecule number  $N_0$  only improves the experimental precision until the point where magnetic noise becomes the dominant noise source. Thus, we would like to have  $D \leq 1/G\sqrt{N_0}$ . For the second generation ACME experiment, we expect to detect about  $1.4 \times 10^9$  molecules per pulse [47], which requires  $D \leq 38$  fT·s. The estimated magnetic field noise in our experiment is about 10 times below this limit [47], which means that magnetic field noise will not be a limit even for the second generation of ACME.

### 4.3 ACME measurement scheme

The ACME experiment uses the  $J = 1$  level of the  $H$  state. We summarize the experimental procedure, going from left to right in Fig. 4.2. A cold beam of ThO molecules is produced in the beam source via laser ablation [48] or thermochemical production [49] and buffer gas cooling. The optimized ablation source using neon buffer gas produces a beam of  $3 \times 10^{11}$  molecules/steradian/pulse in the  $J = 0$  rotational level of the ground state  $X$  [48]. This corresponds to  $2.36 \times 10^{11}$  molecules in a single Zeeman sublevel of the  $J = 1$  state in  $X$ , which is the starting point of the eEDM experiment. Higher yields are possible with the thermochemical source, which is still under development.

The EDM measurement takes place in the interaction region, which consists of a room temperature vacuum chamber surrounded by five layers of magnetic shielding. Parallel electric  $\mathcal{E}$  and magnetic  $\mathbf{B}$  fields are applied along the  $z$ -axis. The magnetic field is produced by coils mounted around the vacuum chamber inside the magnetic shields. The electric field is produced by glass plates with an indium tin oxide (ITO) coating that are mounted inside the vacuum chamber. All laser beams used in the experiment are sent through the field plates and propagate parallel to the electric field. Sending the laser beams through the electric field plates may not be necessary in the final experiment if we implement the measurement scheme described in Section 7.2.

The molecules produced by the source are in a thermal distribution of rotational states in the electronic ground state  $X$ . On entering the interaction region, the molecules see the optical pumping laser, which is tuned to the  $|X, J = 1\rangle \rightarrow |A, J = 0\rangle$  transition. Spontaneous decay from  $A$  to  $H$  then incoherently populates the  $J = 1$

level of the  $H$  state. The applied electric field is large enough that the  $\Omega$ -doublet levels are completely mixed, and the energy eigenstates can be labeled by  $M$  and  $\mathcal{N} = \hat{\mathbf{n}} \cdot \boldsymbol{\mathcal{E}}$ . To produce the coherent superposition of  $M = \pm 1$  states that is the starting point of the eEDM measurement, a second laser is used. This state preparation laser is tuned to the  $|H, J = 1\rangle \rightarrow |C, J = 1\rangle$  transition and linearly polarized in the  $x - y$  plane. Depending on the polarization, this laser depletes a particular superposition of the  $M = \pm 1$  states, leaving behind a dark state. If the laser is polarized along  $\hat{x}$ , for instance, the dark state is

$$|\psi_{\mathcal{N}}(0)\rangle = \frac{|1, \mathcal{N}\rangle - |-1, \mathcal{N}\rangle}{\sqrt{2}}, \quad (4.8)$$

where we use the state labels  $|M, \mathcal{N}\rangle$ . Since the Stark shift for the  $M = \pm 1$  levels is  $\sim 1$  MHz/V/cm, for  $\mathcal{E} \approx 100$  V/cm, the states with  $\mathcal{N} = \pm 1$  are separated by 200 MHz and can be easily resolved spectroscopically. For the eEDM measurement, we select either  $\mathcal{N} = 1$  or  $\mathcal{N} = -1$  simply by tuning the frequency of the state preparation laser.

After state preparation, the molecular state evolves in the  $\boldsymbol{\mathcal{E}}$  and  $\boldsymbol{B}$  fields while the beam flies through a distance  $L = 22$  cm. For our beam velocity  $v_f \sim 200$  m/s, this corresponds to an evolution time  $\tau \approx 1$  ms. The state after time evolution is

$$|\psi_{\mathcal{N}}(\tau)\rangle = \frac{e^{i\phi}|1, \mathcal{N}\rangle - |-1, \mathcal{N}\rangle}{\sqrt{2}}. \quad (4.9)$$

For a molecule with forward velocity  $v_f$ , the accumulated phase is

$$\phi = \frac{1}{\hbar} \int_{x=0}^{x=L} 2(d_e \mathcal{E}_{eff} + \mu_H B) \frac{dx}{v_f} = \phi_E + \phi_B. \quad (4.10)$$

At the end of the interaction region, the molecules encounter the detection laser, also tuned to the  $|H, J = 1\rangle \rightarrow |C, J = 1\rangle$  transition. Molecules are detected by observing

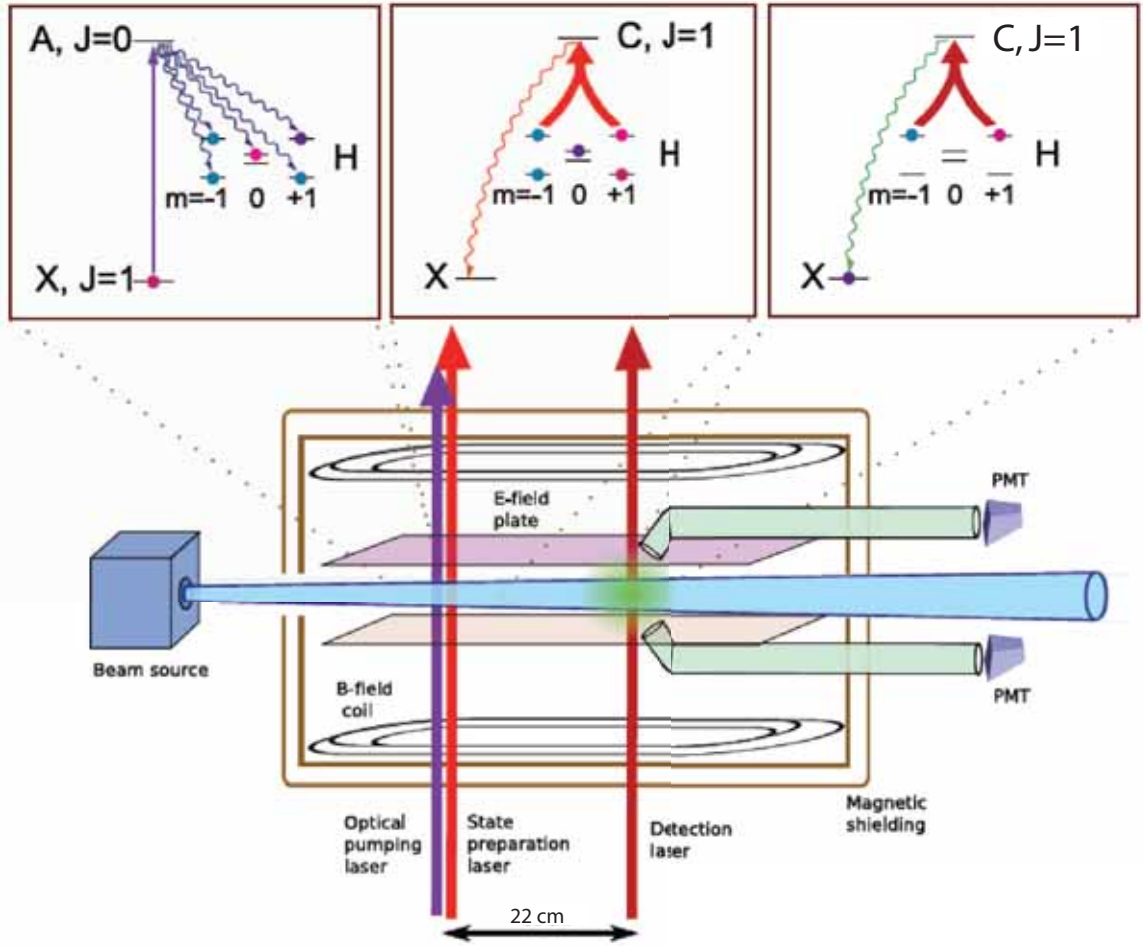


Figure 4.2: Schematic of the ACME experiment. The boxes depict the transitions occurring at each step in the measurement sequence. Full lines indicate transitions driven by a laser, while wavy lines indicate spontaneous decay.

the 690 nm fluorescence photons emitted as they decay from  $C$  back to the ground state  $X$ . We measure the phase  $\phi$  by measuring the population in two quadrature components  $|X_{\mathcal{N}}\rangle$  and  $|Y_{\mathcal{N}}\rangle$  of the final state, where we define

$$\begin{aligned} |X_{\mathcal{N}}\rangle &= \frac{|1, \mathcal{N}\rangle + |-1, \mathcal{N}\rangle}{\sqrt{2}} \\ |Y_{\mathcal{N}}\rangle &= \frac{|1, \mathcal{N}\rangle - |-1, \mathcal{N}\rangle}{\sqrt{2}}. \end{aligned} \quad (4.11)$$

The quadrature state  $|X_{\mathcal{N}}\rangle$  ( $|Y_{\mathcal{N}}\rangle$ ) can be detected by excitation with a laser whose

polarization is  $\epsilon_d = \hat{x}$  ( $\epsilon_d = \hat{y}$ ). The populations in the quadrature states are

$$\begin{aligned} P_X &= N_0 |\langle X_{\mathcal{N}} | \psi_{\mathcal{N}}(\tau) \rangle|^2 = N_0 \left( \frac{1 + \cos \phi}{2} \right) \\ P_Y &= N_0 |\langle Y_{\mathcal{N}} | \psi_{\mathcal{N}}(\tau) \rangle|^2 = N_0 \left( \frac{1 - \cos \phi}{2} \right), \end{aligned} \quad (4.12)$$

where  $N_0$  is the total number of molecules in the beam pulse.

To remove the dependence of the signal on the total number of molecules, which for our source is different for each beam pulse, we will measure the population in both quadratures  $|X_{\mathcal{N}}\rangle$  and  $|Y_{\mathcal{N}}\rangle$  for each pulse of molecules. The sum of the populations  $P_Y + P_X = N_0$  is independent of the precession phase  $\phi$  and is a measure of the total number of molecules in the pulse. The difference  $P_Y - P_X = N_0 \cos \phi$ , depends on both the precession phase and  $N_0$ . To extract only the phase information, we form the asymmetry

$$\mathcal{A} = \frac{P_Y - P_X}{P_Y + P_X} = \cos \phi. \quad (4.13)$$

This asymmetry is the desired eEDM signal.

With the magnetic field adjusted to provide a bias phase  $\phi_B = \pm\pi/2$ , the asymmetry is  $\mathcal{A} = \text{sign}(B) \sin \phi_E = \text{sign}(B) \phi_E$  since  $\phi_E \ll 1$ . From Eqn. 4.10,

$$\mathcal{A} = 2 d_e \mathcal{E}_{eff} \frac{L}{v_f} \text{sign}(B) \text{sign}(\mathcal{E}) \text{sign}(\mathcal{N}). \quad (4.14)$$

In the above we assume that the beam source has a narrow forward velocity distribution so that the offset phase  $\phi_B$  is the same for all the molecules. Since  $\mathcal{A}$  is odd in  $B$ ,  $\mathcal{E}$ , and  $\mathcal{N}$ , it can be isolated by reversing the magnetic field and the electric field and by switching between the states with  $\mathcal{N} = 1$  and  $\mathcal{N} = -1$ .

To measure both quadratures  $|X_{\mathcal{N}}\rangle$  and  $|Y_{\mathcal{N}}\rangle$  for each pulse of molecules from the beam source, we can switch the polarization of the detection laser rapidly between

$\hat{x}$  and  $\hat{y}$  using an electro-optic modulator. For proper normalization, the switching frequency should be much faster than the timescale on which the flux of molecules varies significantly, which leads to a frequency of several hundred kHz for our beam source. This normalization is a crucial component of the eEDM experiment; without it, we cannot combine measurements made on different beam pulses. An alternative technique to normalize the signal for the ACME experiment is described in Section 7.2.

From Eqn. (4.6), the eEDM uncertainty is  $\delta d_e = \hbar v_f / (2\mathcal{E}_{eff} L \sqrt{N_0})$ , where we have used the fact that for a beam experiment,  $\tau = L/v_f$ . For the ACME experiment,  $\tau = 1.1 \text{ ms}^2$ , which gives a shot noise eEDM uncertainty of about  $2.9 \times 10^{-24} e \cdot \text{cm} / \sqrt{N_0}$ . For our expected experimental parameters [41], this leads to a sensitivity of  $2.6 \times 10^{-26} e \cdot \text{cm}$  per molecule pulse using the ablation source assuming the conservative yield of  $10^{10}$  molecules per pulse. With a repetition rate of 10 Hz for the ablation laser, the eEDM uncertainty for a measurement over  $D$  days at 50% duty cycle is  $3.9 \times 10^{-29} e \cdot \text{cm} / \sqrt{D}$ .

---

<sup>2</sup>For the ACME experiment,  $\tau$  is limited by the lifetime of the  $H$  state,  $\tau_H \geq 1.8 \text{ ms}$  [41].

# Chapter 5

## Lasers and locks

Manipulating the state of ThO molecules during the ACME experiment requires lasers at several different wavelengths. Conveniently, all the necessary transitions in ThO are accessible with commercially available laser diodes. We use external cavity diode lasers in the Littrow configuration. The first generation of lasers were home-made, using a design taken from the Greiner group [50] that is similar the one described in [51]. Practical details of the laser construction are discussed in Appendix A. The second generation of lasers were purchased from Toptica and are of the DL Pro design.

The experiment also requires a method of keeping the laser frequencies stable to about 1 MHz over long periods of time and controllably tuning the lasers, for instance to scan over a Doppler profile<sup>1</sup>. Since several lasers are required to prepare and detect the  $H$  state, the stabilization system should be able to handle multiple lasers simultaneously. Also, the system must be sufficiently broadband to handle lasers

---

<sup>1</sup>The width of a Doppler profile for our apparatus can range from about 3 MHz at the end of the interaction region to several hundred MHz a few millimeters from the cell aperture for a 15 K cell.



with wavelengths ranging from 690 nm to 1090 nm. To satisfy these requirements, we stabilize our lasers to a Fabry-Pérot cavity constructed with broadband mirrors and use a LabVIEW program to control the laser frequencies.

## 5.1 Apparatus

We use a confocal Fabry-Pérot cavity with a free spectral range of 750 MHz. The mirrors (Layertec 102965) have a high reflectivity over a broad wavelength range:  $R > 99.8\%$  for 630 - 1100 nm<sup>2</sup>. The cavity design is based on [52]. In this design, the cavity length is variable to allow selection of points of transverse mode degeneracy different from the confocal condition. By adjusting the cavity length appropriately, it is possible to generate transmission peaks separated by  $c/2LN$ , where  $c$  is the speed of light,  $L$  is the cavity length, and  $N > 1$  is an integer ( $N = 2$  for the confocal condition). In practice, we have not found it necessary to reduce the free spectral range using this technique, and we only use the variability of the length to adjust the cavity to the confocal condition. We have successfully used cavities made from Invar. We have also used cavities made from 1018 steel spaced apart with a quartz tube, according to a design from the DeMille group [53]. The latter design is based on cancelation of the thermal expansion of the steel and the quartz, which occurs for a specific choice of the quartz tube length. One of the mirrors in each cavity is mounted on a piezoelectric element (Noliac CMAR03), which allows modulation of

---

<sup>2</sup>Using mirrors of higher reflectivity is unnecessary, as the finesse achieved in practice ( $\mathcal{F} \sim 330$ ) is far below the theoretical finesse based on mirror reflectivity ( $\mathcal{F} = 1569$ ). We initially used mirrors with  $R > 99.9\%$  for 620 - 1120 nm (Layertec 104330). These mirrors have significantly lower transmission ( $T \sim 7 \times 10^{-5}$ ), necessitating the use of an avalanche photodiode to detect the cavity transmission signal. Since the finesse achieved in practice is limited by effects other than mirror reflectivity, there is no advantage to using the higher reflectivity mirrors.

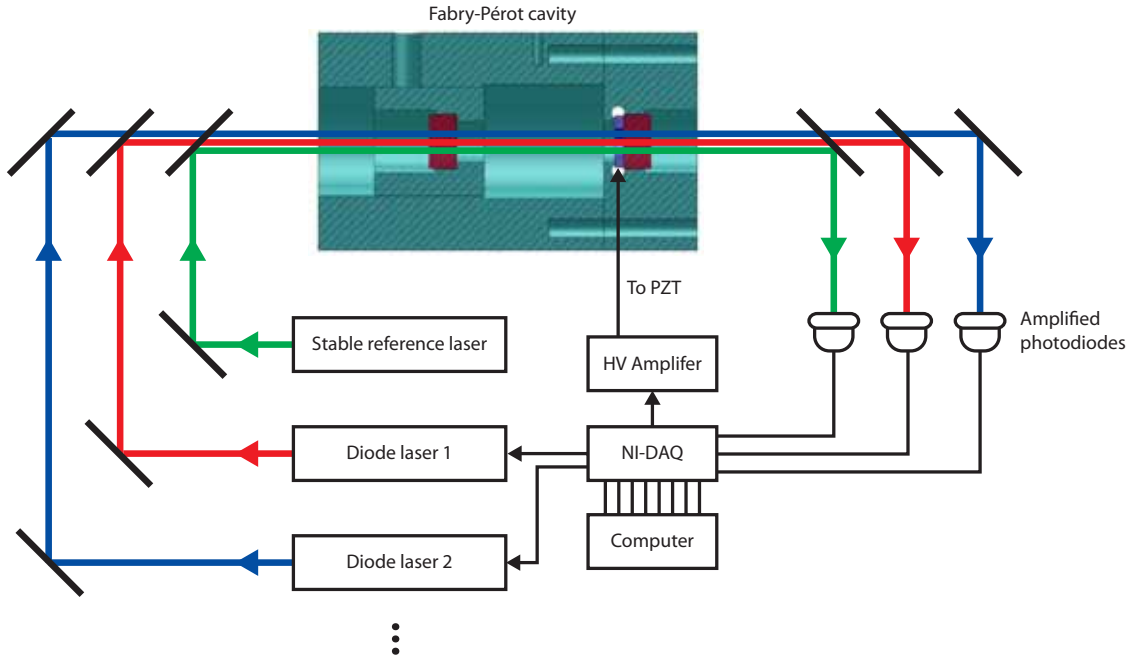


Figure 5.1: Diagram of the setup for laser stabilization.

the cavity length by applying a voltage to the PZT.

Our laser stabilization method is similar to those described in [54, 55, 56]. As shown in Fig. 5.1, we send all the lasers to be stabilized and the stable reference laser into the cavity simultaneously using dichroic beam splitters. We use beam splitters or interference filters to separate the beams at the output for detection. We continuously modulate the length of the cavity by applying a triangle wave to the PZT, while monitoring the transmission of each laser with a separate amplified photodiode (Thorlabs PDA36A). The ramp is provided by a function generator (Stanford Research Systems DS345) and amplified with a high-voltage amplifier before being sent to the PZT. Each time the cavity length is an integer number of half-wavelengths for one of the lasers, there is a peak in the transmission. We simultaneously monitor the voltage ramp applied to the PZT and the cavity transmission signals using a data ac-

quisition board from National Instruments (PCIe-6259). We only collect data during the upward-sloping half of the ramp waveform. During the downward sloping part of the waveform, the computer processes the data and outputs the correction voltages.

After each upward-sloping half-cycle of the ramp waveform, a LabVIEW program finds the position of each transmission peak and determines the corresponding value of the PZT ramp voltage. For each of the controlled lasers, the computer then outputs a correction voltage designed to keep that laser's peak at the same value of the PZT ramp voltage. This correction signal is applied to the laser's piezo element. Correction signals for some lasers are provided by the data acquisition board used to sample the transmission, while outputs for additional lasers are provided by a separate analog output board (National Instruments PCI-6733). The outputs of the two DAQ boards are triggered by a TTL pulse synchronized to the cavity ramp.

To stabilize the average length of the cavity, the LabVIEW program also finds the voltage corresponding to the transmission peak of the stable reference laser. It then outputs a correction voltage that is added to the ramp waveform before it is sent to the cavity PZT. This correction voltage keeps the transmission peak from the stable laser at the same position on the PZT ramp waveform. Any laser with a wavelength within the spectral range of the cavity mirrors can be used as a reference. We have had success using both a commercial stabilized helium-neon laser (Melles Griot 05-STP-901) and a home-made a molecular iodine frequency reference [57].

The beams from all the lasers on the experiment are sent into the cavity using single-mode optical fibers. This ensures that the beams that enter the cavity are Gaussian, regardless of any possible alignment changes of the optics around the laser.

Such changes result in a decrease in power coming out of the fiber, but do not change the shape or direction of the output beam. Although the system is relatively insensitive to changes in the amplitude of the transmission peaks, we use angle-polished (APC) fibers to avoid output power fluctuations that we found to be significant when using physical contact (PC) fibers with flat ends. Alignment of each laser beam into the cavity is done with two mirrors located after the fiber output coupler. This arrangement decouples the lasers and the cavity, allowing us to substitute another laser at the same wavelength by simply switching a fiber, without requiring any change in the optics that couple the beam into the cavity.

### 5.1.1 LabVIEW program

The program has two operating modes: scope and lock. In scope mode, the program simply displays the cavity spectra for all the lasers, allowing the user to verify that the lasers are single-mode<sup>3</sup> and ensure that none of the laser peaks are located too close to the edge of the cavity ramp waveform by adjusting the offset and amplitude of the ramp produced by the function generator. In lock mode, the program keeps track of the center of each laser's transmission peak. It does not attempt to lock any laser until the user presses the 'Lock' button for that particular laser. When the lock is turned on for a given laser, the program outputs a correction voltage to keep that laser's transmission peak fixed at a constant value of the cavity ramp voltage. The proportional (P), integral (I), and derivative (D) gains for each laser and for the cavity feedback are independently adjustable. In practice, we find it unnecessary to

---

<sup>3</sup>Single-mode operation is characterized by the presence of a single peak in the cavity transmission spectrum. The presence of multiple peaks or an absence of peaks indicates multi-mode operation.

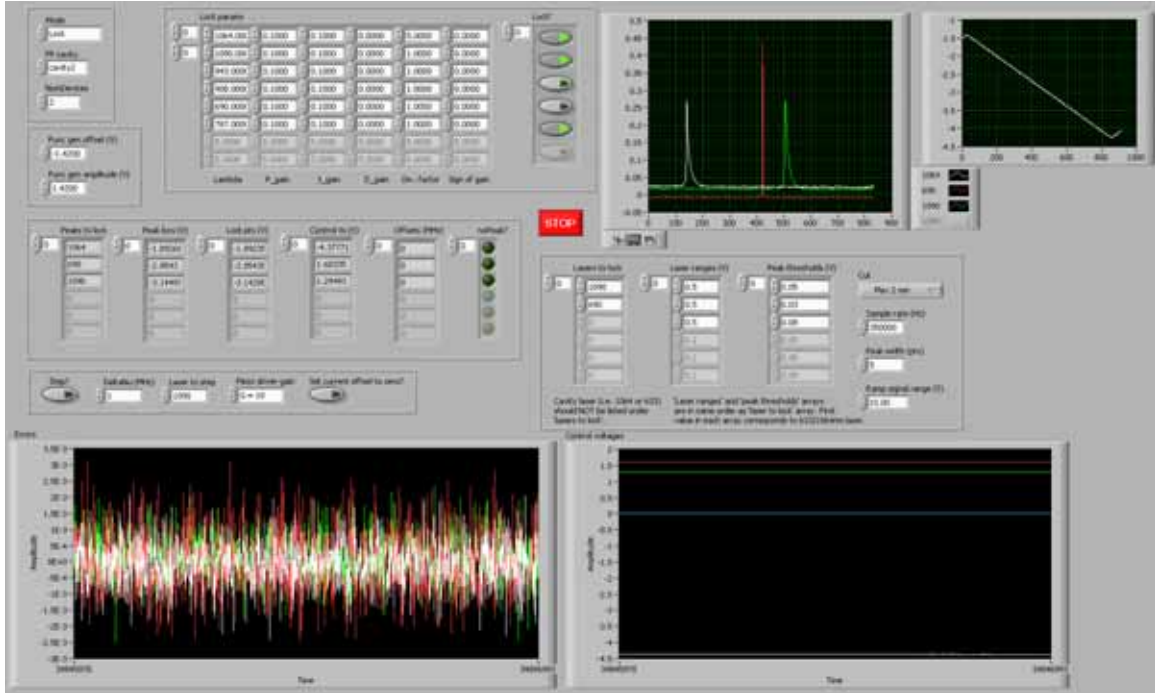


Figure 5.2: Front panel of the LabVIEW program used for laser stabilization.

use the derivative gain. The locks for the different lasers are completely independent. This allows the user to tune one laser, lock it, then tune the next laser, lock it, etc.

In lock mode, the laser frequency can be adjusted by changing the lock point. For ease of use, the user enters the desired frequency change in megahertz and the program converts that to the necessary change in the lock point, which is set in terms of cavity ramp voltage. This conversion is done using measured voltage to frequency conversions for each laser and each cavity. To measure a voltage to frequency conversion for a particular laser, we modulate the laser current to imprint sidebands with a known frequency separation (typically 100 MHz) on the laser output. This frequency modulation can also be done using an electro-optic modulator. We send the frequency-modulated laser through the cavity and simultaneously record cavity transmission and ramp voltage. We then fit the peaks and determine the voltage

interval between the centers of the sidebands, which gives the voltage to frequency conversion since the frequency separation of the sidebands is known. Due to PZT nonlinearity, the voltage to frequency conversion depends on the cavity offset voltage. This dependence can be measured and taken into account if greater accuracy in adjusting the frequency is necessary.

## 5.2 Performance

The cavity ramp frequency and hence the lock loop bandwidth is typically 211 Hz. The sample rate on the DAQ board is about 300-400 kHz. The sampling rate must be fast enough that there are five or more sample points on each transmission peak to allow an accurate determination of the peak center<sup>4</sup>. To minimize electronic noise from the data acquisition boards, the correction signals are low-pass filtered at 1 kHz.

This laser locking system has been used for all the ThO experiments done at Harvard to date. We use two such systems with two different cavities, one located in the room where the experiment takes place (LISE G14) and one located in a different building (Jefferson 162). Light from lasers located in Jefferson 162 is transported to the experiment via 100 meter long optical fibers. Each locking system has 12 outputs, making it possible in principle for 11 lasers to be locked to each cavity<sup>5</sup>. The largest number of lasers we have simultaneously locked to one cavity is four. There is nothing fundamental about this number either; it is simply the largest number of

---

<sup>4</sup>Since we scan over the entire 750 MHz free spectral range in half of the period of the ramp waveform, and the typical width of a peak is  $\sim 5$  MHz, requiring five or more points on the peak leads to a sample rate  $R_{sample} \geq 317$  kHz.

<sup>5</sup>There is nothing fundamental about this number. More outputs can be added if necessary by installing an additional analog output board.

lasers we have ever needed to use simultaneously in an experiment. The lasers can stay locked for days at a time. Some typical error data from the laser lock is shown in Fig. 5.3. Converting the error signal from the laser lock to frequency using the measured voltage to frequency conversion yields a root-mean-square stability of about 1.4 MHz. This is in agreement with measurements of the long-term ( $\sim 10$  seconds) linewidth obtained by beating together two lasers at the same frequency using the method described in [57].

### 5.3 Limitations

The main disadvantage of the laser stabilization scheme discussed here is that it is too slow to eliminate acoustic noise. The locking bandwidth cannot exceed the frequency of the cavity PZT ramp, which is limited by the frequency response of the PZT. For most piezoelectric elements, this limits the ramp frequency to less than a few kilohertz. Thus, a system fast enough to eliminate acoustic noise will need to eliminate the cavity modulation. This is possible by modulating the laser frequency to derive an error signal, for instance using the Pound-Drever-Hall method [58, 59].

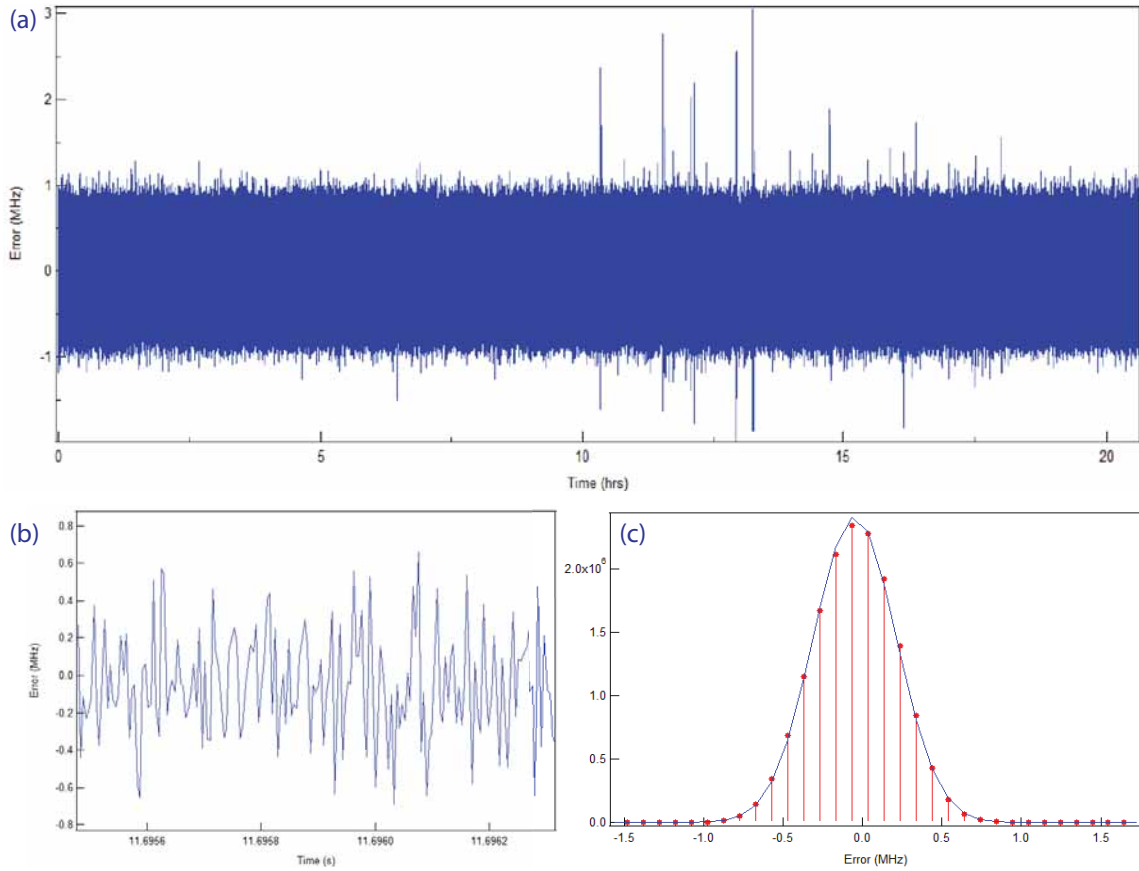


Figure 5.3: **(a)** Typical error signal from the laser lock, which has been converted to frequency using the measured voltage to frequency conversion. The root-mean-square of the above data is  $\sim 1.4$  MHz, which is consistent with the laser linewidth over long times ( $\sim 10$  seconds) measured by beating together two separate lasers locked to separate cavities. **(b)** Zoomed in plot of the signal from part (a). **(c)** A Gaussian fit to a histogram of the error signal yields a center consistent with zero and a FWHM of 0.43 MHz. This indicates that the lock successfully removes long-term drift of the laser frequency.



# Chapter 6

## An alternative $g$ -factor measurement

Recently our collaboration obtained a value for the  $g$ -factor of the  $H$  state by measuring the Zeeman splitting of the  $H \rightarrow E$  transition in a large magnetic field [36]. Since that experiment used permanent magnets, the magnetic field could not be varied to investigate possible systematic errors in the measurement. Thus, we wanted to confirm this important result using a complementary measurement technique that is susceptible to different systematic errors. This chapter describes a measurement of the  $H$  state  $g$ -factor made by observing angular momentum precession in a magnetic field.

### 6.1 Apparatus

This measurement was done using the beam source and interaction region described in Chapter 4. For this experiment, the ThO molecules were not produced by laser ablation but through a thermochemical process [49]. Thermochemical produc-

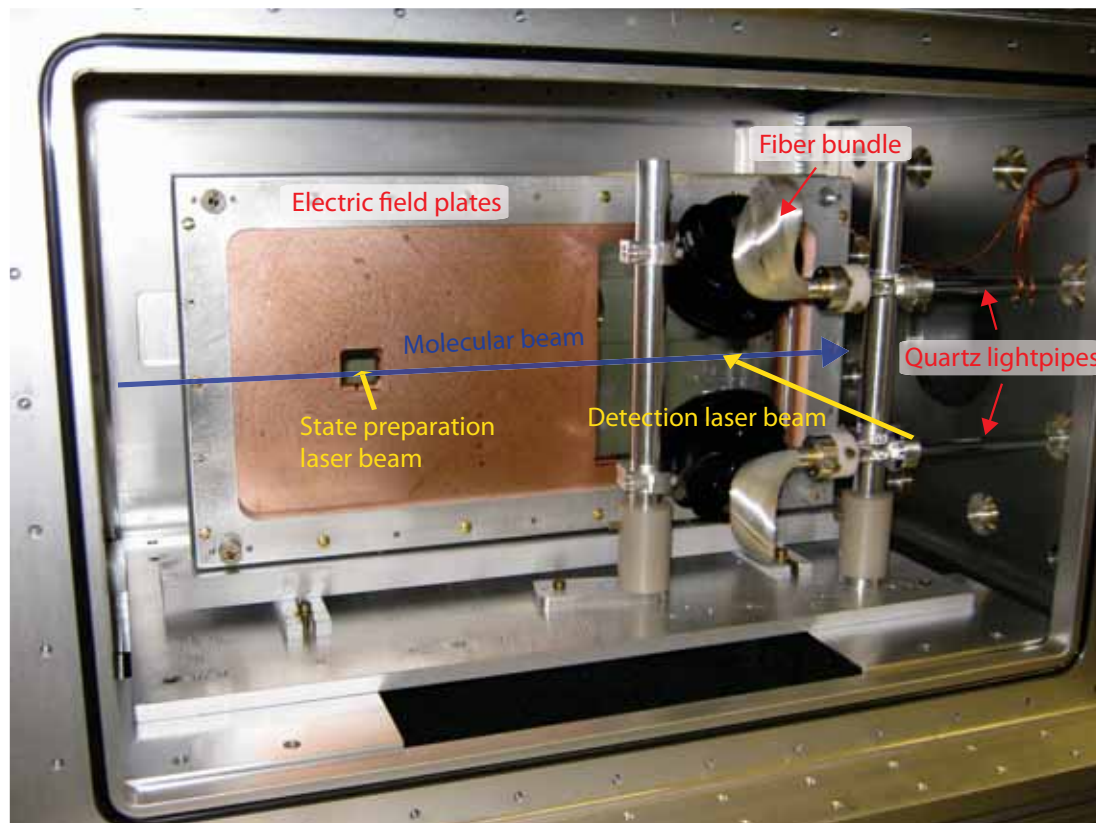


Figure 6.1: Inside of the interaction region vacuum chamber. The ThO beam propagates from left to right. The windows in the electric field plates are for state preparation (small window on the left) and detection (large window on the right).

tion is possible because the reaction  $\text{Th(s)} + \text{ThO}_2\text{(s)} \rightarrow 2\text{ThO(g)}$  is strongly favored at high temperatures (around 2000 K). ThO is produced by locally heating a pressed target of mixed  $\text{ThO}_2$  (75%) and Th (25%) powder using the focused beam from a 50 W fiber laser (IPG Photonics YLR-50). Thermochemical production typically results in peak signals about three times as large as the peak signals from ablation. The real advantage of this technique, however, is the much longer duration of the molecule pulses. While a molecule pulse from ablation lasts a few milliseconds in the detection region, pulses produced by the thermochemical process can be hundreds of

milliseconds long. The molecule pulse duration is controlled by varying the duration of the fiber laser pulse. For the data discussed below, the fiber laser pulses were 2.5 ms long, with a repetition rate of about 7 Hz. The repetition rate and pulse duration are adjusted to keep the temperature of the buffer gas cell at around 15 K. Neon was used as the buffer gas for all the data described here, with a typical buffer gas flow rate of 20 - 30 sccm [48].

Fig. 6.1 shows the inside of the interaction region vacuum chamber. The electric field plates currently in place are made of copper with pieces of ITO-coated float glass (Delta Technologies CH-50IN-1509) attached to allow laser access in the state preparation and detection regions. The field plate spacing is 2 cm. Applying an electric field reduces the detected fluorescence signal by a factor of two due to parity mixing of the  $H$  state levels. Since the pulsed excitation technique we use also reduces the signal due to not sampling all the molecules in the beam, we do not apply an electric field during the  $g$ -factor measurement in order to keep the signal as large as possible.

The magnetic field is produced by the coil that will be used for the final experiment. To achieve good field uniformity, we use both the main coil and the two side coils located at each end of the cylindrical main coil (see Fig. 6.2). The side coils prevent the field from decreasing near the edges of the main coil. The current in both side coils should be 4.4 times the current in the main coil. With this arrangement, the magnetic field in milligauss is given by  $B = 1.37 \times I_{main}$ , where  $I_{main}$  is the current in the main coil in milliamps. The current for the main coils is provided by precision current supplies (Krohn-Hite Model 521 and 522). The side coil current is provided

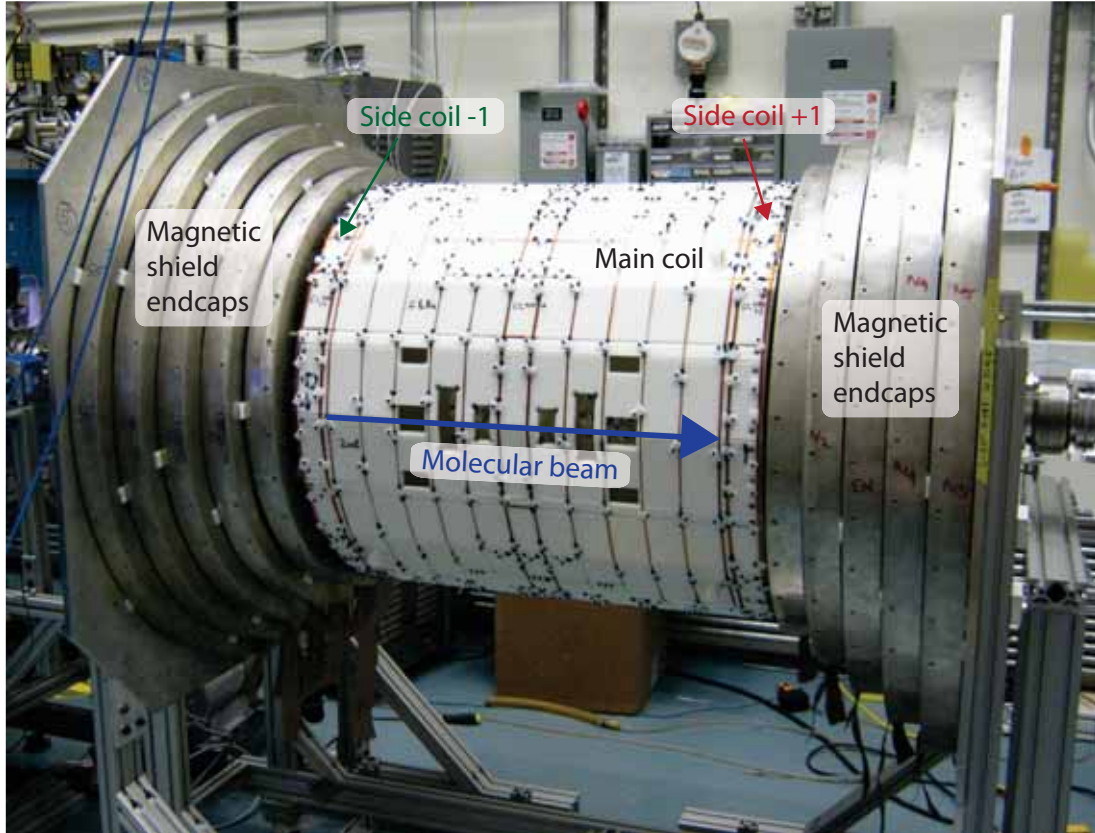


Figure 6.2: Magnetic field coils. The side coils on each end, labeled +1 and -1, maintain field uniformity at the edges of the cylindrical main coil. The endcaps of the magnetic shields can be seen on either side of the apparatus.

by an Agilent 6654A supply. For this data, the interaction region is surrounded by three layers of magnetic shields.

The  $H$  state is populated by exciting molecules to the  $A$  state with a 943 nm laser, which leads to incoherent population of all Zeeman sublevels of the  $J = 1$  level in the  $H$  state. The 943 nm light is derived from a diode laser amplified with a tapered amplifier (Toptica BoostA), so that the power incident on the apparatus is about 120 - 150 mW. The 943 nm laser is followed by a horizontally polarized 1090 nm laser, which excites molecules out of the  $M = \pm 1$  sublevels of the  $H$  state, leaving a dark

state as described in Chapter 7.

The state is read out in the detection region, separated from the state preparation region by 22 cm. The detection light is derived from the same 1090 nm diode laser as the state preparation light. The light is split and fed to two separate polarization maintaining fiber amplifiers (Keopsys KPS-BT2-YFA-1083-SLM-PM-05-FA). The polarization of the detection beam is parallel to that of the state preparation beam. The power of the state preparation beam is about 300 mW, while that of the detection beam is about 70-80 mW. It is helpful to have as much power in the state preparation beam as possible to ensure that all the molecules in the beam are prepared in the appropriate state.

Detection of the fluorescence is accomplished with collection lenses located on either side of the electric field plates, as shown in Fig. 6.1. The light is collimated by a large (3" diameter) lens and focused by a second lens onto the input of a multi-mode fiber bundle. The output of the fiber bundle is optically contacted to a quartz light-pipe that takes the light out of the vacuum chamber. Fluorescence is detected using a photomultiplier tube (Hamamatsu R8900U-20) amplified with a current preamplifier (Stanford Research Systems SR570). Although there will be eight collection lenses surrounding the detection region in the final experiment, the data presented here was taken using only one collection lens.

Since the state preparation beam is not sufficiently powerful to pump out molecules in all velocity classes, a high degree of parallelism between the state preparation and detection beams is crucial to ensure that they address the same velocity class of molecules. This alignment is accomplished by monitoring the depletion of the signal

in zero magnetic field. Since the state preparation and detection polarizations are parallel, the signal in the detection region should disappear when the state preparation beam is turned on since that beam pumps out the same superposition of  $M = \pm 1$  that is addressed by the detection laser. We achieve parallelism of the beams by monitoring the depletion and adjusting the angle of the state preparation beam in small increments. Maximal depletion will occur when the beams are parallel. In practice, the best we have observed is a reduction of the signal by factor of 2 - 3 as result of turning on the state preparation beam. An alternative to changing the beam alignment is to controllably detune one of the beams relative to the other, for instance using an acousto-optic modulator (AOM).

## 6.2 Measurement technique

The procedure for measuring the  $g$ -factor is as follows. We first populate the  $H$  state and prepare the coherent superposition of  $M = \pm 1$ . This superposition corresponds to a state with its angular momentum in the  $x-y$  plane. For concreteness, let's assume that it is initially prepared to lie along  $\hat{x}$  (i.e. the state preparation laser is polarized along  $\hat{y}$ ). An applied magnetic field  $\mathbf{B} = B \hat{z}$  causes the angular momentum to precess. After a precession time  $\tau$ , which corresponds to the time a molecule takes to fly between the state preparation and detection regions, we read out the precession angle  $\phi$  by probing the molecules with a laser identical to the state preparation laser. The resulting signal is proportional to the component of the angular momentum along  $\hat{y}$ , which will be zero in the absence of precession ( $B = 0$ ) and maximal when  $B$  is large enough to make the angular momentum precess by  $\pi/2$ . The population transferred

to the excited state (and hence the observed fluorescence intensity) is proportional to  $\sin(\mu_H B \tau)$ , where  $\mu_H = g\mu_B$  is the magnetic moment of the  $H$  state. This sinusoidal pattern of signal as a function of magnetic field is called a Ramsey fringe.

We can measure the  $H$  state  $g$ -factor by observing a Ramsey fringe and fitting it to  $\sin(g\mu_B B \tau)$ . However, the precision of this measurement will be limited by the velocity spread of the ThO beam. For a molecule with forward velocity  $v_f$ , the time  $\tau$  appearing in the expression for the precession angle  $\phi$  is  $\tau = L/v_f$ , where  $L = 22.25$  cm is the distance between the state preparation and detection beams. The molecular beam with neon buffer gas has a forward velocity spread of around 30 m/s [48], which would result in a fractional uncertainty  $\delta g/g = 16\%$  for an average velocity of 180 m/s. Making a measurement with smaller uncertainty requires selecting a particular velocity group of molecules, which we do using a pulsed excitation technique.

The 943 nm beam that populates the  $H$  state is sent through an AOM (Isomet 1205-C) and the diffracted beam is sent into the apparatus. To switch the 943 nm beam rapidly on and off, the RF signal that drives the AOM is sent through a switch (Mini-Circuits ZYSWA-2-50DRB). A pulse generator (Stanford Research Systems DG645) triggered off the TTL pulse that fires the fiber laser generates a burst of 100  $\mu$ s wide pulses with a variable delay and spacing. These pulses control the switching of the RF signal, such that the 943 nm beam is only on during each 100  $\mu$ s pulse. The delay of the burst is adjusted to maximize the signal amplitude, while the spacing between the pulses is adjusted to ensure that the successive pulses do not overlap in the detected signal. A typical signal with pulsed excitation is shown in

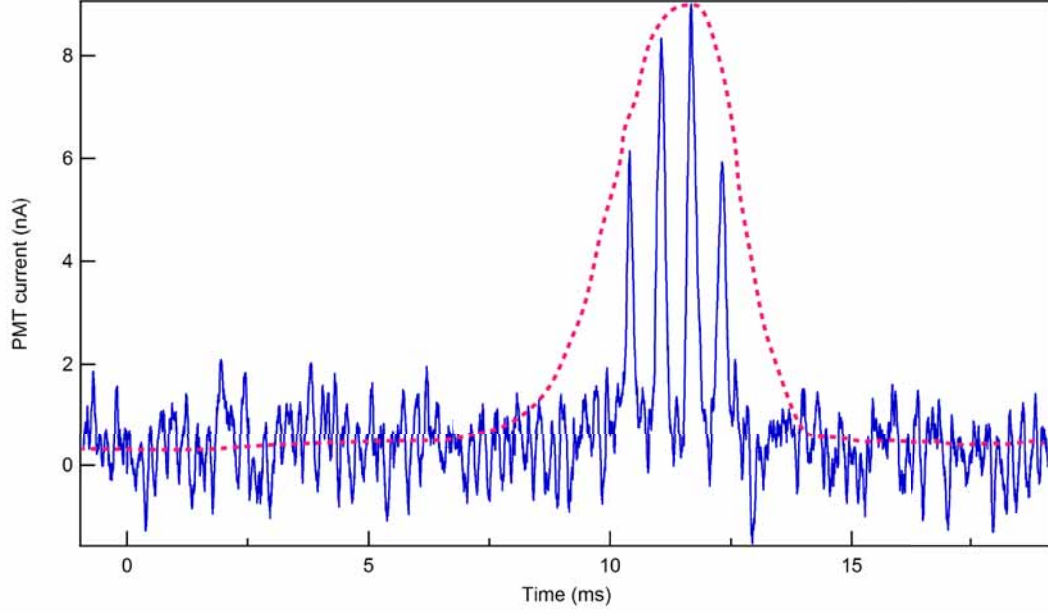


Figure 6.3: Typical fluorescence signal seen with pulsed 943 nm excitation. Each fluorescence peak corresponds to one of the 943 nm excitation pulses; in this case, there were four excitation pulses in total. The fiber laser that produces the ThO molecules turns on at  $t = 0$  and remains on for 2.5 ms. The pink dashed line indicates the molecule pulse envelope. This trace is an average of 64 fiber laser shots.

Fig. 6.3. The state preparation and detection lasers are on continuously.

To determine the  $g$ -factor, we measure a Ramsey fringe using the pulsed excitation technique. Since each pulse in the detected fluorescence corresponds to one of the excitation pulses, which occur at known times, the time interval between the excitation pulse and the detected pulse is the precession time  $\tau$  for that group of molecules<sup>1</sup>.

We can obtain better velocity resolution by dividing each detected pulse into several

<sup>1</sup>Since the beam that is pulsed is the optical pumping beam but spin precession begins only after the molecules have passed through the state preparation beam, this is not exactly true. The real value of  $\tau$  is the value  $\tau'$  determined by the above method corrected to account for the time it takes the molecules to fly between the optical pumping and state preparation beams. Since the distance between these beams is  $d_{ps} = 2$  mm, while the distance between the optical pumping and detection beams is  $L = 22.45$  cm, the real value of  $\tau$  is  $\tau = (1 - d_{ps}/L) = 0.99 \tau'$ . In practice, this correction is negligible given our uncertainty.



time bins, so that the uncertainty in  $\tau$  is just half the width of a time bin.

Due to large variations in the molecular beam yield from one fiber laser shot to the next, the signal must be normalized. We obtain a measure of the beam yield by monitoring the absorption of a 690 nm laser sent through the molecular beam about 1 mm in front of the aperture of the buffer gas cell. To normalize the signal, we divide the integral of the detected fluorescence signal by the peak fractional absorption of the 690 nm laser. We find that using the peak fractional absorption as opposed to the absorption integrated over the entire molecule pulse provides a better normalization, probably because the pulsed technique only samples a small fraction of the beam, which is adjusted to coincide closely with the peak to maximize the signal. Although normalizing to the 690 nm absorption reduces the scatter in the data, this technique is imperfect since it involves measuring the number of molecules in the ground state about 1.6 m before the detection region. A better normalization technique would involve measuring the population in the  $H$  state directly in the detection region. This can be done using one of the methods under development for the main eEDM experiment - polarization switching or switching between the  $C$  state  $\Omega$ -doublet levels.

### 6.3 Results

Fig. 6.4 shows an example of a measured Ramsey fringe. We fit this data to the form  $s(x) = s_0 + A \sin(\beta x + \theta)$ , where the fit parameter  $\beta$  is related to the  $g$ -factor by  $g = \hbar \beta / \mu_B$ . The scatter in the data is almost certainly due to the imperfect normalization provided by the 690 nm absorption signal, which is corroborated by the observation that the scatter increases for data taken using longer fiber laser pulses.

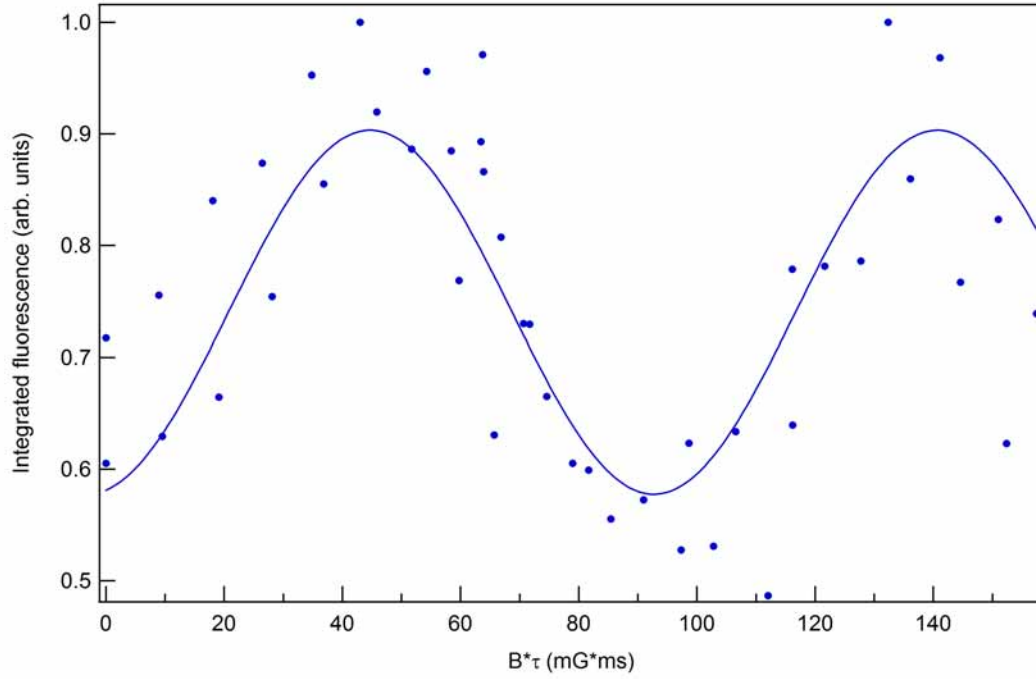


Figure 6.4: Measured Ramsey fringe. Each point is an integral over one of the detected pulses like those shown in Fig. 6.3. The solid line is a fit to the form  $s(x) = s_0 + A \sin(\beta x + \theta)$ , where  $x = B\tau$ . This data was taken on 08/15/11.

Obtaining an accurate  $g$ -factor measurement requires knowledge of the magnetic field over the path of the ThO beam. The field produced by both the main coil and the side coils as a function of distance from the center of the coils has been measured directly in this apparatus. The measurements were done using a fluxgate magnetometer (Bartington Instruments Mag-03MS100) which has an uncertainty of  $\delta B/B = 5 \times 10^{-3}$ . The magnetic field was measured for two different current configurations: one with the main coil at 10 mA and the side coils at 44 mA and one with the main coil at 10 mA and the side coils off. The field from just the side coils is then simply the difference between these two measurements. Fig. 6.5 shows the measured magnetic field values.

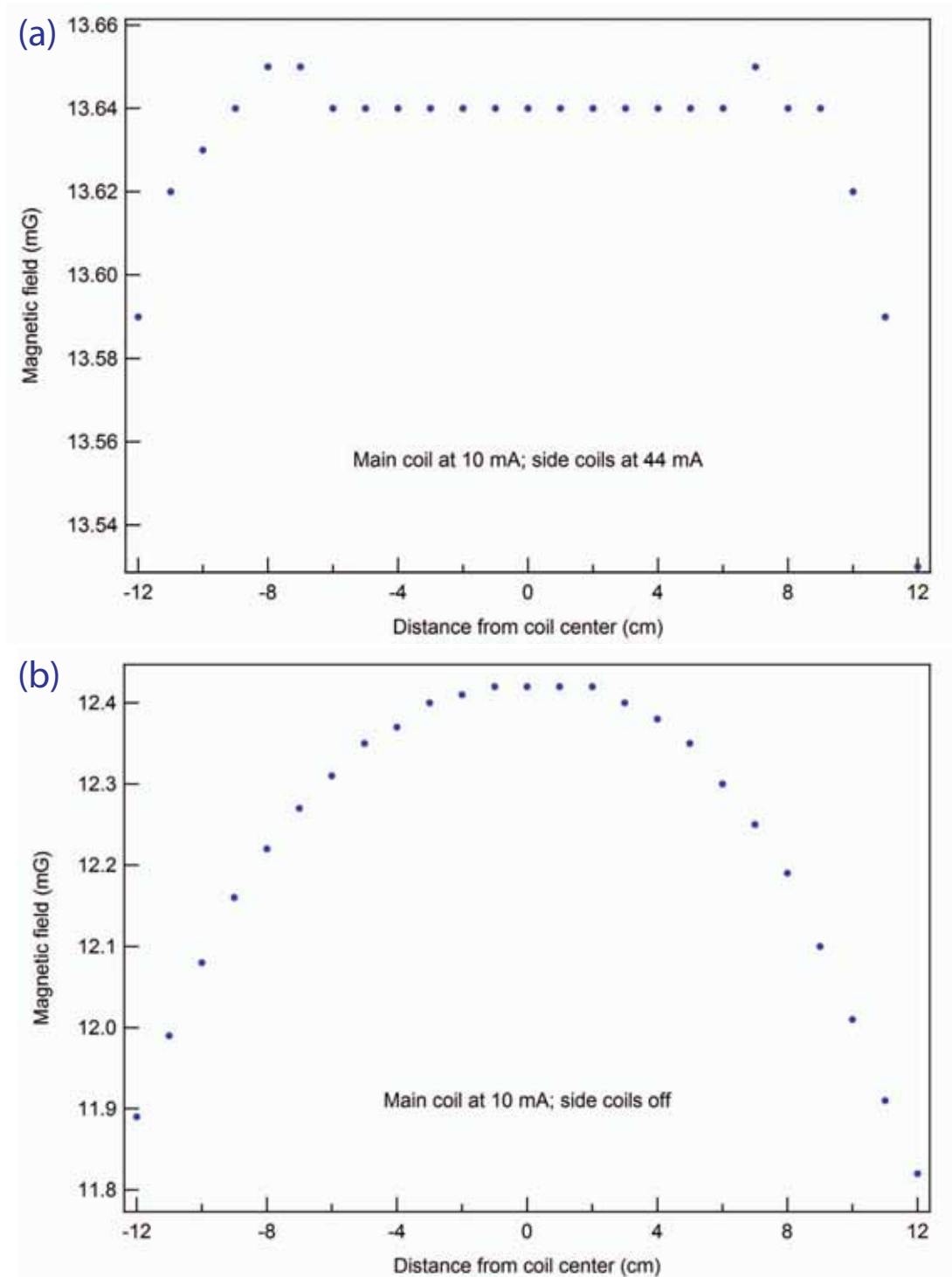


Figure 6.5: Measured magnetic field as a function of distance from the center of the coils. Displacements from the center are positive if they are in the downstream direction. (a) Main coil at 10 mA and side coils at 44 mA. (b) Main coil at 10 mA and side coils off.

To calculate the magnetic field at a particular value  $I_{main}$  of the main coil current in mA, we use the formula

$$B(I_{main}) = \frac{I_{main}}{10} B_{main} + \frac{a}{44} B_{side}, \quad (6.1)$$

where  $B_{main}$  is the measured field from the main coil at 10 mA and  $B_{side}$  is the measured field from the side coils at 44 mA. This equation assumes that the relationship between magnetic field and current is linear. We have verified that this relationship remains linear up to the highest currents used in our experiment<sup>2</sup>. For maximum field uniformity, the current in the side coils should be 4.4 times the current in the main coil. Due to an incorrectly set voltage limit, the current in the side coils could not go above 48 mA during this experiment. This is accounted for by the parameter  $a$  above, which takes the following values:  $a = 22$  for  $I_{main} = 5$  mA,  $a = 44$  for  $I_{main} = 10$  mA, and  $a = 48$  for all other values of  $I_{main}$ .

For a field that is not constant over the precession time, the expression for the precession angle  $\phi$  is

$$\phi = \frac{g\mu_B}{\hbar} \int_0^\tau B(t) dt = \frac{g\mu_B}{\hbar} \int_0^L \frac{B(x)}{v_f} dx = \frac{g\mu_B}{\hbar} \frac{\tau}{L} \int_0^L B(x) dx, \quad (6.2)$$

since  $v_f = L/\tau$  is the forward velocity of the ThO beam. To measure the  $g$ -factor, we need to calculate the integral  $\mathcal{B} = \int_0^L B(x) dx$ . We do this by first calculating the integrals  $\mathcal{B}_{main} = \int_0^L B_{main}(x) dx$  and  $\mathcal{B}_{side} = \int_0^L B_{side}(x) dx$  and then using Eqn. (6.1) to find  $\mathcal{B}$  for each value of the main coil current.

Since the magnetic field was not uniform throughout the region, the integrals depend on the exact locations of the state preparation and detection beams relative

---

<sup>2</sup>This indicates that no magnetization of the mu-metal shields occurs as a result of applying the magnetic field.

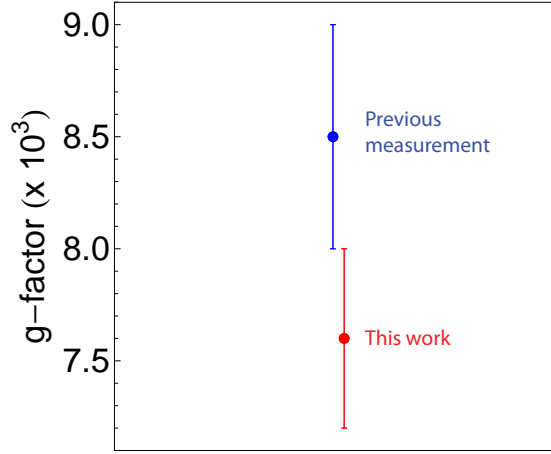


Figure 6.6: Comparison of current  $g$ -factor measurement with the previous measurement by our collaboration.

to the center of the coils. We determine these locations as follows. The beams are sent through 2.4 cm wide holes in the mu-metal shields, and each beam was centered by eye on the corresponding hole. For the detection beam, which was never moved, we estimate the uncertainty in its position as  $\pm 3$  mm. The state preparation beam location is not known as precisely. As discussed above, this is the beam that was tweaked to maximize the depletion. We thus conservatively estimate the uncertainty as one quarter of the width of the hole or  $\pm 6.35$  mm. The uncertainty in the location of the precession region due to uncertainties in both beam positions is thus  $\pm 7$  mm.

We calculate the central value of  $\mathcal{B}$  by assuming that the state preparation and detection beams are sent through the centers of the holes in the mu-metal shields, so the precession region extends from -11 cm to +11 cm. We find  $\mathcal{B}_{main} = 270.18 \pm 0.28$  and  $\mathcal{B}_{side} = 29.865 \pm 0.031$ . The error bars quoted above are due to the magnetometer uncertainty. There is another source of error due to the uncertainty in the locations of the state preparation and detection beams. We estimate this as half the difference

in the values of  $\mathcal{B}$  obtained by displacing the precession region by  $\pm 7$  mm<sup>3</sup>. This gives  $\delta\mathcal{B}_{main} = 0.054$  and  $\delta\mathcal{B}_{side} = 0.032$ . Combining these uncertainties gives  $\delta\mathcal{B}_{main} = 0.29$  and  $\delta\mathcal{B}_{side} = 0.045$ . Estimating the uncertainty in the length  $L = 22$  cm of the precession region as 3 mm, we find  $\delta L/L = 0.014$ . The total uncertainty in  $\phi$  due to uncertainties in  $\mathcal{B}$  and  $L$  is then  $\delta(\mathcal{B}/L)/(\mathcal{B}/L) = 0.027^4$ .

Uncertainties in the fit parameter  $\beta$  and the precession time  $\tau$  also contribute to the uncertainty of the measured  $g$ -factor. The signal from each excitation pulse lasts  $T_{pulse}$  ms at the detection region<sup>5</sup>. Dividing each detected fluorescence pulse into  $n$  time bins reduces the uncertainty in  $\tau$ , but increases the scatter of the points since fewer data points are integrated for each point on the Ramsey fringe. We take the uncertainty to be half the width of a time bin, so for  $n$  time bins  $\delta\tau = T_{pulse}/(2n)$  ms. As the number of bins increases, the uncertainty in  $\tau$  decreases, while the uncertainty in  $\beta$  either stays the same or increases due to the increased scatter in the data. The optimum number of bins is taken to be the one where the fractional uncertainty in  $\tau$  becomes smaller than the uncertainty in  $\beta$ . The  $g$ -factor values obtained from the fit do not depend on the number of bins. For comparison, Table 6.1 lists the results from the 08/15/11 data as a function of the number of bins. The error in the  $g$ -value is determined by combining the errors in  $\tau$ ,  $\beta$ , and the magnetic field in quadrature

$$\frac{\delta g}{g} = \sqrt{\left(\frac{\delta\beta}{\beta}\right)^2 + \left(\frac{\delta\tau}{\tau}\right)^2 + 0.027^2}. \quad (6.3)$$

<sup>3</sup>The two values of  $\mathcal{B}$  are calculated by having the precession region extend from -11.7 cm to +10.3 cm and from -10.3 cm to +11.7 cm.

<sup>4</sup>The fractional uncertainty  $\delta\mathcal{B}/\mathcal{B}$  differs slightly for different values of  $\mathcal{B}$ . It ranges from 0.0236 to 0.0247. We use the larger value in the above calculation.

<sup>5</sup> $T_{pulse}$  differs slightly from one data run to the next and is also longer for the thermochemical source than the ablation source. To account for this, we determine  $T_{pulse}$  individually for each data set. See Table 6.2 for the  $T_{pulse}$  values.

# of bins	$g$ -factor ( $\times 10^3$ )	$\delta\tau/\tau$	$\delta\beta/\beta$
1	$7.4 \pm 1.4$	0.180	0.044
2	$7.3 \pm 0.8$	0.090	0.053
3	$7.5 \pm 0.6$	0.060	0.049
4	$7.4 \pm 0.5$	0.045	0.046
5	$7.6 \pm 0.5$	0.036	0.043

Table 6.1: Best-fit values of the  $g$ -factor obtained from the data set taken on 08/15/11 by dividing the data into the indicated number of bins. The error is calculated using Eqn. (6.3) using the listed fractional errors in  $\tau$  and  $\beta$ .

Four data sets were used for the measurement, which were taken on 08/06/11 (ablation source), 08/15/11 (thermochemical source with 2.5 ms long fiber laser pulses), 08/16/11 (ablation source), and 08/20/11 (thermochemical source with 10 ms long fiber laser pulses). As expected, the best-fit phase for all data except the set from 08/06/11 is such that the fringe has a minimum at zero magnetic field. Due to the phase offset, the 08/06/11 data is not used for the final  $g$ -factor determination<sup>6</sup>.

Combining all data except that from 08/06/11 gives  $g = (7.6 \pm 0.4) \times 10^{-3}$ . This result is in agreement with the previous determination,  $g = (8.5 \pm 0.5) \times 10^{-3}$  [36]. A comparison of the two values is shown in Fig. 6.6. The agreement between two results obtained using measurement techniques that are susceptible to very different systematic errors gives us confidence in our determination of the  $H$  state  $g$ -factor. The small  $g$ -factor is one of the main advantages of ThO over other molecules currently being used for eEDM measurements. For instance, our experiment is about 90 times

<sup>6</sup>There is something strange about this data because the phase of the Ramsey fringe is different for the points taken while increasing the coil current in increments and those taken while turning the current back down. This could be explained by magnetization of the mu-metal shields. However, the linearity of the measured magnetic field with current in the coils suggests that there is no magnetization of the shields even at the highest magnetic fields used in this experiment. To avoid any possible magnetization, the shields were degaussed after application of the highest magnetic field value for all data sets except 08/06/11. Including the 08/06/11 data, which gives a value of the  $g$ -factor in agreement with all the other data, does not change the final result.

Date	$g$ -factor ( $\times 10^3$ )	$T_{pulse}$ (ms)	Optimal # of bins
08/06/11	$7.1 \pm 0.8$	0.236	2
08/15/11	$7.6 \pm 0.5$	0.397	5
08/16/11	$6.7 \pm 1.2$	0.210	1
08/20/11	$8.0 \pm 0.7$	0.463	4

Table 6.2: Best-fit values of the  $g$ -factor obtained from all data sets.

less sensitive to magnetic fields than the PbO eEDM experiment, since the  $a(1)$  state of PbO has a  $g$ -factor of about 0.9 [60].



# Chapter 7

## State preparation

The most straightforward way to prepare the initial state for the ACME experiment, a coherent superposition of the  $M = +1$  and  $M = -1$  sublevels within the  $J = 1$  level of the  $H$  state, takes two steps. The first step is incoherent population of the  $H$  state by means of optical pumping via the  $A$  state. The second step - termed state preparation - produces the coherent superposition and is the focus of this chapter.

State preparation is done using a laser that excites molecules out of the  $H$  state. The coherent superposition of  $M = \pm 1$  that remains after the molecules have passed through the state preparation laser is the one that does not couple to the laser, i.e. it is a dark state. In order to have a dark state, the state preparation laser must couple both the  $M = +1$  and  $M = -1$  sublevels of the  $H$  state to a single Zeeman sublevel of the upper state but with excitation amplitudes that cancel. For instance, if the state preparation laser is polarized along  $\hat{x}$ , the dark state is

$$|d_x\rangle = \frac{|M = +1\rangle - |M = -1\rangle}{\sqrt{2}}. \quad (7.1)$$

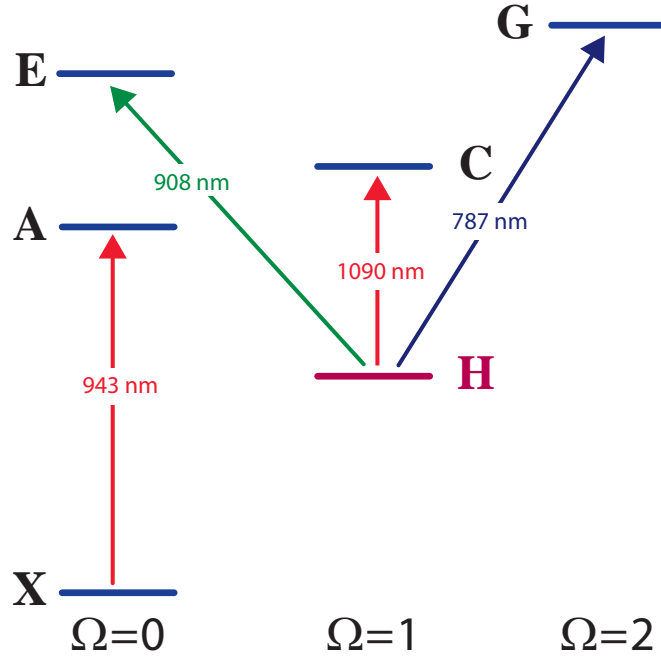


Figure 7.1: Electronic states of ThO relevant for the state preparation schemes discussed here. All states in a given column have the  $\Omega$  value indicated at the bottom.

Since the initial  $H$  state has  $J'' = 1$  and we are using an E1 transition, the final state of the state preparation transition can have  $J' = 0, 1$ , or  $2^1$ . For  $J' = 0$  or  $1$ , a linearly polarized state preparation laser with its polarization vector in the  $x-y$  plane couples the  $M = \pm 1$  sublevels of the  $H$  state only to the  $M = 0$  sublevel of the upper state. In this case, there is always a dark state. For  $J' = 2$ , however, the laser also couples the  $M = \pm 1$  sublevels to the  $M = \pm 2$  sublevels of the upper state. In this case, there is no longer a dark state. A systematic discussion of the conditions under which dark states exist for a particular transition can be found in [61].

The  $\Omega$ -doublet structure in the  $H$  state and possibly also in the upper state of the

<sup>1</sup>We use the standard notation in which primes refer to the upper state and double primes refer to the lower state in the transition.

transition complicates this picture. Recall that an  $\Omega$ -doublet consists of two states with the same  $J$  and  $M$  but opposite parity, with the  $e$  levels having parity  $(-1)^J$  and the  $f$  levels having parity  $(-1)^{J+1}$ . In the absence of external fields, the  $H$  state  $\Omega$ -doublet is unresolved in our experiment, which means that the state preparation laser always addresses both the  $e$  and  $f$  levels of the  $H$  state. E1 selection rules then determine which levels interact with the laser, as we will see below.

We consider three cases. If there is no  $\Omega$ -doubling in the upper state, only the  $f$  levels of the  $H$  state will participate in a transition with  $J' = J''$ , whereas only the  $e$  levels will participate in a transition with  $J' = J'' \pm 1$ . This situation occurs if we use the  $H \rightarrow E$  transition since the  $E$  state has  $\Omega = 0$ . In this case, the criteria for the existence of a dark state are the same as they would be without  $\Omega$ -doubling. By appropriate choice of  $J'$ , it is possible to prepare a dark state in either the  $e$  or  $f$  levels of the  $H$  state.

If the  $\Omega$ -doubling in the upper state is spectroscopically resolvable, the situation is similar to the case with no  $\Omega$ -doubling. In this case, it is possible to address either the  $e$  or  $f$  levels of the  $H$  state by tuning the laser to the appropriate component of the upper state  $\Omega$ -doublet without needing to tune to a different rotational transition. This is the case when using the  $H \rightarrow C$  transition for state preparation. The splitting of the  $J = 1$   $\Omega$ -doublet in  $C$  measured by our group is 51 MHz, which agrees well with the value of 50.4 MHz derived from the data of [44].

If the  $\Omega$ -doubling in the upper state is not spectroscopically resolvable, the laser always excites transitions to both the  $e$  and the  $f$  levels of the upper state. Since E1 radiation only couples the  $e$  and  $f$  level of the lower state to the one upper state level

that has opposite parity<sup>2</sup>, there is still a dark state for the  $e$  levels and a dark state for the  $f$  levels.

The above discussion applies in the absence of external fields. An external electric field mixes the  $e$  and  $f$  levels and dramatically alters the situation, as we will see in the next section. For a sufficiently large field, the Stark splitting between sublevels of different  $|M|$  is large enough that they can be spectroscopically resolved. In this situation, it is possible to use a transition having a  $J' = 2$  state as the upper state for state preparation, since the undesired transitions to the  $M' = \pm 2$  sublevels will no longer be resonant at the same laser frequency as transitions to the desired  $M' = 0$  state.

## 7.1 The G state

In deciding which transition to use for state preparation in the ACME experiment, we have three choices:  $H \rightarrow E$  at 908 nm,  $H \rightarrow C$  at 1090 nm, and  $H \rightarrow G$  at 787 nm. Both the  $H \rightarrow E$  and  $H \rightarrow C$  transitions are weak, requiring over 1.75 W/cm<sup>2</sup> for saturation<sup>3</sup>. In contrast, the  $H \rightarrow G$  transition is quite strong, requiring less than  $\sim 1$  mW/cm<sup>2</sup> to saturate. The  $E$  state has  $\Omega = 0$  and the  $C$  state has  $\Omega = 1$ , so for these transitions the lowest available rotational level is  $J = 0$  and  $J = 1$ , respectively. Either of these transitions can be used for state preparation with or without an applied electric field.

---

<sup>2</sup>For the  $e$  level of the lower state, for instance, this will be the  $f$  level for a  $J' = J''$  transition and the  $e$  level for  $J' = J'' \pm 1$ .

<sup>3</sup>We define the saturation intensity as the laser intensity past which the observed fluorescence no longer increases with increasing laser intensity. Obviously, this definition depends on the collimation properties of the molecular beam. The quoted value is for a beam similar to the one we anticipate in the ACME experiment.

Although we have demonstrated state preparation using the  $H \rightarrow C$  transition, it is worth considering the  $H \rightarrow G$  transition for this purpose because it would require much less laser power. Investigating this option was one focus of this thesis work. Since the  $G$  state has  $\Omega = 2$ , the lowest rotational level is  $J = 2$ . This means that the  $H \rightarrow G$  transition can only be used for state preparation in an electric field that is sufficiently large that transitions to the  $M' = \pm 2$  levels can be spectroscopically separated from transitions to the desired  $M' = 0$  level. Since the electric dipole moment in the  $G$  state is about half as large as it is in  $H$  state, this requirement is easily met with an applied field of around 40 V/cm. The requirement of an electric field would not have been a problem by itself, since state preparation will take place in the electric field in the ACME experiment.

However, the  $G$  state has another drawback that makes it impossible to use for state preparation: the  $\Omega$ -doublet splitting is very small. Fitting splittings between the two lines of the  $Q$  branch<sup>4</sup> of the  $H \rightarrow G$  transition for  $J = 106 - 150$  measured by [33] to  $\Delta Q = qJ(J+1) + pJ^2(J+1)^2$  and subtracting out the known value of  $q$  for the  $H$  state, we estimate that  $q \sim 32$  kHz for the  $G$  state. The splitting in  $J = 2$  is thus  $qJ(J+1) \sim 192$  kHz, which is smaller than both the Doppler width of the transition with our beam collimation and our laser linewidth<sup>5</sup>.

To see what happens as a result of the unresolved  $\Omega$ -doublet, recall Eqn. (3.18), which gives the eigenstates of the  $J = 1$  level in the  $H$  state in the limit that the Stark splitting is much larger than the  $\Omega$ -doublet splitting. Considering only the upper pair

---

<sup>4</sup>In molecular spectroscopy, transitions with  $J' = J''$  are called  $Q$ , those with  $J' = J'' + 1$  are called  $R$ , and those with  $J' = J'' - 1$  are called  $P$ .

<sup>5</sup>The linewidth of our diode lasers is typically  $\geq 200$  kHz.

of  $|M| = 1$  states, these are

$$\begin{aligned} |\psi_H, M = +1\rangle &= \frac{1}{\sqrt{2}} (|1, 1, e\rangle - |1, 1, f\rangle) \\ |\psi_H, M = -1\rangle &= \frac{1}{\sqrt{2}} (|1, -1, e\rangle + |1, -1, f\rangle), \end{aligned} \quad (7.2)$$

where the state label is  $|J, M, e/f\rangle$ . Now we find the dark state for the transition to  $|2, 0, e/f\rangle$  in the  $G$  state. Expressing the desired dark state as a linear combination of the two lower states with undetermined coefficients  $\alpha$  and  $\beta$  and using Eqn. (7.2), we find

$$\begin{aligned} |d\rangle &= \alpha|\psi_H, M = +1\rangle + \beta|\psi_H, M = -1\rangle \\ &= \frac{\alpha}{\sqrt{2}}|1, 1, e\rangle - \frac{\alpha}{\sqrt{2}}|1, 1, f\rangle + \frac{\beta}{\sqrt{2}}|1, -1, e\rangle + \frac{\beta}{\sqrt{2}}|1, -1, f\rangle. \end{aligned} \quad (7.3)$$

The state  $|d\rangle$  will be dark if the matrix element  $\langle d| -e\mathbf{r} \cdot \boldsymbol{\mathcal{E}} |2, 0, e/f\rangle$  vanishes, where  $\boldsymbol{\mathcal{E}}$  is the electric field of the laser. For an unresolved  $\Omega$ -doublet, the matrix elements for transitions to both the  $e$  and  $f$  states must vanish. For a laser linearly polarized in the  $x - y$  plane, the polarization vector  $\boldsymbol{\epsilon}$  in the spherical basis has only two components,  $\mathcal{E}_{+1} = (\epsilon_x + i\epsilon_y)/\sqrt{2}$  and  $\mathcal{E}_{-1} = (\epsilon_x - i\epsilon_y)/\sqrt{2}$ , where  $\epsilon_x = \boldsymbol{\epsilon} \cdot \hat{x}$  and  $\epsilon_y = \boldsymbol{\epsilon} \cdot \hat{y}$ . The matrix element for transitions induced by this laser is

$$\langle d| -e\mathbf{r} \cdot \boldsymbol{\mathcal{E}} |2, 0, e/f\rangle = -\frac{1}{\sqrt{60}} (\beta \mathcal{E}_{+1} \mp \alpha \mathcal{E}_{-1}), \quad (7.4)$$

where the upper sign holds for the  $e$  state and the lower sign for the  $f$  state. Setting the matrix element in Eqn. (7.4) to zero, the solution for the dark state is

$$\beta = \pm \frac{\mathcal{E}_{-1}}{\mathcal{E}_{+1}} \alpha, \quad (7.5)$$

where again the upper sign holds for transitions to the  $e$  state in  $G$  and the lower sign for transitions to the  $f$  state. The sign difference for the  $e$  and  $f$  states in Eqn. 7.5

occurs because the fully mixed states in the electric field for  $M = +1$  and  $M = -1$  are different linear combinations of  $e$  and  $f$ , as can be seen from Eqn. (7.2). For  $x$ -polarized light,  $\mathcal{E}_{-1} = \mathcal{E}_{+1}$ , while for  $y$ -polarized light  $\mathcal{E}_{-1} = -\mathcal{E}_{+1}$ . For  $x$ -polarized light, Eqn. (7.5) tells us that the state with  $\beta = -\alpha$  is dark for transitions to the  $e$  state. Unfortunately, because of the different signs in Eqn. (7.5), this state is bright for transitions to the  $f$  state. Similarly, the state with  $\beta = \alpha$  is dark for transitions to the  $f$  state and bright for transitions to the  $e$  state.

The above discussion demonstrates that it is impossible to use E1 transitions to the  $G$  state for preparing the initial state for the eEDM measurement; thus, one of the alternative transitions ( $H \rightarrow E$  at 908 nm or  $H \rightarrow C$  at 1090 nm) must be used instead. Since both transitions are weak, an amplifier after the diode laser is needed to provide enough power to saturate the transition. The availability of fiber amplifiers at 1090 nm makes it possible to obtain significantly more power (up to 20 W) at this wavelength than is available at 908 nm, where the highest power option is a 1.5 W tapered amplifier. Thus, we are currently using the  $H \rightarrow C$  transition for both state preparation and detection. The reason there is no dark state for the  $H \rightarrow G$  transition even in an electric field was only recognized after we were unable to experimentally prepare a dark state using this transition.

## 7.2 A new normalization scheme

The unsuccessful attempt to prepare a dark state using the  $H \rightarrow G$  transition resulted in a more careful consideration of transitions between  $\Omega$ -doublet states in an electric field, which led to a promising new technique for normalizing the signal in

the eEDM experiment. As discussed in Chapter 4, the large fluctuations in molecule yield from one beam pulse to the next make it essential to normalize the signal to the total number of molecules in each pulse.

To see how we might do so, let's reconsider the  $|H, J = 1\rangle \rightarrow |C, J = 1\rangle$  transition. As before, we are interested in transitions from the  $M = \pm 1$  levels in  $H$  to the  $M = 0$  level in  $C$ . Since the  $\Omega$ -doublet splitting in the  $C$  state is spectroscopically resolvable, we can choose to excite transitions either to the  $e$  state or the  $f$  state in  $C$  simply by tuning the laser. To start, let's consider transitions only to the  $e$  state. In this case, the dark state for excitation with  $x$ -polarized light is  $|d_X\rangle = (|M = +1\rangle - |M = -1\rangle)/\sqrt{2}$ , so the opposite linear combination,  $|d_Y\rangle = (|M = +1\rangle + |M = -1\rangle)/\sqrt{2}$ , is the state that interacts with the laser. For  $y$ -polarized light, the dark state is  $|d_Y\rangle$ , while the state that interacts with the laser is  $|d_X\rangle$ . The effect of switching from  $x$  to  $y$  polarization is to change the relative sign of the  $|M = +1\rangle$  and  $|M = -1\rangle$  states in the linear combination that interacts with the laser. As Eqn. 7.5 shows, the same sign change occurs if we keep the laser polarization fixed, but switch from using the  $e$  state as the upper state to using the  $f$  state. Thus, we can access the two quadratures  $|d_X\rangle$  and  $|d_Y\rangle$  *either* by switching the laser polarization from  $\hat{x}$  to  $\hat{y}$  or by switching the upper state of the transition from  $e$  to  $f$ . The latter switch is easily accomplished by shifting the laser frequency using an acousto-optic modulator (AOM).

The ACME experiment initially proposed to measure both quadratures  $|d_X\rangle$  and  $|d_Y\rangle$  of the signal many times within each molecule pulse by rapidly switching the polarization of the detection laser between  $\hat{x}$  and  $\hat{y}$  using an electro-optic modulator



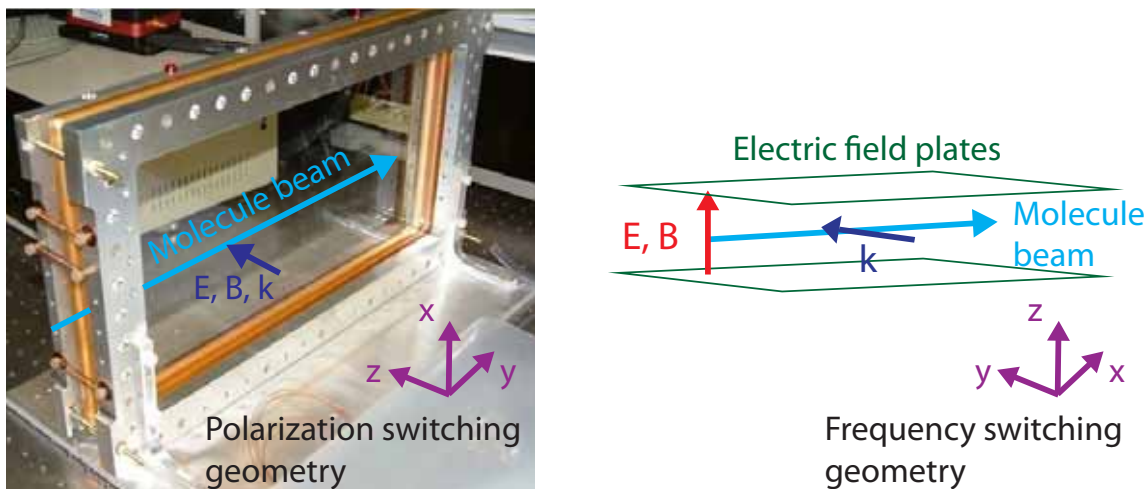


Figure 7.2: Geometry of electric field plates and laser beams for the polarization switching and frequency switching normalization schemes.

(EOM) [41]. Ideally, we would like to switch the polarization sufficiently fast that each molecule has a chance to interact with both polarizations during the time it spends in the laser beam. For a 2 mm wide beam, this time is about  $10 \mu\text{s}$ , necessitating a switching frequency of 200 kHz. How fast the polarization can be switched with our EOM while maintaining a high contrast remains to be investigated. Regardless of the achievable switching speed, a significant drawback of the polarization switching scheme is that it necessitates sending the laser beams through the electric field plates since there must be two polarization axes to switch between, both orthogonal to the electric field direction. Since at least some of the laser beams will have several watts of power, reflections from the field plates could create standing waves between the plates and distort the electric field. Moreover, the necessity of keeping the detection laser beam path clear precludes placing the fluorescence collection lenses at the locations where collection efficiency is maximal, resulting in lower detection efficiency.

The alternative normalization scheme discussed here would keep the polarization

fixed and rapidly switch the frequency of the detection laser such that it excites transitions either to the  $|1, 0, e\rangle$  or the  $|1, 0, f\rangle$  state in  $C$ . This can be done using an AOM since the frequency difference between the two  $\Omega$ -doublet components is 51 MHz. This method only requires one available polarization direction orthogonal to the electric field, which makes it possible to send the lasers between the electric field plates instead of through them, as shown in Fig. 7.2.

Such an arrangement has many advantages. It would eliminate problems associated with scattering of the laser light by the field plates. It would allow placement of the fluorescence collection optics in the optimal locations, resulting in enhanced detection efficiency. Finally, it would dramatically simplify the implementation of a more efficient method of state preparation via stimulated Raman adiabatic passage (STIRAP). STIRAP offers much higher excitation efficiency than optical pumping via the  $A$  state and would immediately produce the desired coherent superposition of  $M = \pm 1$ , eliminating the need for an additional state preparation step. However, it requires a laser polarized parallel to the electric field, which is impossible in the current geometry since the laser beams propagate along the electric field direction. A challenge of the new normalization scheme that remains to be investigated is that the two levels of the  $C$  state  $\Omega$ -doublet decay via different channels<sup>6</sup>, resulting in different spatial distributions of the emitted fluorescence, which means that the detection efficiencies differ for the two transitions.

Fig. 7.3 illustrates the principle of this normalization scheme. This data was taken

---

<sup>6</sup>Using the notation  $|J, M, \mathcal{P}\rangle$ , where  $\mathcal{P} = \pm 1$  is the parity, the two states of the  $\Omega$ -doublet are  $|1, 0, +1\rangle$  and  $|1, 0, -1\rangle$ . The  $|1, 0, +1\rangle$  state must decay to  $J = 1$  in the  $X$  state and this transition has  $\Delta M = \pm 1$ . The  $|1, 0, -1\rangle$  state can decay to  $J = 0$  or  $J = 2$  (but mostly decays to  $J = 0$ ) and this transition has  $\Delta M = 0$ .

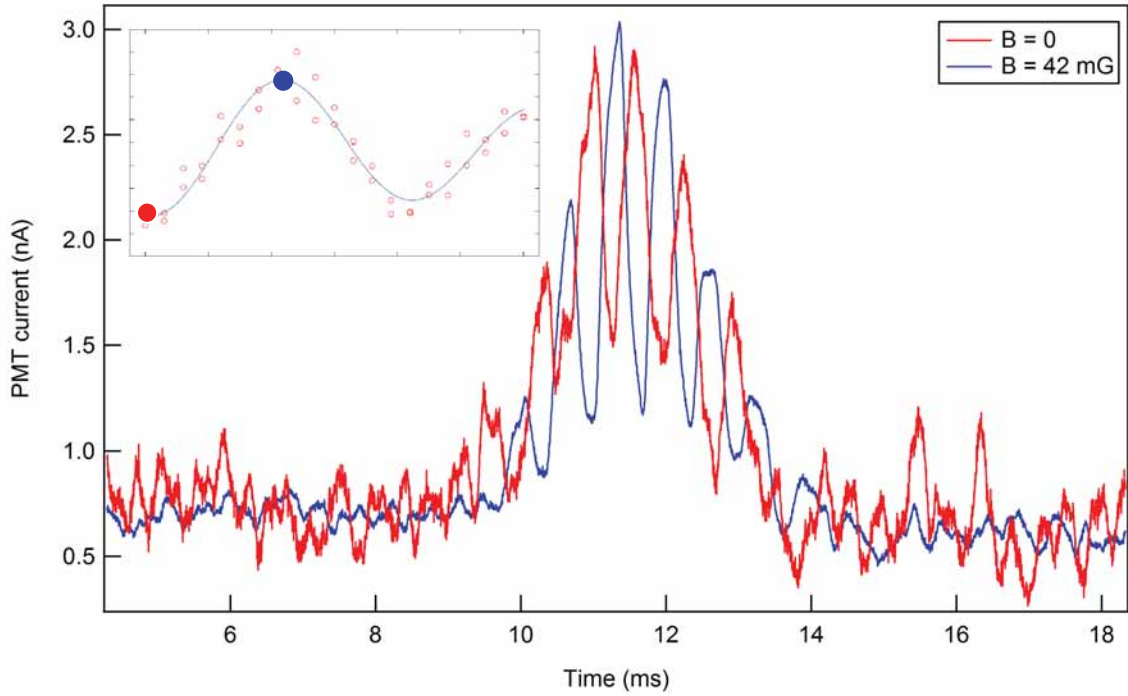


Figure 7.3: Data taken with the frequency of the detection laser switched rapidly between resonance with the  $e$  level and the  $f$  level of the  $C$  state  $\Omega$ -doublet. Data is shown for  $B = 0$  (red) and for  $B = 42$  mG (blue). The colored dots on the inset indicate the position on the Ramsey fringe where the corresponding data was taken. The signals from the minimum and maximum points on the fringe are out of phase because the transitions to the  $e$  and  $f$  states address opposite quadratures  $|d_X\rangle$  and  $|d_Y\rangle$  of the molecular state. The switching speed for this data was 1.5 kHz.

using the main beam apparatus, described in detail in Section 6.1. The frequency of the detection beam was rapidly switched between the two  $\Omega$ -doublet levels of the  $C$  state using two AOMs with a frequency difference of 51 MHz. The diffracted beams from both AOMs were combined using a 50/50 beamsplitter and sent to the input of the fiber amplifier that produces the detection beam. To enable frequency switching, the RF signal driving each AOM was sent through a switch (Mini-Circuits ZYSWA-2-50DRB), with the two switches arranged so that one RF signal is on while the other is off. The switching frequency used here was much slower than what is

needed for the eEDM experiment. The choice of such a low frequency was dictated by signal to noise requirements; increasing the switching frequency requires increasing the detection bandwidth, which leads to larger noise levels. This data was taken using one-eighth of the fluorescence collection optics that will be used for the final experiment. Installing all the collection lenses, which will be done shortly, should significantly improve the signal to noise, allowing demonstration of faster frequency switching.

## Chapter 8

## Conclusion

We describe work towards the ultimate goal of the ACME collaboration - making an eEDM measurement using a cryogenic beam of ThO. All the lasers necessary for this experiment have been built, along with a versatile system to stabilize and controllably tune the laser frequencies. This system can stabilize the laser frequencies to about 1 MHz and has been used for all the ThO beam measurements done at Harvard thus far. The laser locking system discussed here has the advantages of simplicity, scalability, and ease of use, while its main disadvantage is the low achievable bandwidth. In the future, a higher bandwidth stabilization system will be necessary to eliminate acoustic noise and provide better frequency stability.

A new measurement of the  $H$  state magnetic moment is reported that uses a very different technique from the one employed for the previous determination of this quantity. The current measurement relies on observing precession of the angular momentum in a magnetic field, combined with a pulsed excitation technique that allows selection of molecules by velocity, thus reducing the error due to the longitu-

dinal velocity spread of the ThO beam. We find  $g = (7.6 \pm 0.4) \times 10^{-3}$ , which is in agreement with the previous measurement of  $g = (8.5 \pm 0.5) \times 10^{-3}$ . The consistency of these results provides important confirmation of the low sensitivity of the  $H$  state to magnetic fields, which is a key advantage of ACME compared to other molecular eEDM experiments.

Our unsuccessful attempts to prepare a dark state using the  $H \rightarrow G$  transition resulted in a more careful consideration of matrix elements for transitions between  $\Omega$ -doublet states in an electric field. This led to the realization that transitions to the  $e$  and  $f$   $\Omega$ -doublet levels sample different quadratures of the molecular state, so switching between them is equivalent to switching the laser polarization from  $\hat{x}$  to  $\hat{y}$ . This makes it possible to normalize the eEDM signal by rapidly switching the detection laser frequency from one of the  $C$  state  $\Omega$ -doublet levels to the other. Initial results using this method are promising, but more work remains to be done to demonstrate switching at the high frequencies needed for the eEDM measurement.

The  $C$  state switching normalization scheme promises to allow a more efficient geometry of the interaction region in which lasers are sent between the electric field plates rather than through them, as is currently done. This has the advantages of eliminating scattering of laser light by the field plates, allowing more optimal placement of the fluorescence collection lenses, and simplifying the addition of more efficient state preparation (e.g. using stimulated Raman transitions) in the future.

# Appendix A

## Diode laser assembly instructions

This appendix provides instructions for assembling external cavity diode lasers like the ones used on the ACME experiment. No previous experience with diode lasers is assumed. Those new to diode lasers may want to read [62] for background information.

### A.1 Precautions

Follow these guidelines to avoid damaging your laser diode.

1. Laser diodes are easily damaged by static discharge. To avoid this, wear a grounding strap whenever you handle a laser diode or touch anything inside the laser enclosure (i.e. while adjusting the collimation lens, turning the precision screws, etc.).
2. Laser diodes can also be damaged by sudden changes in current. Laser current controllers are designed to ramp the current up and down slowly when you turn

the laser on and off. When connecting the laser to the current controller, use a cable that has jackscrews which secure the connector to the plug at each end. This prevents the cable from being accidentally pulled out while the current is on, an event which could easily kill the laser diode.

3. The sensitivity of laser diodes to optical feedback is exploited in the external cavity setup. To avoid undesired feedback due to reflections from optics in the beam path that go back into the laser diode, place an optical isolator after the output of the laser. The isolation should be at least 30 dB, although 60 dB is recommended if you are planning to couple a significant fraction of the laser light into an optical fiber. If there is insufficient isolation, feedback from optics in the beam path will affect the laser's behavior. Since the amount of feedback depends sensitively on the alignment of the optical element(s) providing it, you can test for feedback from a particular optic by monitoring the laser's spectrum on a Fabry-Pérot cavity while changing the alignment of that optic.

## A.2 Selecting the grating

The choice of grating depends on the wavelength of the laser diode and the amount of feedback desired. In the Littrow configuration, the first-order diffracted beam from the grating returns along the same path as the input beam from the laser diode; this beam provides the feedback that controls the lasing wavelength. In this configuration, the following relationship holds between the diffraction angle  $\alpha$ , the number of lines



per millimeter  $N_\ell$  on the grating, and the wavelength  $\lambda$  of the light

$$\alpha = \arcsin\left(\frac{\lambda N_\ell 10^{-6}}{2}\right). \quad (\text{A.1})$$

In Eqn. (A.1),  $\alpha$  is in radians,  $\lambda$  is in nanometers, and  $N_\ell$  is in lines/mm. The number of lines per millimeter should be chosen such that  $\alpha$  is approximately  $\pi/4$ . Since the zeroth-order beam reflected from the grating is the output beam, choosing  $\alpha$  in this way will make the output beam exit approximately perpendicular to the input beam. This choice is determined by convenience rather than necessity, so it doesn't have to be exact. Gratings are commonly available only with certain values of  $N_\ell$  so choose from the available options the one that gives  $\alpha$  closest to  $\pi/4$ .

The diffraction efficiency at the laser wavelength tells you what fraction of the light incident on the grating is diffracted into the first order<sup>1</sup>. This determines the amount of feedback your laser will have, with higher diffraction efficiency giving stronger feedback but reducing the output power of the laser since more light is diffracted back into the diode. Typical values of the grating efficiency for a Littrow laser are around 10 - 20%. Less feedback can be used if a high output power is desired; however, a laser with less feedback will generally have a smaller tuning range than one with stronger feedback.

### A.3 Circuit board assembly

Assemble the circuit board before starting to assemble the laser. The design of this board was taken from the Greiner group [50]. We have our boards made by

---

<sup>1</sup>In reading grating efficiency curves, look at the values for polarization parallel to the grating grooves since the laser diode will be oriented so that its output is vertically polarized.

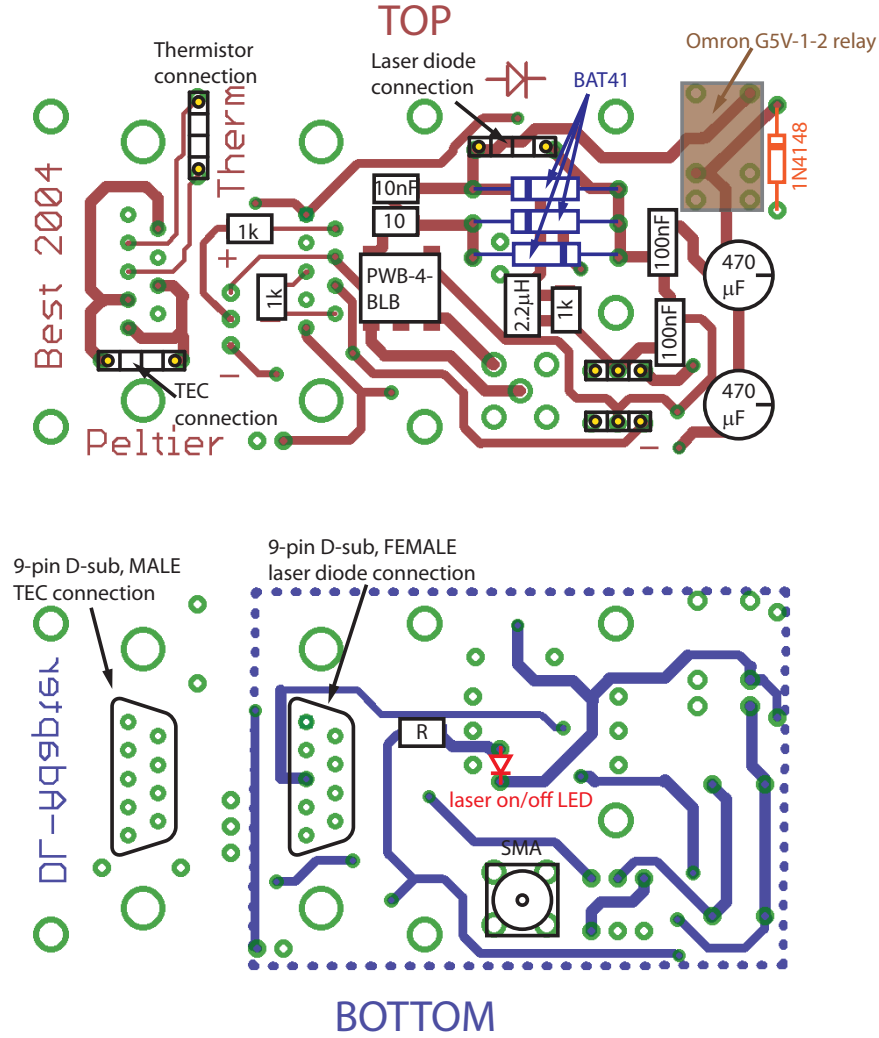


Figure A.1: Layout of components on the circuit board: (a) top and (b) bottom. Numbers without units denote resistances in Ohms. Orientation of the diodes (BAT41 and 1N4148) is indicated by the lines (the line denotes the cathode). Orientation of the polarized 470  $\mu\text{F}$  capacitors is indicated by the “-” sign on the capacitor symbol. The resistance  $R$  on the bottom of the board should be 0  $\Omega$  for Thorlabs controllers and 680  $\Omega$  for Toptica controllers.

Alberta Printed Circuits. Table A.1 lists the parts needed for assembling the circuit board.

Fig. A.1 shows the placement of components on the board. Strip headers (see

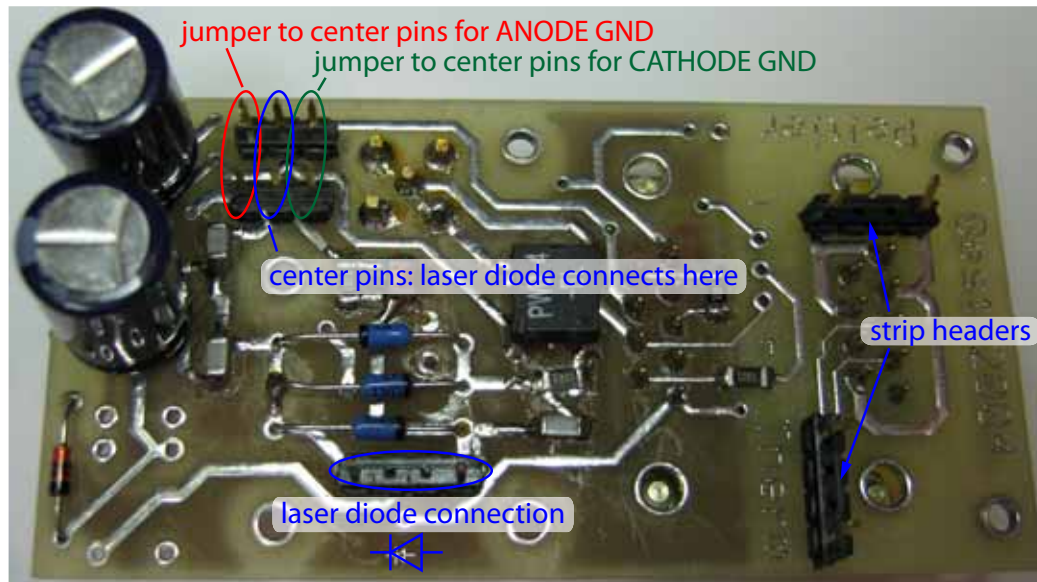


Figure A.2: The laser diode should always be connected to the pins labeled “laser diode connection” in the orientation indicated by the diode symbol. The jumpers in the upper left corner should be set according to whether the laser diode is cathode ground or anode ground.

Fig. A.2 for a picture) are used for connecting the thermistor, TEC, and laser diode to the circuit board. Cut them to lengths of four pins, pull out the two middle pins, and solder the end pins into the holes indicated in Fig. A.1. The laser diode is *always* connected in the orientation indicated by the diode symbol printed on the circuit board directly above the pins where the diode connects (see Fig A.2). Also solder 3-pin lengths of strip header into the two sets of three holes between the SMA connector and the  $470\ \mu\text{F}$  capacitors. These connections define the direction of the current. The center pin of each set of three pins is connected to the laser diode via traces on the circuit board. Depending on whether your laser diode is cathode ground or anode ground, you need to jumper either the left or the right pin in both sets of three to the center pin (see Fig A.2).

The hole pattern in the upper right corner of the circuit board next to the 1N4148

Table A.1: Circuit board components.

Part #	# per board	Vendor	Description
RNCS32T91K0.1%ICT-ND	3	Digi-Key	Resistor, 0.25 W, 1 k $\Omega$ , 1206 package
RNCS32T9100.1%ICT-ND	1	Digi-Key	Resistor, 0.25 W, 10 $\Omega$ , 1206 package
490-1767-1-ND	2	Digi-Key	Ceramic capacitor, 0.1 $\mu$ F, 25 V, C0G, 1206 package
445-1375-1-ND	1	Digi-Key	Ceramic capacitor, 10000 pF, 50 V, C0G, 1206 package
P5168-ND	2	Digi-Key	Capacitor, 470 $\mu$ F, 35 V, aluminum electrolytic, radial leads
497-2493-1-ND	3	Digi-Key	BAT41 Schottky diode, 100 V, 100 mA
ED7250-ND	1	Digi-Key	Strip header
ED6350-ND	1	Digi-Key	Strip header socket
A26242-ND	2	Digi-Key	Strip header jumper
44K0365	1	Newark	1N4148 Small signal diode, 100 V, 150 mA
27C8063	1	Newark	PCB mount SMA connector
93F8882	1	Newark	PCB mount 9-pin D-sub connector, female <sup>1</sup>
93F8883	1	Newark	PCB mount 9-pin D-sub connector, male <sup>1</sup>
ED5003-ND	2	Digi Key	Pin receptacle, we use these to connect the laser diode
1008CS-222XGLB	1	CoilCraft	2.2 $\mu$ H chip inductor, 1008 package
PWB-4-BLB	1	CoilCraft	RF transformer, 0.140 – 700 MHz bandwidth

<sup>1</sup> These connectors do not come with jackscrews, which are needed to allow the cable to be screwed to the plug to prevent it being accidentally pulled out. Jackscrews can be purchased separately from Newark or L-Com.

diode is designed to accommodate an Omron G5V-1-2 relay, which would short-circuit the laser diode whenever the current is disabled. This protects the laser diode from static discharge. The relay requires 12 V to open and allow current to flow through the laser diode. Since the Thorlabs controllers don't have an appropriate output, we do not install this relay on our lasers.

The circuit board is attached to Side1 (see Fig. A.3) with 2-56 screws. Put some plastic washers or standoffs between the board and Side1 to prevent shorting. To connect the laser diode to the circuit board, you can use a commercial socket (i.e. Thorlabs S7060R for 5.6 mm diodes or S8060 for 9 mm diodes). We use pin receptacles (Digi-Key ED5003-ND) covered with heat shrink to prevent them from shorting to each other. Whatever connector you use, make sure it does not come loose when you rotate the laser diode, as you will be doing this later to align the beam polarization.

### A.3.1 Current, temperature, and PZT controllers

Table A.2: Pin assignments for laser connector on circuit board.

Pin #	Connection
1	Interlock
2	Photodiode cathode
3	Laser diode ground
4	Photodiode anode
5	Ground for Pin 1
6	Not used
7	Laser diode cathode (with polarity anode ground)
8	Laser diode anode (with polarity cathode ground)
9	Not used

We use Thorlabs current and temperature controllers for all our home-made lasers.

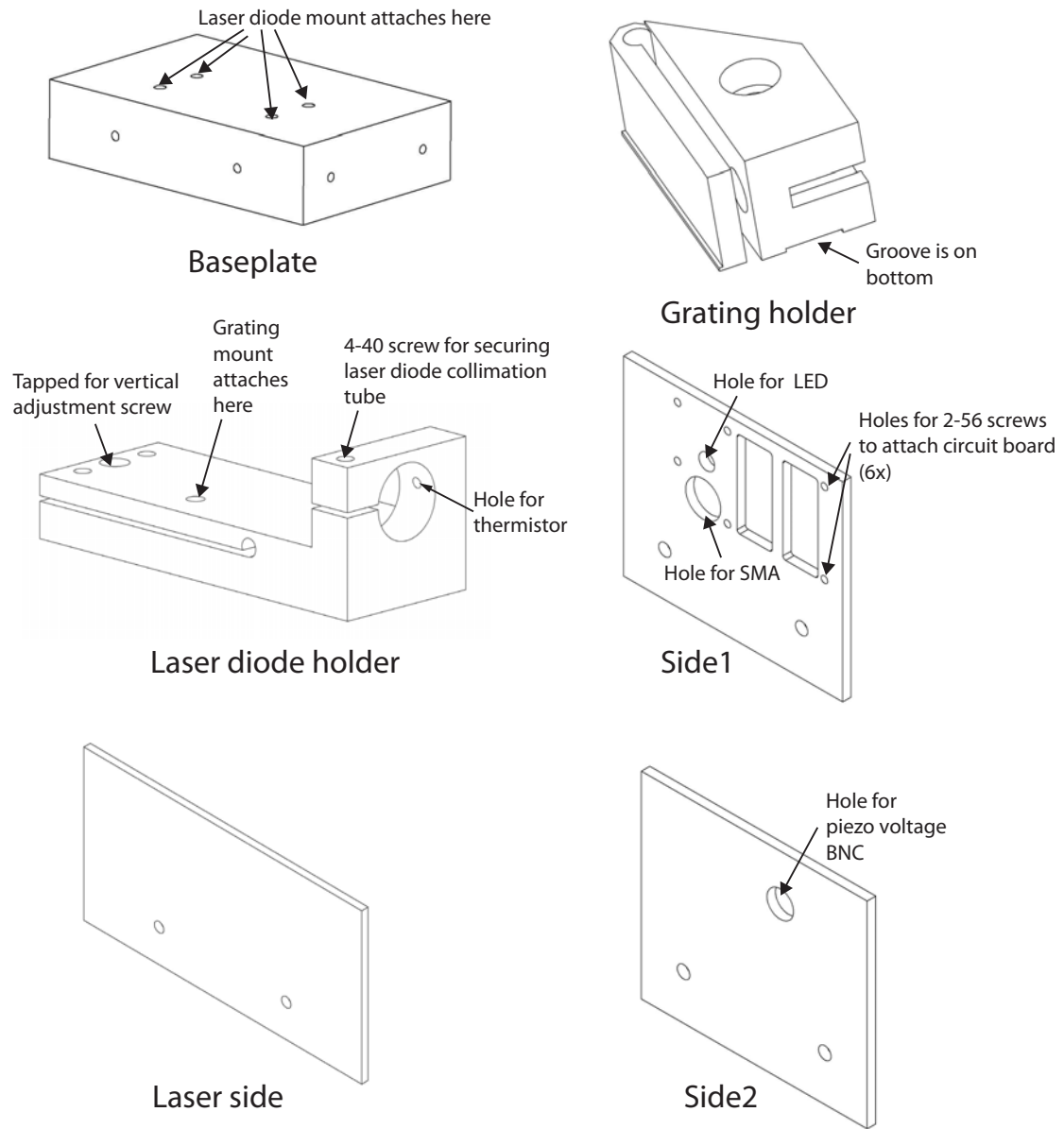


Figure A.3: Laser parts that need to be machined.

The pinouts for the 9-pin D-sub connectors on the circuit board are given in Tables A.2 and A.3. Toptica controllers have the same pinouts, so using them only requires changing one resistor on the circuit board. This is the only resistor on the back of the board, which should be a short ( $0\ \Omega$ ) for Thorlabs controllers and  $680\ \Omega$  for Toptica

Table A.3: Pin assignments for TEC connector on circuit board.

Pin #	Connection
1	Status LED + (for TEC on/off indication)
2	Thermistor -
3	Thermistor +
4	TEC +
5	TEC -, Status LED -
6	Not used
7	AD 590 -, LM335 +
8	AD 590 +, LM335 +
9	AGND LM335

controllers.

For PZT adjustment, we use a stable voltage source based on a ADR445 voltage reference, which provides an adjustable output ranging from -10 V to +10 V<sup>2</sup>. Since we use a low-voltage PZT<sup>3</sup>, this voltage range is sufficient for our needs. For modulating the frequency, a function generator can be used to drive the PZT.

## A.4 Laser assembly instructions

Fig. A.3 shows the parts that need to be machined, while Table A.4 lists additional parts needed for the laser and where to purchase them. The first step in laser assembly is to check that the 10 k $\Omega$  thermistor you have will fit into the small hole in the side of the laser diode mount. If the thermistor doesn't fit, drill out the hole using the smallest size drill large enough to accommodate your thermistor. At the same time, make sure the laser diode collimation tube fits in the large hole in the laser

<sup>2</sup>This circuit was designed by Jim MacArthur of the Harvard Electronic Instrument Design Lab.

<sup>3</sup>The voltage range of the piezo is -30 V to +150 V.

Table A.4: Laser parts that need to be purchased.

Part #	Vendor	Description
TH10K	Thorlabs	10 k $\Omega$ thermistor
TE-71-1.4-1.5	TE Technology	TEC module <sup>1</sup>
93939A199	McMaster-Carr	1" long nylon screw for attaching laser mount to base-plate
LT230P-B	Thorlabs	collimation tube for laser diode <sup>2</sup>
PSt 150/4/5	Piezomechanik	PZT for laser wavelength tuning <sup>3</sup>
AJS8-100-02H	Newport	precision adjustment screw (need two per laser)
NT45-567	Edmund Optics	sapphire window to put under ball of vertical screw
CSXX-0096-05	Small Parts	springs to provide resistance for vertical adjustment
CU-234	Newark or DigiKey	Bud box for laser base

<sup>1</sup> Buy the module potted

<sup>2</sup> “B” specifies the AR-coating; choose the appropriate coating for your laser wavelength.

<sup>3</sup> This part number is not in the catalog; you need to email Piezomechanik and ask for it. This cylindrical PZT comes either with two flat ends or with one flat end and one hemispherical end. Either type will work, but those with one hemispherical end are better.

diode holder. This hole should be a tight fit for the collimation tube<sup>4</sup>, but it must be physically possible to get the collimation tube in there and rotate it. If the collimation tube doesn’t fit, lightly sand the inside of the hole until it does. Before beginning the assembly, make sure all the parts are thoroughly cleaned and degreased.

Now attach the thermistor. Dip it in thermal grease before placing it in the hole. Locate it as close as possible to the inner edge of the hole where the collimation tube will go, but make sure it doesn’t protrude into the hole. Since the temperature of the laser diode is the crucial parameter, the thermistor should be as close as possible to the collimation tube that holds the diode. The thermistor is held in place by putting five-minute epoxy around the leads on the outside of the hole.

---

<sup>4</sup>This is necessary to ensure good thermal contact between the laser diode mount, which is temperature controlled, and the collimation tube, which holds the laser diode whose temperature you want to stabilize.



Next, attach the laser diode holder to the baseplate, with the TEC sandwiched between the two. It is crucial that the TEC is oriented correctly so that the cold side is touching the laser diode holder and the hot side is touching the baseplate. The cold side is the side whose temperature is controlled, whereas the hot side is where excess heat is rejected. To figure out which side is which, place the TEC module in front of you with the wires pointing toward you. If the red wire is on the right, the hot side of the module is facing downward. Before attaching the TEC, sand the bottom of the laser diode holder and the top of the baseplate with fine sandpaper. This removes surface imperfections so that the parts make good thermal contact to the TEC.

Put a thin layer of thermal grease on the hot side of the TEC and set it on top of the baseplate in approximately its final position. You want the TEC as close as possible to the end of the laser diode holder where the collimation tube will go. Put another thin layer of thermal grease on the cold side of the TEC and place the laser diode holder on top. Use the 1 inch long plastic screws to attach the laser diode holder to the baseplate. These screws must be plastic in order to keep the baseplate and laser diode holder thermally isolated from each other. Tighten the screws sequentially in small increments, making sure throughout the process that you are tightening all four screws evenly. Try not to overtighten since you can break the screws. Some thermal grease will squeeze out during this process. Carefully wipe off it off to prevent it from making a thermal connection between the laser diode holder and the baseplate. Wait an hour or so for the thermal grease to settle and then tighten the screws a little more.

Next attach the base, which for our lasers consists of a Bud box filled with lead

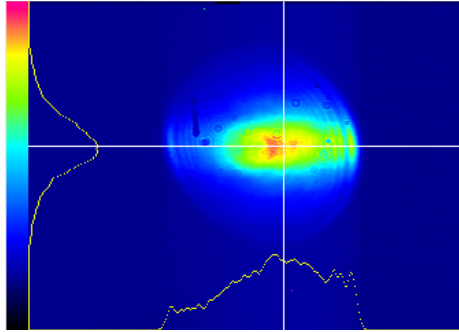


Figure A.4: CCD camera image of a beam with the laser diode off center with respect to the collimation lens, so that the beam is clipped on the right side.

shot<sup>5</sup>. Drill a 1/4-20 through hole roughly in the middle of the bottom of this box. A screw through this hole into the tapped hole on the bottom of the baseplate attaches the baseplate to the box. The lead shot makes the base heavy to reduce vibrations. It is useful to glue a layer of Sorbothane<sup>6</sup> on the lid of the box, which is the bottom of the laser, to further isolate the laser from vibrations.

Now mount the laser diode in the collimation tube. Mount the collimation tube in the laser diode holder, but don't tighten the 4-40 screw that secures it yet. Turn on the laser and rotate the collimation tube until the long axis of the output beam is horizontal. If you cannot tell which axis is the long one, rotate the collimation tube until the output polarization is vertical. If possible, look at the beam on a beam profiler to make sure that the laser diode is aligned properly. It is possible for the laser diode to be sufficiently off center in the collimation tube that the output beam is clipped by the edge of the collimation lens. Fig. A.4 shows how this might look. Since there is no controllable way to adjust the centering of the diode, the only solution is

---

<sup>5</sup>This can be bought from McMaster-Carr.

<sup>6</sup>Sorbothane is a rubber-like material designed for reducing vibration. It can be purchased from McMaster-Carr.

to unscrew the diode, wiggle it around and/or rotate it, and screw it back in. Once the laser beam is oriented correctly, tighten the 4-40 screw to secure the collimation tube in the laser diode holder.

To adjust the collimating lens, look at the beam several meters away from the laser. You want to adjust the lens such that the length of the long (horizontal) dimension of the beam does not change much between a location several inches from the laser to several meters away. The small (vertical) dimension of the beam will increase significantly. The beam far away from the laser will probably look quite bad (i.e. brighter on one side than on the other, made up of several vertical stripes of varying brightness, etc.); in our experience, this doesn't matter. Ensure that the beam is not obviously diverging or converging and that it does not come to a focus anywhere along the path from the laser to several meters away. When you are done adjusting the collimation lens, put a few drops of five-minute epoxy around the edges of the lens to hold it in place.

Quite often you will find that the height of the beam changes significantly over a distance of several meters. This occurs because the laser diode output is not centered on the collimation lens, so the lens deflects the beam. This is only a problem if the inclination is severe enough that you cannot direct the first-order diffracted beam from the grating back into the laser diode using the vertical adjustment screw on the edge of the laser diode mount. If you are concerned about this, it is a good idea to attach the grating mount and grating and try to obtain feedback (see Section A.4.2 for how to do this). If you succeed, don't worry about the beam inclination, as it can be easily corrected once the beam exists the laser. If you cannot obtain feedback within

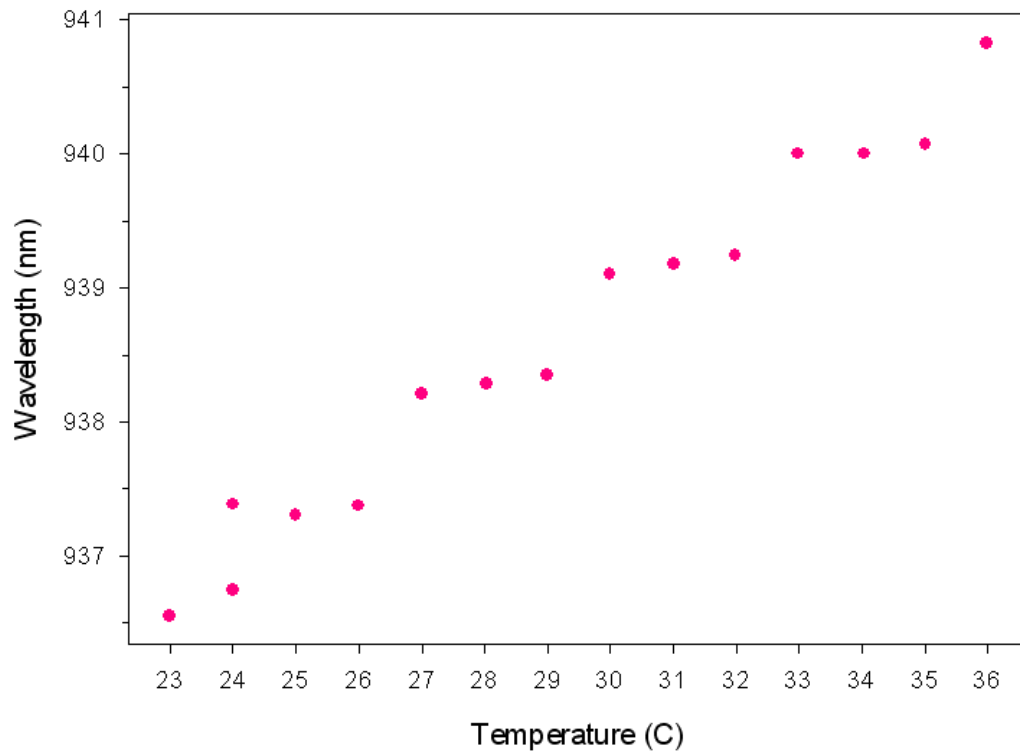


Figure A.5: Wavelength as a function of temperature for a 940 nm diode. The line segments correspond to temperature tuning of a single mode due to change in the length of the emission region, while the discontinuous jumps are mode hops.

the available range of vertical adjustment, loosen the laser diode in the collimation tube, rotate it about ninety degrees, and screw it back in. Make sure you are satisfied with the inclination of the beam before moving on, as it will be difficult to change it later.

At this point, get a sense of what temperature to operate the laser diode by measuring its free-running wavelength as a function of temperature. Measure this at a current close to the intended operating current. It is helpful to put on the sides and top of the laser enclosure while doing this measurement to isolate the diode from air currents. Fig. A.5 shows a typical curve of wavelength versus temperature. Increasing

the temperature makes the emission wavelength longer. Ideally, you want to operate the diode at a temperature where its the free-running wavelength is close to the desired wavelength. However, running a laser diode at elevated temperature has the effect of reducing its output power for a given current and decreasing its lifetime. The specifications should list a maximum operating temperature for the laser diode, so be sure not to exceed this value. The proper choice of operating temperature reduces the amount you have to tune the wavelength using the grating. This is advantageous since changing the grating angle reduces the feedback, which imposes a limit to how far it is possible to tune using the grating.

At this point, assemble all remaining parts of the laser. Put a small sapphire window under the ball of the vertical precision adjustment screw in the laser diode mount. This prevents the ball from digging into the aluminum underneath, which could cause the vertical adjustment to drift over time. The two holes on either side of the vertical adjustment screw are for 3-48 screws with springs placed between the cap of the screw and the laser diode mount, as shown in the Fig. A.6. Tighten the screws until there is enough tension in the springs to provide noticeable resistance when you turn the precision adjustment screw. The springs help keep the vertical adjustment stable by opposing upward motion of the lip of the laser diode mount, which is not constrained by the adjustment screw.

#### **A.4.1 Tuning the temperature control loop**

When the laser is completely assembled, tune the control loop parameters of the temperature controller. Especially for high-power lasers, you should do this with the

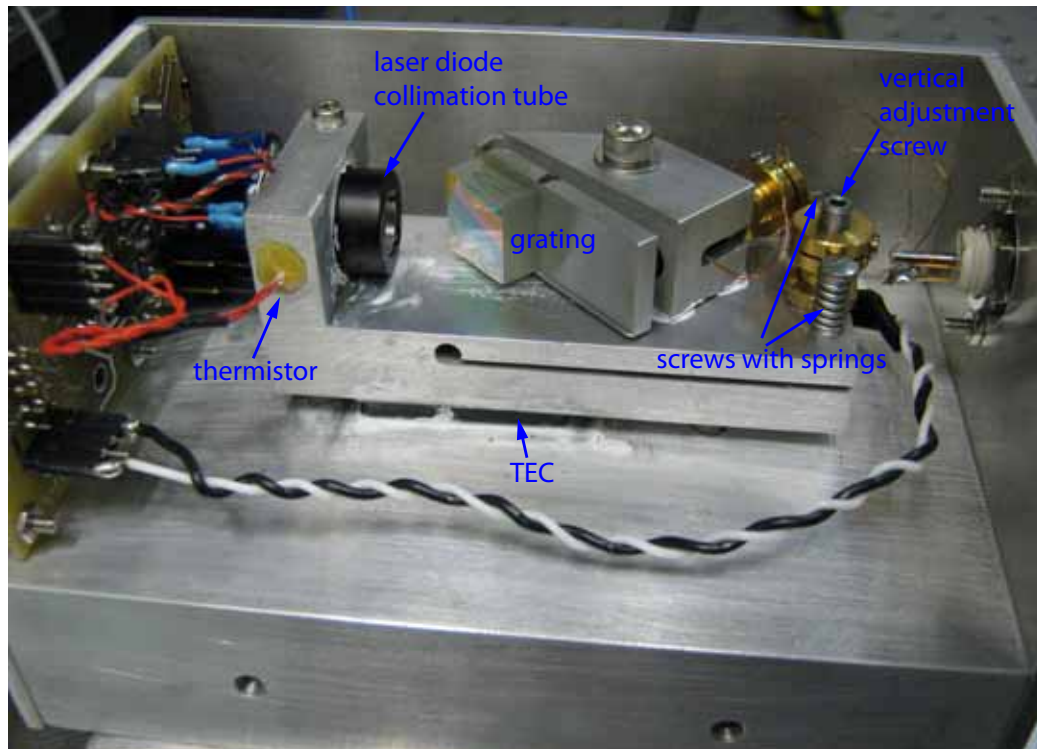


Figure A.6: View of assembled laser. The screws with springs provide resistance for vertical adjustment using the precision adjustment screw.

laser running close to the intended operating current. The instructions below assume you are using a Thorlabs temperature controller, although the same basic technique applies to any controller with adjustable proportional (P), integral (I), and derivative (D) gains. To start, set all gains to zero. If possible, disable the integral gain. It is much more convenient to tune the gains while monitoring the output voltage from the controller, which is proportional to the temperature. We use a National Instruments data acquisition card to read the voltage into the computer and plot it using LabVIEW.

Begin by setting the P gain to some value, say half a turn of the knob on the

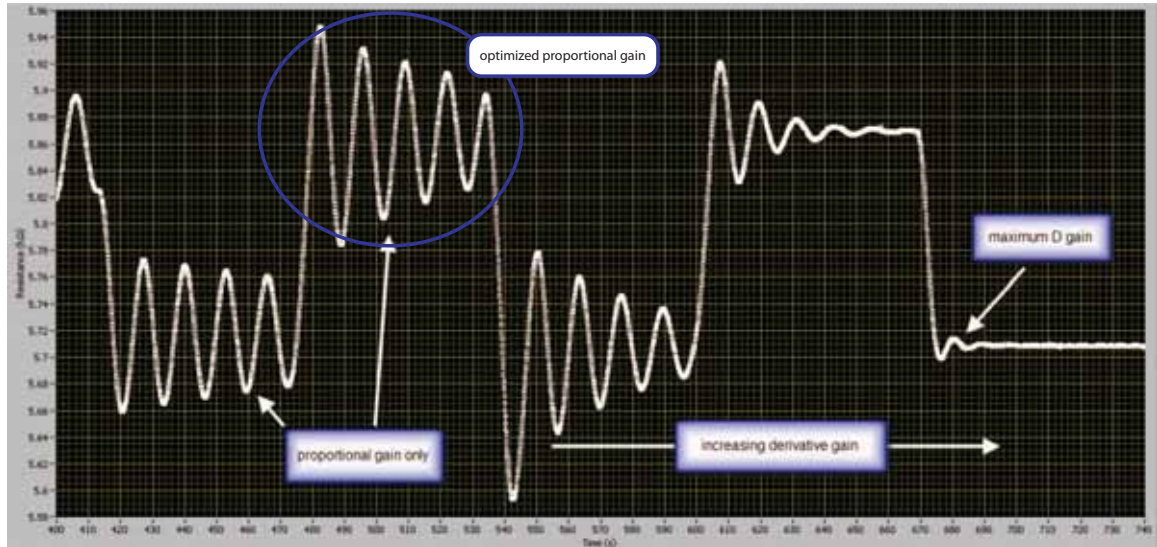


Figure A.7: Example of the sort of responses you will see while tuning the temperature control loop.

Thorlabs controller. Next change the setpoint by  $0.3 \text{ k}\Omega$ <sup>7</sup>. The output voltage from the controller will change suddenly and then oscillate for a while before eventually settling to its new value. Keep increasing the P gain until the oscillations after the step in setpoint are only slightly damped (see Fig. A.7). If you increase P beyond this value, the oscillations will not damp out at all. Leaving P at its current value, set the D gain to some value, say half a turn on the Thorlabs controller. Again make a sudden change in setpoint and monitor the output. The oscillations should now damp out more quickly. Keep increasing D until the response shows no overshoot<sup>8</sup>. Once P and D are optimized, you can try turning on the integral gain. In my experience, it is best to leave it off on the Thorlabs controllers. The effect of the integral gain is to make the temperature settle to the setpoint; without integral gain, there will be

<sup>7</sup>We quote the change in resistance of the  $10 \text{ k}\Omega$  thermistor since this is what the Thorlabs controllers read out. This corresponds to about  $0.7^\circ\text{C}$  near room temperature.

<sup>8</sup>This may not be possible with some controllers (for instance, the older Thorlabs TEC2000), but do the best you can.

an offset between the setpoint and the actual temperature. Turning on the integral gain tends to also increase the overshoot and oscillations before the temperature settles to its final value. For this reason, we leave it disabled for all our lasers. It is easy to compensate for the resulting offset by adjusting the setpoint until the actual temperature is at the desired value. After tuning the temperature loops for about ten lasers of different power levels, we find that the best settings for Thorlabs controllers are always in the following range:

- **P**: about 62.5% of maximum value
- **D**: maximum
- **I**: disabled

### A.4.2 Obtaining feedback

To obtain feedback, you need to direct the first-order diffracted beam from the grating back into the laser diode. Start by carefully gluing the grating to the grating holder. The grating should be flush with the lip on the bottom of the holder (see Fig. A.3); this lip helps ensure that the grating is straight. The grooves should be vertical. Most gratings have an arrow on the side to indicate the blaze direction; the grating grooves are vertical when the arrow is horizontal<sup>9</sup>. To figure out where the grating should be glued, first attach it to the grating holder with double-stick tape, adjust it to the angle that gives feedback, and make sure that the output beam of the laser diode is centered on the grating at this angle. This is important since the beam position will change as you rotate the grating to tune the laser, and you don't want

---

<sup>9</sup>If you are using a holographic grating, it doesn't matter which direction the arrow points as long as it is horizontal.



the beam to be clipped. Once the correct position is found, glue the grating on with five-minute epoxy (a couple of drops on each side is sufficient and makes it easier to remove if you make a mistake). Leaving the grating attached with double-stick tape is not recommended for long-term stability, since the tape becomes less sticky over time.

After the epoxy is dry, assemble the remaining pieces of the grating mount. Drop the PZT in the hole with its hemispherical end (if it has one) facing the grating and its leads coming out through the slot in the side<sup>10</sup>. Screw in the precision adjustment screw with its ball against the flat end of the PZT. Adjust the screw to give yourself some range to change the grating angle in both directions. Don't bend the front of the grating mount out too far, as the thin part at the hinge may crack.

Adjust the feedback with the temperature set to the desired operating temperature. Your previous measurements of wavelength vs. temperature will allow you to make a good estimate of the best temperature to operate the laser. To obtain feedback, you need to direct the first-order diffracted beam back into the laser diode. It is possible to see the diffracted beam directly by turning the current well above threshold and rotating the grating mount while holding a small sliver of card by the side of the collimation tube, making sure you are not blocking the output beam from the diode. As you rotate the grating mount, the diffracted beam should move. At this point, it is useful to turn the vertical adjustment screw until the output and diffracted beams are at the same height. Now set the current close to the lasing threshold and look at the output beam on a card; as you rotate the grating mount, you should see

---

<sup>10</sup>The longer of the two PZT wires is the positive voltage lead. This is important since the PZT voltage range is asymmetric: -30 V to +150 V.

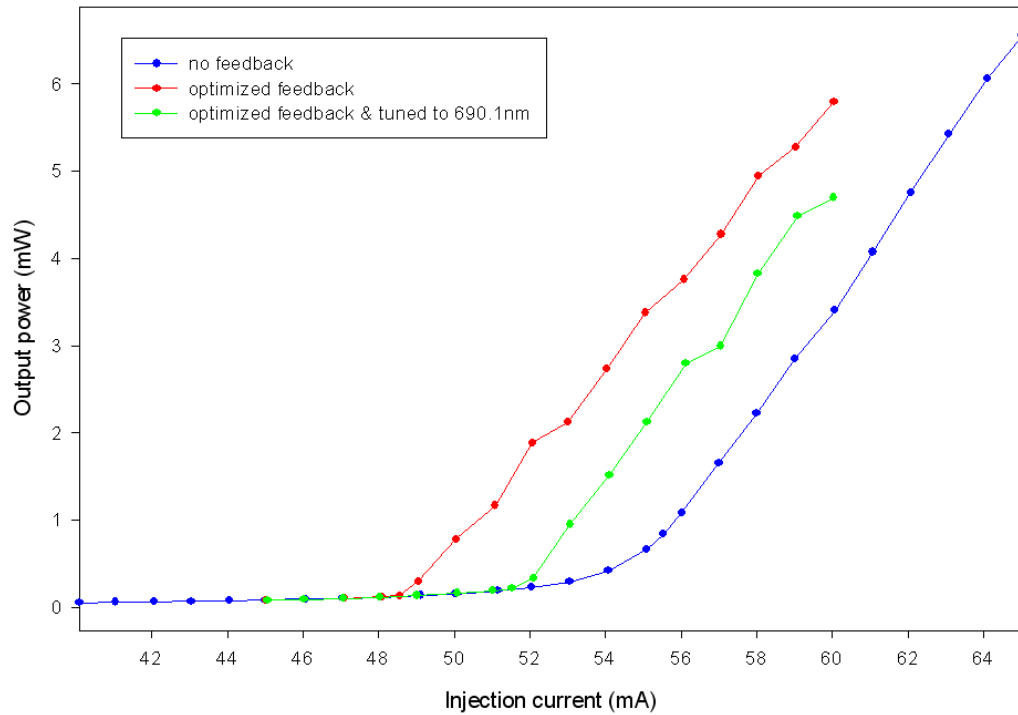


Figure A.8: Laser output power as a function of current. Note the sharp increase in power at threshold with the onset of lasing. The tuned laser has a slightly higher threshold current since rotating the grating from the optimal angle reduces the feedback.

it become noticeably brighter at some angle. This occurs when feedback from the grating pushes the diode over the lasing threshold. If you do not see this, the vertical adjustment is probably wrong. Check it again by comparing the heights of the output and diffracted beams, as described above. Alternatively, you can sometimes see a second beam near the main output beam that also moves when you turn the grating. Turning the grating to merge these two beams will give feedback. For visible lasers, looking at the beam on a white card works well. For IR lasers, it is much easier to use a white card and look at the beam through an IR viewer or camera than to use

an IR card for this step<sup>11</sup>. Before screwing down the grating mount at the angle that gives feedback, measure the threshold current of the free-running diode. Comparing this value with the threshold current after feedback has been optimized gives a good indication of how well the feedback is aligned.

If you keep turning down the current, the range of grating angles for which there is observable feedback decreases. Turn the current down far enough that feedback occurs only over a small angular range and screw down the grating mount at an angle within this range. You can make small corrections with the precision adjustment screw. This angle does not have to be extremely precise since you will change it later when tuning the laser. Once the angle is correct, it is time to fine-tune the vertical adjustment. Put a power meter in front of the laser and watch it while carefully adjusting the vertical screw. Optimize the power, then turn down the current and optimize it again. Repeat this step until you can no longer make significant changes in the output power. Once you've done as well as you can, measure the threshold current again and make sure it has decreased by about 10%. If the decrease is significantly less than this, either the grating angle or (more likely) the vertical adjustment is wrong. Try looking over a larger range of vertical adjustments to see if you can find a better optimum point. Fig. A.8 shows typical threshold behavior before and after feedback adjustment.

If you are going to use a metal side plate with an AR-coated window for the laser beam to exit, you can now figure out where the window should be located and glue it into the plate. The alternative is to make the side of the laser enclosure where

---

<sup>11</sup>The brightness of the spot on an IR card depends not only on the brightness of the beam illuminating it but also on how long the beam has been hitting that particular spot on the card, which makes IR cards essentially useless for something like this.

the beam exits out of clear Plexiglas. We use metal side plates with windows on our lasers, although the Greiner lab has had success using Plexiglas side plates.

Once the feedback is optimized, it is time to tune the laser to the desired wavelength. Measure the wavelength while slowly turning the adjustment screw in the grating mount. The wavelength will tune continuously over some regions and occasionally jump when the laser switches from one mode to another. Leave the laser in the mode closest to your desired wavelength. Depending on how close you are, you may need to adjust the temperature (higher temperature corresponds to longer wavelength). At this point, you need to look at the output on a Fabry-Pérot cavity to see whether the laser is operating in a single mode. Single mode operation is indicated by a single peak in the Fabry-Pérot cavity spectrum. Several peaks or the absence of any peaks indicates that the laser is multi-mode. If the laser is not single mode, tweak the current slightly. Changing the current is basically a fast way to change the temperature of the emission region, so increasing the current makes the wavelength longer just like increasing the temperature does. Once you are close to the desired wavelength, try tuning over it using the PZT. Watch the spectrum to make sure the laser remains single-mode. If you reach the end of the tuning range, you can push it further in the same direction by slightly changing the current in such a way that it pushes the wavelength in the same direction as the PZT adjustment (i.e. if you were tuning to longer wavelengths with the PZT, increase the current slightly). The theoretical basis for this simultaneous tuning with current and PZT is given in [63]. If you can't reach the desired wavelength, change the temperature in the appropriate direction and try again. Keep adjusting the parameters in this way until the laser

remains single-mode while tuning over some region around your desired wavelength with the PZT. If you changed the grating angle significantly to tune the laser, it is a good idea to re-optimize the vertical adjustment at the new grating angle. It is normal for the threshold to increase after tuning, since you have reduced the feedback by changing the grating angle (see Fig. A.8).

## A.5 Some notes on laser operation

To maximize their lifetime, it is best to turn the lasers off when not in use. Always leave the temperature control enabled to avoid small alignment changes due to thermal cycling.

For high power lasers, dirt sometimes collects on the output window at the location where the beam exits. If the power output of the laser suddenly drops, check the window and clean it with methanol if it is dirty.

## A.6 Limitations and possible improvements

All the parts for our lasers are made out of aluminum 6061. It is probably better to make them out of brass, which is heavier and thus better at damping out vibrations.

The design described here provides no ability to adjust the  $x$  and  $y$  position of the collimation lens relative to the laser diode. This makes it difficult to correct undesired effects such as vertical deflection of the beam by the lens. See [51] for a similar design that does provide  $x$  and  $y$  adjustment of the collimation lens.

Using the Omron G5V-1-2 relay to short-circuit the laser diode when the current

is disabled is probably a good idea. We have not used these relays because Thorlabs controllers lack an appropriate output to open the relay. It is possible that the hole pattern on the circuit board is not correct for this relay.

# Bibliography

- [1] Streater, R. & Wightman, A. *PCT, Spin and Statistics, and All That* (W. A. Benjamin, New York, 1964).
- [2] Branco, G. C., Lavoura, L. & Silva, J. P. *CP Violation*. International Series of Monographs on Physics (Oxford University Press, Oxford, 1999).
- [3] Pospelov, M. & Ritz, A. Probing CP violation with electric dipole moments. In Roberts, B. L. & Marciano, W. J. (eds.) *Lepton Dipole Moments*, vol. 20 of *Advanced Series on Directions in High Energy Physics*, chap. 13, 439–518 (World Scientific, Singapore, 2010).
- [4] Jarlskog, C. Commutator of the quark mass matrices in the standard electroweak model and a measure of maximal CP nonconservation. *Phys. Rev. Lett.* **55**, 1039–1042 (1985).
- [5] Commins, E. D. & DeMille, D. The electric dipole moment of the electron. In Roberts, B. L. & Marciano, W. J. (eds.) *Lepton Dipole Moments*, vol. 20 of *Advanced Series on Directions in High Energy Physics*, chap. 14, 519–581 (World Scientific, Singapore, 2010).
- [6] Nakamura, K. *et al.* Cabibbo-Kobayashi-Maskawa quark-mixing matrix. *J. Phys. G* **37**, 075021 (2010).
- [7] Pospelov, M. E. & Khriplovich, I. B. Electric dipole moment of the W boson and the electron in the Kobayashi-Maskawa model. *Sov. J. Nucl. Phys.* **53**, 638–640 (1991).
- [8] Glashow, S. L., Iliopoulos, J. & Maiani, L. Weak interactions with lepton-hadron symmetry. *Phys. Rev. D* **2**, 1285 (1970).
- [9] Hudson, J. J., Kara, D. M., Smallman, I. J., Sauer, B. E., Tarbutt, M. R. & Hinds, E. A. Improved measurement of the shape of the electron. *Nature* **473**, 493 (2011).
- [10] Nakamura, K. *et al.* Neutrino mass, mixing, and oscillations. *J. Phys. G* **37**, 075021 (2010).

- [11] Archambault, J. P., Czarnecki, A. & Pospelov, M. Electric dipole moments of leptons in the presence of Majorana neutrinos. *Phys. Rev. D* **70**, 073006 (2004).
- [12] Sakharov, A. D. Violation of CP invariance, C asymmetry, and baryon asymmetry of the universe. *Pisma Zh. Eksp. Teor. Fiz.* **5**, 32 (1967).
- [13] Nakamura, K. *et al.* Higgs bosons: Theory and searches. *J. Phys. G* **37**, 075021 (2010).
- [14] Nir, Y. CP violation in and beyond the Standard Model (1999). [arXiv:hep-ph/9911321v2](#).
- [15] Schiff, L. I. Measurability of nuclear electric dipole moments. *Phys. Rev.* **132**, 2194–2200 (1963).
- [16] Sandars, P. G. H. The electric dipole moment of an atom. *Phys. Lett.* **14**, 194–196 (1965).
- [17] Sandars, P. G. H. Enhancement factor for the electric dipole moment of the valence electron in an alkali atom. *Phys. Lett.* **22**, 290–291 (1966).
- [18] Salpeter, E. E. Some atomic effects of an electronic electric dipole moment. *Phys. Rev.* **112**, 1642–1648 (1958).
- [19] Commins, E. D., Jackson, J. D. & DeMille, D. P. The electric dipole moment of the electron: An intuitive explanation for the evasion of Schiff’s theorem. *Am. J. Phys.* **75**, 532 (2007).
- [20] Hinds, E. A. Testing time reversal symmetry using molecules. *Phys. Scripta* **T70**, 34 (1997).
- [21] Meyer, E. R., Bohn, J. L. & Deskevich, M. P. Candidate molecular ions for an electron electric dipole moment experiment. *Phys. Rev. A* **73**, 062108 (2006).
- [22] Khriplovich, I. B. & Lamoreaux, S. K. *CP Violation without Strangeness: Electric Dipole Moments of Particles, Atoms, and Molecules* (Springer, 1997).
- [23] Regan, B. C., Commins, E. D., Schmidt, C. J. & DeMille, D. New limit on the electron electric dipole moment. *Phys. Rev. Lett.* **88**, 071805 (2002).
- [24] Bethlem, H., Berden, G. & Meijer, G. Decelerating neutral polar molecules. *Phys. Rev. Lett.* **83**, 1558–1561 (1999).
- [25] Rangwala, S., Junglen, T., Rieger, T., Pinkse, P. & Rempe, G. Continuous source of translationally cold dipolar molecules. *Phys. Rev. A* **67**, 1–4 (2003).



- 
- [26] Krems, R. V., Stwalley, W. C. & Friedrich, B. (eds.) *Cold Molecules: Theory, Experiment, Applications* (CRC Press, 2009).
- [27] Leanhardt, A., Bohn, J., Loh, H., Maletinsky, P., Meyer, E., Sinclair, L., Stutz, R. & Cornell, E. On measuring the electron electric dipole moment in trapped molecular ions (2010). [arXiv:1008.2997v3\[physics.atom-ph\]](#).
- [28] Bransden, B. H. & Joachain, C. J. *Physics of Atoms and Molecules* (Longman, Harlow, Essex, 1983).
- [29] Brown, J. M. & Carrington, A. *Rotational Spectroscopy of Diatomic Molecules* (Cambridge University Press, 2003).
- [30] Paulovič, J., Nakajima, T., Hirao, K., Lindh, R. & Malmquist, P. Å. Relativistic and correlated calculations on the ground and excited states of ThO. *J. Chem. Phys.* **119**, 798–805 (2003).
- [31] Sobelman, I. I. *Atomic Spectra and Radiative Transitions* (Springer, 1992).
- [32] Edvinsson, G. & Lagerqvist, A. A low-lying  $\Omega = 2$  state in the ThO molecule. *J. Mol. Spectrosc.* **113**, 93–104 (1985).
- [33] Edvinsson, G. & Lagerqvist, A. Rotational analysis of yellow and near infrared bands in ThO. *Phys. Scripta* **30**, 309–320 (1984).
- [34] Edvinsson, G. & Lagerqvist, A. Rotational analysis of some violet and green bands in the ThO spectrum. *J. Mol. Spectrosc.* **122**, 428–439 (1987).
- [35] Hamilton, P. *Preliminary results in the search for the electron electric dipole moment in PbO\**. Ph.D. thesis, Yale University (2010).
- [36] Vutha, A. C., Spaun, B., Gurevich, Y. V., Kirilov, E., Hutzler, N. R., Doyle, J. M., Gabrielse, G. & DeMille, D. Magnetic and electric dipole moments of the  $H^3\Delta_1$  state in ThO (2011). [arXiv:1107.2287v1\[physics.atom-ph\]](#).
- [37] Sakurai, J. J. *Modern Quantum Mechanics* (Addison-Wesley, Reading, MA, 1994).
- [38] Bickman, S., Hamilton, P., Jiang, Y. & DeMille, D. Preparation and detection of states with simultaneous spin alignment and selectable molecular orientation in PbO. *Phys. Rev. A* **80**, 023418 (2009).
- [39] Kozlov, M. G. & DeMille, D. Enhancement of the electric dipole moment of the electron in PbO. *Phys. Rev. Lett.* **89**, 133001 (2002).

- [40] DeMille, D., Bay, F., Bickman, S., Kawall, D., Hunter, L. R., Krause, D., Jr, Maxwell, S. & Ulmer, K. Search for the electric dipole moment of the electron using metastable PbO. In Budker, D., Bucksbaum, P. H. & Freedman, S. J. (eds.) *Art and Symmetry in Experimental Physics*, no. 596 in AIP Conf. Proc., 72 (AIP, New York, 2001).
- [41] Vutha, A. C., Campbell, W. C., Gurevich, Y. V., Hutzler, N. R., Parsons, M., Patterson, D., Petrik, E., Spaun, B., Doyle, J. M., Gabrielse, G. & DeMille, D. Search for the electric dipole moment of the electron with thorium monoxide. *J. Phys. B* **43**, 074007 (2010). [arXiv:0908.2412v2\[physics.atom-ph\]](#).
- [42] Goncharov, V., Han, J., Kaledin, L. & Heaven, M. C. Ionization energy measurements and electronic spectra for ThO. *J. Chem. Phys.* **122**, 204311 (2005).
- [43] Meyer, E. R. & Bohn, J. L. Prospects for an electron electric-dipole moment search in metastable ThO and ThF<sup>+</sup>. *Phys. Rev. A* **78**, 010502 (2008).
- [44] Edvinsson, G., Selin, L.-E. & Åslund, N. On the band spectrum of ThO. *Arkiv för Physik* **30**, 283–319 (1965).
- [45] Marian, C. M., Wahlgren, U., Gropen, O. & Pyykkö, P. Bonding and electronic structure in diatomic ThO: Quasirelativistic effective core potential calculations. *J. Mol. Struct.-Theochem* **169**, 339–354 (1988).
- [46] Crawford, F. H. Zeeman effect in diatomic molecular spectra. *Rev. Mod. Phys.* **6**, 90 (1930).
- [47] DeMille, D., Doyle, J. M. & Gabrielse, G. NSF Grant Proposal (2009).
- [48] Hutzler, N. R., Parsons, M., Gurevich, Y. V., Hess, P. W., Petrik, E., Spaun, B., Vutha, A. C., DeMille, D., Gabrielse, G. & Doyle, J. M. A cryogenic beam of refractory, chemically reactive molecules with expansion cooling. *Physical Chemistry Chemical Physics* (2011). [arXiv:1101.4217v1\[physics.atom-ph\]](#).
- [49] Darnell, A. J., McCollum, W. A. & Milne, T. A. Vapor pressure of thorium. *J. Phys. Chem.* **64**, 341–346 (1960).
- [50] Gillen, J. Private communication (2008).
- [51] Ricci, L., Weidemüller, M., Esslinger, T., Hemmerich, A., Zimmermann, C., Vuletic, V., König, W. & Hänsch, T. W. A compact grating-stabilized diode laser system for atomic physics. *Opt. Commun.* **117**, 541–549 (1995).
- [52] Budker, D., Rochester, S. M. & Yashchuk, V. V. Obtaining frequency markers of variable separation with a spherical mirror Fabry-Perot interferometer. *Rev. Sci. Instrum.* **71**, 2984–2987 (2000).

- [53] Barry, J. Private communication (2010).
- [54] Zhao, W. Z., Simsarian, J. E., Orozco, L. A. & Sprouse, G. D. A computer-based digital feedback control of frequency drift of multiple lasers. *Rev. Sci. Instrum.* **69**, 3737 (1998).
- [55] Burke, J. H. T., Garcia, O., Hughes, K. J., Livedalen, B. & Sackett, C. A. Compact implementation of a scanning transfer cavity lock. *Rev. Sci. Instrum.* **76**, 116105 (2005).
- [56] Matsubara, K., Uetake, S., Ito, H., Li, Y., Hayasaka, K. & Hosokawa, M. Precise frequency-drift measurement of extended-cavity diode laser stabilized with scanning transfer cavity. *Jpn. J. Appl. Phys.* **44**, 229–230 (2005).
- [57] Farkas, D. *An Optical Reference and Frequency Comb for Improved Spectroscopy of Helium*. Ph.D. thesis, Harvard University (2006).
- [58] Drever, R. W. P., Hall, J. L., Kowalski, F. V., Hough, J., Ford, G. M., Munley, A. J. & Ward, H. Laser phase and frequency stabilization using an optical resonator. *Appl. Phys. B* **31**, 97–105 (1983).
- [59] Black, E. D. An introduction to Pound-Drever-Hall laser frequency stabilization. *Am. J. Phys.* **69**, 79–87 (2001).
- [60] Kawall, D., Bay, F., Bickman, S., Jiang, Y. & DeMille, D. Precision Zeeman-Stark spectroscopy of the metastable  $a(1)[^3\Sigma^+]$  state of PbO. *Phys. Rev. Lett.* **92**, 133007 (2004).
- [61] Berkeland, D. J. & Boshier, M. G. Destabilization of dark states and optical spectroscopy in Zeeman-degenerate atomic systems. *Phys. Rev. A* **65**, 033413 (2002).
- [62] Wieman, C. E. & Hollberg, L. Using diode lasers for atomic physics. *Rev. Sci. Instrum.* **62**, 1–20 (1991).
- [63] Petridis, C., Lindsay, I. D., Stothard, D. J. M. & Ebrahimzadeh, M. Mode-hop-free tuning over 80 GHz of an extended cavity diode laser without antireflection coating. *Rev. Sci. Instrum.* **72**, 3811 (2001).